Motion Control and Temperature Monitoring of a Six-Phase Permanent Magnet Synchronous Machine (PMSM)

by

Marcos Orviz Zapico

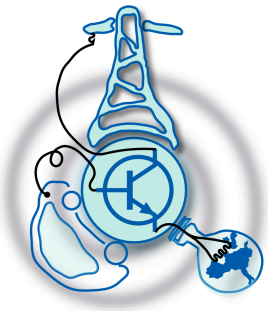

Submitted to the Department of Electrical Engineering, Electronics, Computers and Systems
in partial fulfillment of the requirements for the degree of
Electrical Energy Conversion and Power Systems
at the
UNIVERSIDAD DE OVIEDO
July 2020

Author .....

Certified by .....
David Díaz Reigosa
Associate Professor
Thesis Supervisor

Certified by .....
Daniel Fernández Alonso
Assistant Professor
Thesis Supervisor

Motion Control and Temperature Monitoring of a Six-Phase Permanent Magnet Synchronous Machine (PMSM)

by

Marcos Orviz Zapico

Submitted to the Department of Electrical Engineering, Electronics, Computers and Systems
on July 30, 2020, in partial fulfillment of the
requirements for the degree of
Electrical Energy Conversion and Power Systems

Abstract

Nowadays, electric machines are responsible for more than 50% of the global electricity consumption, as they are notable for their high power density and efficiency, good dynamic performance and controllability. This makes electric machines a suitable option for key sectors as the automotive or wind generation ones. The use of permanent magnet synchronous machines (PMSMs) has been sustainedly increasing during the last decades due to their superior performance compared with other types of electric machines in terms of power density, speed range or dynamic response. Most of PMSMs today are three-phase. Nevertheless the design of multi-phase PMSMs can provide several advantages. Above all, their fault-tolerant capability makes multi-phase machines a very attractive option for applications in which high reliability is required, like aviation, aerospace or marine applications. Open-phase faults due to a failure in a power electronic device are the most common ones. Fault-tolerant operation can be achieved by applying a modified fault-tolerant control (FTC) strategy after the fault occurs. Several FTC methods present in literature are described in this document. The different strategies are more or less convenient depending on the multi-phase machine configuration: non-three-phase series machines, non-multi three-phase machines or multi three-phase machines. In the present Master Thesis a novel fault-tolerant control strategy is proposed. This strategy is based on distinguishing two three-phase sets in a six-phase IPMSM so that when a fault occurs in one of the three-phase sets, the healthy one can compensate it.

Among all PMSM parts, permanent magnets (PMs) are the weakest, as their properties strongly depend on the temperature. Usually, the maximum operating temperature of the machine is determined by the PM maximum operating temperature. Due to this, PM temperature estimation/measurement during normal operation of the machine is a very interesting feature. However, temperature measurement provides many inconveniences being thus temperature estimation preferred. PM temperature estimation methods can be divided into thermal models, BEMF based methods and

methods which inject some form of test signal into the stator terminals of the machine. Thermal models require previous knowledge of the machine geometry, materials and cooling system. Hence, the model is only valid for a specific machine design. BEMF based methods cannot work at standstill or very low speeds and also require previous knowledge of some machine parameters. Methods based on the injection of a test signal can be further divided into pulse injection based methods and high-frequency (HF) signal injection based methods. Both types of methods can be used in the whole speed range of operation of the machine and do not require previous knowledge of machine parameters in principle.

Matlab and Simulink are used for simulating some of the described fault-tolerant control techniques. A PM-temperature estimation method based on high-frequency signal injection is also simulated.

An experimental test-bench with a dual three-phase interior permanent magnet synchronous machine (DT-IPMSM) and an IPMSM in charge of fixing the speed is built. The followed steps for reaching a suitable performance are explained. The proposed FTC technique and the simulated PM temperature estimation method based on high-frequency signal injection are tested in the experimental test-bench.

Thesis Supervisor: David Díaz Reigosa
Title: Associate Professor

Thesis Supervisor: Daniel Fernández Alonso
Title: Assistant Professor

Acknowledgments

I would like to start by thanking my advisors David Díaz Reigosa and Daniel Fernández Alonso for their time and help whenever I needed it during the development of this Master Thesis. Without doubt, the interest I show today in research and the world of electricity and electronics is thanks to them. I can not forget my colleagues in the lab María, Diego and Cristina for the countless tips they have given me since I met them. I would like to mention all my classmates during the master, with whom I have lived these two years, sharing the hardest times of the master, but also really good moments. My thanks to all the professors for the lessons learned, with especial mention to Fernando Briz.

Finally, I want to thank all my family and friends, for the patience and encouragement that they always transmit me, standing out above all my mother, Ani and my father, Gelin, without which none of this would be possible.

Contents

List of Figures

List of Tables

Chapter 1

Introduction

1.1 Background

The present Master Thesis is framed within the activities programmed by the project '*Diseño, Control y Monitorización de Máquinas Síncronas de Imanes Permanentes Polifásicas*' which is part of '*Plan Nacional de Investigación Científica, Desarrollo e Innovación Tecnológica (Plan Nacional de I+D+i), del Ministerio de Economía y Competitividad*'. AECP (Accionamientos Eléctricos y Convertidores de Potencia) research group, from the University of Oviedo, has received funding for three years in order to develop this project.

Electric machines can be used in a wide range of industrial and residential applications like fans, air-conditioning, refrigerators or elevators. It is estimated that the use of electric motors today accounts for more than 50% of global electricity consumption [1]. High torque/power density, high efficiency, good dynamic performance and controllability are some of the most interesting characteristics of electric motors. Hence, they are suitable for high performance applications such as wind power generation, automotive, servo drive, robotics, military, etc. As an example, the development of Electric Vehicles (EVs), Hybrid Electric Vehicles (HEVs), etc., in which the vehicle is powered with an electric motor, has grown exponentially over the last decade, and

the forecast is that it will stay that way until at least 2030 [2].

Among all types of electric machines, the use of permanent magnet synchronous machines (PMSMs) has extensively increased in both traction and industrial applications. These machines allow a better performance compared with other type of electrical machines such as induction machines (IMs) or DC motors, in terms of power density, torque density, dynamic response, speed range, controllability and efficiency. The main drawbacks of PMSMs are related with the high and often unpredictable price of rare-earth materials and the risk of demagnetization due to excessive operating currents/temperature.

Most of the AC machines in existence today are three-phase. However, when a machine is fed by a power converter, there is no reason why the machine must have the same number of phases that the power grid. The design of multi-phase machines (with a number of phases higher than three) may provide relevant advantages compared with a three-phase machine, especially in aspects related with the fault-tolerant capability of the machine [3–26]. The use of multi-phase drives is already accepted in aviation, aerospace and marine applications, in which it is essential to guarantee the operation of the converter-machine assembly in case of failure. However, there are other sectors like electric traction (electric vehicles, hybrid electric vehicles, railway traction,...) or wind generation, where multi-phase drives are considered as an interesting future option.

Despite the advantages of multi-phase drives, there are some aspects related with the design and control of both the machine and the power converter that are still not satisfactorily resolved and where intense research activity is being carried out.

The performance of PMSMs, whether they are multi-phase or three-phase ones, is directly dependent on the permanent magnets and their magnetization state [27–35]. Hence, it is particularly relevant to develop monitoring techniques that can be implemented in this type of machines and that can be integrated with the machine's own control strategy, in order to minimize the risk of magnet demagnetization. In this

way, the fault-tolerant capability of the drive is substantially improved. Although this type of technique has already been developed for conventional three-phase permanent magnet machines, its application has so far been restricted to laboratory prototypes, and has not been studied in multi-phase machines.

1.2 Research Motivation

The main objective of the proposed Master Thesis is the control of a multi-phase machine, adding the monitoring of the permanent magnet temperature. The specific goals of the project are:

- Development of fault-tolerant control algorithms for the multi-phase machine.
- Development of monitoring techniques for multi-phase machines:
  - Permanent magnet temperature estimation methods.
- Development of the necessary simulation models for the theoretical study of these techniques.
- Development of experimental tests to confirm the validity of these methods.

1.3 Outline of the Document

This Master Thesis is organized in seven chapters and one appendix:

- **Chapter 2** introduces the pros and cons of multi-phase machines. In addition, the dynamic model of both three-phase and six-phase PMSMs is included.
- **Chapter 3** evaluates different fault-tolerant control strategies for multi-phase PMSMs present in literature, and proposes a new one. The proposed FT control strategy is based on compensating the currents in the faulty three-phase winding with the healthy one.
- **Chapter 4** studies temperature effects in PMSMs; state of the art of PM temperature estimation methods in PMSMs is also analysed.

- **Chapter 5** shows the obtained results when simulating some of the control strategies mentioned in chapter 3 and chapter 4.
- **Chapter 6** evaluates the proposed FT control strategy in a real test-bench. Experimental results are analysed. In the same way, one of the described PM temperature estimation methods is assessed in the test-bench.
- **Chapter 7** summarizes the contributions of this Master Thesis and outlines future research lines.
- **Appendix A** develops the different steps that were followed to obtain a suitable performance of the experimental test-bench as well as the elements that build it.

Chapter 2

Multi-phase PMSMs

2.1 Introduction

As stated in Chapter 1, the use of standard electrical machines has been continuously growing. For some specific applications, the conventional three-phase variable speed drives are being substituted by multi-phase drives [7]. Multi-phase machines were first proposed in the late 1960s, when inverter-fed AC drives were in the initial development stage, as it was considered the best solution to remove the low frequency torque ripple produced by the six-step mode of three-phase inverter operation. However, research on this type of machines was boosted in the 1990s, especially due to developments in electric ship propulsion [36].

Nowadays, reliability of drives is a crucial aspect, and it can be improved in different ways. Oversizing might be a solution, making the system work below the maximum functioning point during normal operation. In this way, lifetime is increased. However, this could lead to lower efficiencies and higher costs. Besides, in case of failure, the system will not be able to continue working [8].

Multi-phase drives provide additional degrees of freedom compared with the conventional three-phase ones. These degrees of freedom can be used for different purposes [36]. One of the main characteristics that multi-phase machines provide is their

high fault-tolerant capability without need of extra hardware. Moreover, under open-phase faults, multiphase machines allow to carry out a fault-tolerant operation by using a modified control strategy in the remaining healthy phases [13]. Other interesting features of multi-phase machines are related with a high level of power [7], and reduced power flow per phase [3]. Nowadays, new electromechanical systems with an increased torque density are demanded by industry. In addition, the number of high-speed and low-cost applications is continuously growing. These facts have led to an increased research on multiphase PM machines [3]. The most popular applications for multi-phase machines include: electric ship propulsion, EVs and HEVs, locomotive traction, and wind generation [3, 4].

Table 2.1: Overview of Main Advantages of Multi-phase-Machine-Based-Drives [36]

Property	Three-Phase Machine	Multi-phase (n-phase) machine
Torque ripple frequency (f = fundamental frequency)	$6f$	$2nf(>6f)$
Order of the lowest spatial mmf harmonics (sinusoidal mmf machines)	5 and 7	$2n \pm 1$ $(>5, 7)$
Power/torque per phase (rated power/torque = P/Te)	$P/3$ $(Te/3)$	P/n (Te/n)
Continued operation after an open-phase fault	No[1]	Yes[2]
Torque enhancement by stator current harmonic injection	Not possible	Yes (concentrated winding machines)

[1]Not possible without modification of the power converter topology.
[2]Requires a fault-tolerant control strategy to be applied during the fault.

A disadvantage when using multiphase machines is related with the increase in the number of inverters (and thus power electronic devices) and wires. The increased number of power electronics raises cost, size and processing capacity of microcontrollers. Increasing the number of wires leads to an increase in cost, weight, and connection trouble [37].

Two types of multi-phase machine systems can be distinguished [37]. One is non-three-phase series type, in which the number of phases is not a multiple of three.

Five-phase [11], seven-phase [38] or eleven-phase [12] machines are examples of this type of machines. The other system is the three-phase series type [39–42], in which the number of phases is a multiple of three. This system can be classified in detail to non-multi three-phase [39, 40] such as six-phase and nine-phase, and multi three-phase [41, 42] such as dual three-phase and triple three-phase. Three-phase series types provide advantages especially in ease of industrial application since the three-phase theory can be applied to the drive method, being possible the use of classical three-phase converters [37].

This chapter introduces the dynamic model of a multi-phase synchronous machine starting from the one of a three-phase one. First, the synchronous reference frame in which a three-phase permanent magnet synchronous machine (PMSM) is generally specified is introduced. From it, the dynamic model of the machine is obtained, and the torque equation is developed. Once the three-phase machine is analysed, the model of a six-phase machine will be developed, studying it as a set of two three-phase systems.

2.2 Fundamental Dynamic Model of a PMSM

2.2.1 Three-phase PMSM

The dynamic model of a permanent magnet synchronous machine is usually specified in a rotor reference frame. As these machines rotate at the synchronous speed the rotor reference frame matches with the synchronous reference frame. Fig. 2-1 shows both the stationary and the synchronous (with the rotor) reference frames, in a cross-section of a three-phase, two pole PMSM. The dq^r-axis is the one related with the rotor synchronous reference frame, being the d^r-axis aligned with the PM flux, λ_{PM}, while the dq^s-axis regard to the stationary reference frame. When the model of a PM machine is referred to a synchronous reference frame, in solidarity with the

rotor, the dynamic equations of the model may be expressed as (2.1) [43].

$$\begin{bmatrix} v_{ds}^r \\ v_{qs}^r \end{bmatrix} = \begin{bmatrix} R_{ds} & 0 \\ 0 & R_{qs} \end{bmatrix} \begin{bmatrix} i_{ds}^r \\ i_{qs}^r \end{bmatrix} + p \begin{bmatrix} L_{ds} & 0 \\ 0 & L_{qs} \end{bmatrix} \begin{bmatrix} i_{ds}^r \\ i_{qs}^r \end{bmatrix} + \begin{bmatrix} 0 & -\omega_r L_{qs} \\ \omega_r L_{ds} & 0 \end{bmatrix} \begin{bmatrix} i_{ds}^r \\ i_{qs}^r \end{bmatrix} + \begin{bmatrix} 0 \\ \omega_r \lambda_{PM} \end{bmatrix} \tag{2.1}$$

where,

R_{ds}	:	total resistance referred to the stator in the $d-$axis.
R_{qs}	:	total resistance referred to the stator in the $q-$axis.
L_{ds}	:	total inductance referred to the stator in the $d-$axis.
L_{qs}	:	total inductance referred to the stator in the $q-$axis.
ω_r	:	rotational speed of the rotor in rad/s.
λ_{PM}	:	flux induced by the permanent magnets.
p	:	differential operator. Equivalent to Laplace s variable.

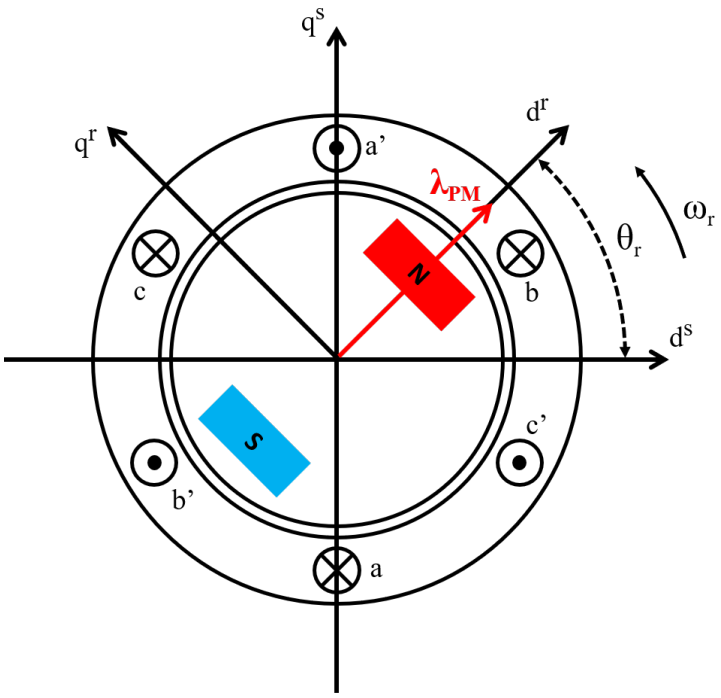

Figure 2-1: Synchronous and stationary reference frames for a three-phase PM machine

The torque produced by a PMSM is expressed as equation (2.2) shows. This equation can be split in two components. On one side, the reluctance torque, T_{rel}

(2.3), which depends on the saliency of the machine, i.e. the difference between the $d-$ and $q-$axis inductances. On the other side, the electromagnetic torque, T_e (2.4), which is proportional to the PM flux, λ_{PM} and the $q-$axis current, i^r_{qs}. P stands for the machine number of poles.

$$T = \frac{3}{2}\frac{P}{2}(\lambda_{PM} i^r_{qs} + (L_{ds} - L_{qs}) i^r_{ds} i^r_{qs}) \tag{2.2}$$

$$T_{rel} = \frac{3}{2}\frac{P}{2}((L_{ds} - L_{qs}) i^r_{ds} i^r_{qs}) \tag{2.3}$$

$$T_e = \frac{3}{2}\frac{P}{2}(\lambda_{PM} i^r_{qs}) \tag{2.4}$$

Depending on how torque is produced, PMSMs may be classified in two types: interior permanent magnet synchronous machines (IPMSMs) and surface permanent magnet synchronous machines (SPMSMs). Insert permanent magnet synchronous machines (Ins-PMSMs) can be classified as a type of SPMSM in which the permanent magnets are inserted in the surface of the rotor core. Both IPMSMs and SPMSMs, as well as Ins-PMSMs produce electromagnetic and reluctance torque. However, in an IPMSM, the permanent magnets are embedded in the rotor core in a way that the machine's saliency will be higher compared with a SPMSM. This last machine has a symmetric rotor structure so that the $d-$ and the $q-$axis inductances are very similar. Hence, for a SPMSM the reluctance torque is almost negligible. Summarizing, IPMSM produce both electromagnetic torque and reluctance torque. For SPMSMs, the electromagnetic torque generation is lower than in IPMSMs. Both SPMSMs and Insert PMSMs have a very low or null reluctance torque production.

Table 2.2: Comparison of PMSMs

	IPMSM	SPMSM	Insert
Magnetic flux linkage	$\lambda_{PM} > 0$	$\lambda_{PM} > 0$	$\lambda_{PM} > 0$
d and q inductances	$L_d < L_q$	$L_d \approx L_q$	$L_d \approx L_q$

2.2.2 Multi-phase PMSM

In section 2.2.1, the dynamic model of a three-phase PM synchronous machine is analysed. For a multi-phase PMSM the procedure is quite similar, but in this case the increased number of phases must be considered. In this Master Thesis, a six-phase interior permanent magnet synchronous machine (IPMSM) will be studied (see appendix A.3). This multi-phase machine may be also understood as a *'dual three-phase PM machine'* (DT-PMSM) since its six phases can be analysed as two sets of three-phase stator windings that are spatially shifted by a certain electric angle, with isolated neutral points for both sets [21]. Both possibilities (isolated or connected neutral points between three-phase windings) have their own advantages. Having the neutral points isolated allows to avoid the flow of zero-sequence currents, thus reducing the number of required current controllers. Moreover, this arrangement provides isolation between windings, improving the DC-bus voltage utilization. On the other side, a single isolated neutral point connection gives an extra degree of freedom (from four to five), providing better means for fault-tolerant operation. It must be considered that an additional current controller is required [15]. In principle, to have both neutral points isolated, simplifies the study. Hence, this technique will be the one followed in this Master Thesis. Among the different winding configurations, the most popular one consists of having a 30º phase shift between both three-phase windings. Machines with this special winding structure, also known as asymmetrical dual three-phase machines can remove the sixth harmonic torque pulsations that always appear in conventional three-phase motors [23].

In multi-phase PM machines, as well as in a conventional three-phase ones, the rotor reference frame goes along with the synchronous reference frame. However, as

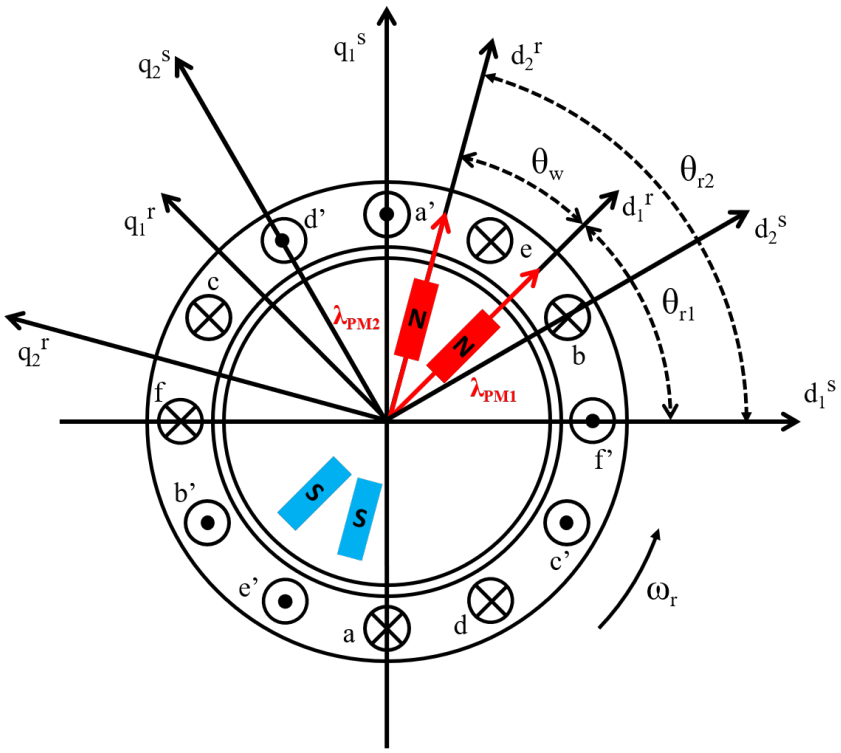

Figure 2-2: Synchronous and stationary reference frames for a six-phase PM machine

the machine is studied as a set of two three-phase systems, two synchronous reference frames will be distinguished as shown in Fig. 2-2. The dq_1^r-axis regard the rotor synchronous reference frame corresponding to the first three-phase winding, which is created by the phases abc. In the same way, dq_2^r-axis is related with the second three-phase winding, for which phases def are responsible. This can be extended for the stationary reference frame dq^s-axes. For the modelling of the multiphase PMSM, two different sets of PMs are distinguished, and thus two different PM fluxes, λ_{PM_1} and λ_{PM_2} as Fig. 2-2 shows. In principle, both fluxes will be equal when the machine operates in normal conditions. However, in fault operation, these variables will not continue being equal anymore.

Now, the dynamic model of the six-phase PMSM can be obtained using (2.1) for

both dq^r systems, as (2.5) and (2.6) shows:

$$\begin{bmatrix} v^r_{d1s} \\ v^r_{q1s} \end{bmatrix} = \begin{bmatrix} R_{d1s} & 0 \\ 0 & R_{q1s} \end{bmatrix} \begin{bmatrix} i^r_{d1s} \\ i^r_{q1s} \end{bmatrix} + p \begin{bmatrix} L_{d1s} & 0 \\ 0 & L_{q1s} \end{bmatrix} \begin{bmatrix} i^r_{d1s} \\ i^r_{q1s} \end{bmatrix} + \begin{bmatrix} 0 & -\omega_r L_{q1s} \\ \omega_r L_{d1s} & 0 \end{bmatrix} \begin{bmatrix} i^r_{d1s} \\ i^r_{q1s} \end{bmatrix} + \begin{bmatrix} 0 \\ \omega_r \lambda_{PM_1} \end{bmatrix} \tag{2.5}$$

$$\begin{bmatrix} v^r_{d2s} \\ v^r_{q2s} \end{bmatrix} = \begin{bmatrix} R_{d2s} & 0 \\ 0 & R_{q2s} \end{bmatrix} \begin{bmatrix} i^r_{d2s} \\ i^r_{q2s} \end{bmatrix} + p \begin{bmatrix} L_{d2s} & 0 \\ 0 & L_{q2s} \end{bmatrix} \begin{bmatrix} i^r_{d2s} \\ i^r_{q2s} \end{bmatrix} + \begin{bmatrix} 0 & -\omega_r L_{q2s} \\ \omega_r L_{d2s} & 0 \end{bmatrix} \begin{bmatrix} i^r_{d2s} \\ i^r_{q2s} \end{bmatrix} + \begin{bmatrix} 0 \\ \omega_r \lambda_{PM_2} \end{bmatrix} \tag{2.6}$$

The output torque produced by the multi-phase machine may be studied separately for each three-phase set, so that following equation (2.2), the total torque produced by the machine can be obtained as the addition of the torque produced by each set of three-phase windings.

$$\begin{aligned} T = T_1 + T_2 =& \frac{3}{2}\frac{P}{2}(\lambda_{PM_1} i^r_{q1s} + (L_{d1s} - L_{q1s}) i^r_{d1s} i^r_{q1s}) \\ &+ \frac{3}{2}\frac{P}{2}(\lambda_{PM_2} i^r_{q2s} + (L_{d2s} - L_{q2s}) i^r_{d2s} i^r_{q2s}) \end{aligned} \tag{2.7}$$

Once the equations are known, it is possible to build a dynamic model of the machine. Starting from the stator phase voltages, by applying the Park transformation

(2.8),(2.9), the machine voltages in a synchronous reference frame can be computed.

$$\begin{bmatrix} v^r_{d1s} \\ v^r_{q1s} \end{bmatrix} = \frac{2}{3} \begin{bmatrix} cos(\theta_1) & cos(\theta_1 - \frac{2\pi}{3}) & cos(\theta_1 + \frac{2\pi}{3}) \\ -sin(\theta_1) & -sin(\theta_1 - \frac{2\pi}{3}) & -sin(\theta_1 + \frac{2\pi}{3}) \end{bmatrix} \begin{bmatrix} v_A \\ v_B \\ v_C \end{bmatrix} \tag{2.8}$$

$$\begin{bmatrix} v^r_{d2s} \\ v^r_{q2s} \end{bmatrix} = \frac{2}{3} \begin{bmatrix} cos(\theta_2) & cos(\theta_2 - \frac{2\pi}{3}) & cos(\theta_2 + \frac{2\pi}{3}) \\ -sin(\theta_2) & -sin(\theta_2 - \frac{2\pi}{3}) & -sin(\theta_2 + \frac{2\pi}{3}) \end{bmatrix} \begin{bmatrix} v_D \\ v_E \\ v_F \end{bmatrix} \tag{2.9}$$

where θ_1 and θ_2 are the synchronous rotating angles for three-phase windings 1 and 2 respectively. After obtaining the stator voltages in a synchronous reference frame, applying (2.5) and (2.6), the stator currents in the synchronous reference frame are computed. Applying the inverse Park transformation (2.10),(2.11), the phase currents can be calculated:

$$\begin{bmatrix} i_A \\ i_B \\ i_C \end{bmatrix} = \frac{2}{3} \begin{bmatrix} cos(\theta_1) & -sin(\theta) \\ cos(\theta_1 - \frac{2\pi}{3}) & -sin(\theta_1 - \frac{2\pi}{3}) \\ cos(\theta_1 + \frac{2\pi}{3}) & -sin(\theta_1 + \frac{2\pi}{3}) \end{bmatrix} \begin{bmatrix} i^r_{d1s} \\ i^r_{q1s} \end{bmatrix} \tag{2.10}$$

$$\begin{bmatrix} i_D \\ i_E \\ i_F \end{bmatrix} = \frac{2}{3} \begin{bmatrix} cos(\theta_2) & -sin(\theta) \\ cos(\theta_2 - \frac{2\pi}{3}) & -sin(\theta_2 - \frac{2\pi}{3}) \\ cos(\theta_2 + \frac{2\pi}{3}) & -sin(\theta_2 + \frac{2\pi}{3}) \end{bmatrix} \begin{bmatrix} i^r_{d2s} \\ i^r_{q2s} \end{bmatrix} \tag{2.11}$$

Up to this point, the electrical model of the machine is completely defined. The next step consists of moving to the torque model of the PMSM. This can be done by using (2.7), as it links the synchronous currents i^r_{dq12s}, with the electromagnetic torque, T_e.

Finally, for moving from the torque model of the PM machine to the mechanical one, the following equations must be followed:

$$T_e - T_{LOAD} = J\frac{d}{dt}\omega_{rm} + F\omega_{rm} \tag{2.12}$$

$$\omega_{re} = \frac{P}{2}\omega_{rm} \tag{2.13}$$

$$\theta = \int \omega_{re} \tag{2.14}$$

where T_{LOAD} is the load torque, ω_{rm} is the mechanical speed of the rotor, ω_{re} is the electrical speed of the rotor, and θ is the position of the rotor. It must be taken into account that:

$$\theta_1 = \theta \tag{2.15}$$

$$\theta_2 = \theta + \theta_w \tag{2.16}$$

being θ_w the phase shift between both three-phase windings. Once the angle is calculated, the feedback process can be done to start again from the beginning. It must be mentioned that for a conventional three-phase machine the process would be exactly the same, but only using the equations related to a single three-phase system. This model will be useful for building a simulation model of the studied DT-IPMSM

in Simulink (see Chapter 5).

Chapter 3

Fault-Tolerant Control (FTC) Strategies

As mentioned in Chapter 2, multi-phase machines provide several advantages compared with the conventional three-phase ones. Added to a reduced power per phase, smaller torque ripple [3, 4], improved noise characteristics [14] or larger power rating [16], multi-phase machines highlight due to their fault-tolerant capability [3, 4, 7, 14–17]. This means that the machine is capable to continue the operation if a failure occurs in one or more phases [17]. Moreover, no additional hardware is required for achieving the fault-tolerant operation, as it can be accomplished by applying a modified control strategy [7]. Other ways of achieving the fault-tolerant capability are related with special machine designs [15, 18], or the development of an application-specific converter topology [15, 19]. However most of research focus on the post-fault control [15]. The fault-tolerant capability makes multi-phase machines suitable for applications in which high reliability is required [3, 4, 7, 14–17].

Several different types of faults can appear in an electric drive, both in the inverter and in the machine. In this way, faults can be classified in [4]:

- Short-circuits: In a phase, inverter switch, interturn, etc.
- Open-circuits: In an inverter switch, phase, line, etc.

Fig. 3-1 shows a scheme with a set of fault possibilities for a five-phase machine.

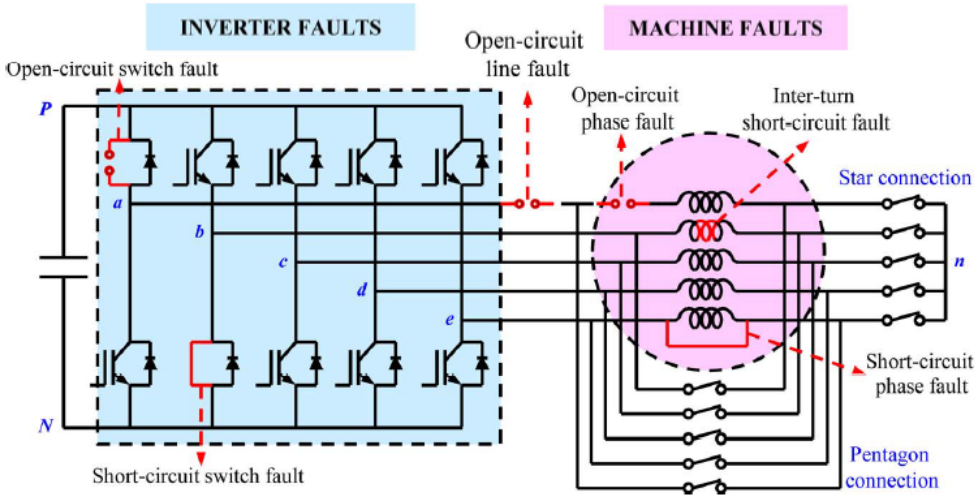

Figure 3-1: Scheme for different fault possibilities in a five-phase machine [4]

However, as stated in [20], the failure rate of power electronics supposes more than 50% of all the remaining component faults. Hence, in multi-phase machines the increase of power electronic devices means an increase in the failure rate [21]. Among all the types of faults that have been previously mentioned, the most typical one found consists of the open-circuit fault [7, 21]. When talking about multi-phase machines built with two or more sets of three-phase windings, the simplest way of keeping the operation under fault consists of isolating the faulty three-phase winding, while operating with the healthy ones. However, this would suppose a significant reduction in the achievable torque/power [4,7,15]. The goal of the fault-tolerant control strategy is to take advantage of all the healthy phases to preserve the machine's operation. However, the performance will be influenced by certain limits.

In principle, it is wanted to keep the machine producing the same torque after the fault ($T_n^{post} = T_n^{pre}$). However, it must be taken into account that, as one of the phases has been disconnected, to keep the same torque might suppose current to be above the pre-fault rms rated value ($I_{max}^{post} >> I_{max}^{pre}$). This could lead to violate the semiconductor ratings. Hence, *limit 1* will be defined as the conservative one that keeps the post-fault currents at the same rated values that in the pre-fault operation

($I_{max}^{post} = I_{max}^{pre}$). This might cause a reduction in the rated torque after the fault. Another option, consists of allowing current to go above its initial rated value, as long as the copper losses in post-fault operation are kept constant ($P_{cu}^{post} = P_{cu}^{pre}$). This possibility is riskier, but might allow to keep torque constant [4]. It will be defined as *limit 2*. Table 3.1 shows the comparison of these limits.

Table 3.1: Qualitative comparison of FT operation limits [4]

	No limit	Limit 1	Limit 2
Current	$>> I_n^{pre}$	$= I_n^{pre}$	$> I_n^{pre}$
Joule losses	$>> P_{cu}^{pre}$	$< P_{cu}^{pre}$	$= P_{cu}^{pre}$
Temperature	$>> Te^{pre}$	$= Te^{pre}$	$> Te^{pre}$
Torque	$= T_n^{pre}$	$<< T_n^{pre}$	$< T_n^{pre}$
Damage	Short term	None	-

Depending on how these limits are fulfilled, all the different fault-tolerant control (FTC) strategies can be broadly categorized in two groups [4]:

- Minimum-loss strategy: The main goal of the control strategy is to calculate the currents that allow to produce the commanded torque in such a way that the copper losses are minimized. There are no restrictions for the currents magnitude.
- Maximum torque strategy: Currents are calculated to produce a certain torque reference on average, being then the fundamental components of phase currents forced to have equal magnitudes.

In literature, different fault-tolerant control strategies for multi-phase PMSMs can be found. Table 3.2 summarizes the main characteristics of some of the most relevant ones. Section 3.1 is devoted to describe more in depth the FT control techniques compiled in the aforementioned table. Moreover, in this Master Thesis a novel fault-tolerant control strategy will be proposed (see 3.7). The performance of the method will be tested both in simulation and in a real test-bench.

Table 3.2: Comparison of FT control techniques

	FTC-IPB (section 3.1)	FTC-VA (section 3.2)	FTC-VSD (section 3.3)	FTC-WCME (section 3.4)	FTC-MMF (section 3.5)	FT-PC (section 3.6)	FTC-WCSM (section 3.7)
Neutral point connected to the DC-link midpoint	✘	✘	✘	✘	✔	✘	✘
DT-PMSM with isolated neutral points allowed	✘	✘	✔	✔	✘	✘	✔
Limited to SPMSM	✘	✔	✘	✘	✘	✘	✘
Real-time implementation	✘	✔	✘	✔	✘	✔	✔
Synchronous reference frame current control	✘	✘	✔	✔	✔	✘	✔
Complexity	Medium	High	Medium	Low	Medium	High	Medium

3.1 Fault-Tolerant Control Based On Instantaneous Power Balance Theory (FTC-IPB)

In [14] it is proposed a fault-tolerant control technique based on the instantaneous power balance theory in such a way that the continuous operation of the machine is ensured while minimizing torque ripples and stator ohmic losses. Excitation currents for the healthy phases are calculated to produce the desired torque when a fault occurs. First of all, assuming that a fault occurs in a z^{th} phase, the following variables can be defined:

$$F = \begin{bmatrix} 1 \\ 1 \\ \vdots \\ 0 \\ \vdots \\ 1 \end{bmatrix} \quad Q = \begin{bmatrix} 1 & 0 & \cdots & 0 & \cdots & 0 \\ 0 & 1 & \cdots & 0 & \cdots & 0 \\ \vdots & \vdots & \ddots & \vdots & \vdots & \vdots \\ 0 & 0 & \cdots & 0 & \cdots & 0 \\ \vdots & \vdots & \vdots & \vdots & \cdots & \vdots \\ 0 & 0 & \cdots & 0 & \cdots & 1 \end{bmatrix} \quad e = \begin{bmatrix} e_1 \\ e_2 \\ \vdots \\ e_z \\ \vdots \\ e_n \end{bmatrix} \quad i = \begin{bmatrix} i_1 \\ i_2 \\ \vdots \\ i_z \\ \vdots \\ i_n \end{bmatrix} \tag{3.1}$$

$$n_H = F^T F \tag{3.2}$$

being F a fault matrix in which the ones indicate healthy phases and zeros faulty ones, Q a diagonal matrix with F in its diagonal, e is the back-EMF matrix and i is the phase currents matrix. Finally, n_H indicates the number of healthy phases. Then, assuming that a fault appears in only one phase, and taking into account the instantaneous power balance theory, the electrical power must match the mechanical

power:

$$T_e\omega = e^T Qi \tag{3.3}$$

where T_e is the electromechanical torque and ω stands for the mechanical speed of the rotor. To simplify the previous expression, the speed-normalized back-EMF, K can be defined as follows:

$$K = e/\omega = \begin{bmatrix} k_1 & k_2 & \cdots & k_z & \cdots & k_n \end{bmatrix}^T \tag{3.4}$$

Hence, the electromagnetic torque, T_e can be defined as:

$$T_e = K^T Qi \tag{3.5}$$

One of the goals of the control strategy is to minimize the torque ripple, it means to minimize the difference between the commanded torque and the electromagnetic torque. Hence, a constraint $g_1(i)$ for the minimum torque is defined:

$$T^* - K^T Qi = g_1(i) \tag{3.6}$$

Moreover, assuming that the common return path for the stator currents is absent, it means that the summation of phase currents equals zero, another constraint $g_2(i)$ can be defined:

$$F^T i = g_2(i) \tag{3.7}$$

Infinite solutions for the stator phase currents satisfying equations (3.6) and (3.7) can be found. However, by adding a minimization function, a unique solution might be obtained. This function will be developed so that the stator ohmic losses can be

minimized (it is considered that the stator phase resistances are equal).

$$\frac{1}{2}i^T i = h(i) \tag{3.8}$$

Now, the objective function f for the problem can be built. Then, the Lagrangian multipliers $p_1(i)$ and $p_2(i)$ for the constraints (3.6) and (3.7) are defined, so that:

$$f(i, p_1, p_2) = \frac{1}{2}i^T i + p_1(T^* - K^T Q i) + p_2 F^T i \tag{3.9}$$

Up to this point, it is needed to take the partial derivatives of f with respect to the phase currents, then equalising them to zero. This will allow to find the minimum condition of the objective function:

$$i = p_1 Q k - p_2 F \tag{3.10}$$

Combining (3.6), (3.7) and (3.10) the Lagrangian Multipliers can be obtained:

$$p_1 = \frac{n_H}{n_H K^T Q K - F^T Q K K^T Q F} \tag{3.11}$$

$$p_2 = \frac{F^T Q K}{n_H K^T Q K - F^T Q K K^T Q F} \tag{3.12}$$

Finally, if the previously calculated Lagrangian multipliers are replaced in (3.10), the stator phase current references that allow to match a certain torque command under an open phase fault can be expressed as:

$$i^* = \frac{n_H Q K - F^T Q K F}{n_H K^T Q K - F^T Q K K^T Q F} T^* \tag{3.13}$$

Once the current references have been obtained, several aspects must be taken into account. First, in (3.13) it can be seen how prior knowledge on the normalized back-EMF induced in the stator phases, K is needed. This can be achieved with a direct measure of the back-EMF at a known speed, or by using the PM flux linkage and

applying Faraday's equation:

$$K = \frac{e}{\omega} = \frac{d\phi}{d\theta} \tag{3.14}$$

Another aspect to consider is that the current analysis does not take into account any current per phase limit. Maximum phase current limit constraints might be added to the analysis in the derivation of the control technique to take this aspect into account.

Finally, the block diagram of the control scheme is shown in Fig. 3-2. Sensors are used to measure the phase currents, stator phase voltages and rotor position, in a way that they will allow to detect faults and carry out the machine control. Optimal current profiles under various fault conditions are calculated for a unique torque reference and stored offline in look-up tables. PI controllers are used to control the speed obtaining thus a certain torque reference. Depending on the fault condition, the look-up tables are used to generate the suitable current references. Eventually, hysteresis current controllers are used to generate the gate drive signals for the inverter that allow the stator currents to follow the desired current references.

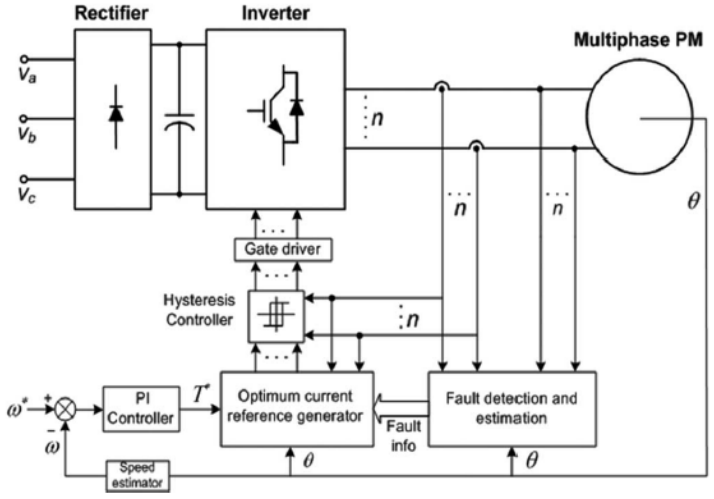

Figure 3-2: Block diagram for the proposed fault-tolerant control strategy [14]

Simulation and experimental tests were carried out to assess the performance of the control technique. For the experimental tests, a five-phase PMSM was used. Both

the simulation and the experimental results validate the feasibility of the described fault-tolerant control strategy.

3.2 Vectorial Approach For Generation of Optimal Current References (FTC-VA)

In the previous section, a method for generating optimal current references both in normal and in fault operation was explained. However, it was mentioned that current references were stored offline in look-up tables. In [7], it is proposed a vectorial approach to compute the aforementioned current references in real time. Unlike a scalar analysis like the previous one, the vectorial approach allows to reduce the number of computations so that current references can be obtained in real time. Moreover, as current references consist of expressions that depend on physical parameters, this control strategy can be also used to evaluate the influence of machine parameters in the control performance. In a vectorial way, electromagnetic torque, T can be expressed as follows:

$$T = \vec{\varepsilon} \cdot \vec{i} = \varepsilon^{\vec{a}cc} \cdot \vec{i} \tag{3.15}$$

being $\vec{\varepsilon}$ the speed normalized back-EMF (SN-BEMF) vector ($\vec{e}/\omega$), $\vec{i}$ the current vector, and $\varepsilon^{\vec{a}cc}$ the accessible SN-EMF vector, which actually corresponds to $\vec{\varepsilon}$ adapted to the dimensions of $\vec{i}$, since the current vector can have certain components imposed to zero due to constrains like a star connection or open-circuit phases. From a control point of view, the computation of a current reference from a torque one is given by:

$$\vec{i}^{*} = \vec{c} \cdot T^{*} \tag{3.16}$$

where $\vec{c}$ is a vectorial criterion that allows to obtain a vector $\vec{i}$ from a scalar T^{*}. This

criterion can be found by defining several constraints, being the balanced sinusoidal currents or the minimum copper losses the most common ones.

Following the Minimum Joule-Loss Criteria, the following expression is defined with aim of minimizing the instantaneous copper losses for a certain torque reference:

$$p_J(t) = R \min \|\vec{i}\|^2 = R \min \sum_{k=1}^{n} i_k^2 \tag{3.17}$$

For a given torque T, $\|\vec{i}\|$ is minimized when the scalar product $\vec{\varepsilon}^{acc} \cdot \vec{i}$ in (3.15) is maximized. This happens when $\vec{i}$ is collinear with $\vec{\varepsilon}^{acc}$.

$$\vec{i} = A \cdot \vec{\varepsilon}^{acc} \quad \text{A real} \tag{3.18}$$

Substituting (3.18) in (3.15), and assuming that one of the constraints is related with the minimization of the torque ripple, $T^* = T$:

$$A = \frac{T^*}{\|\vec{\varepsilon}^{acc}\|^2} \tag{3.19}$$

From this and (3.16) it is possible to define the criterion, $\vec{c}$:

$$\vec{c} = \frac{\vec{\varepsilon}^{acc}}{\|\vec{\varepsilon}^{acc}\|^2} \tag{3.20}$$

Finally, the current reference vector can be obtained like:

$$\vec{i}^* = \frac{\vec{\varepsilon}^{acc}}{\|\vec{\varepsilon}^{acc}\|^2} T^* \tag{3.21}$$

However, the goal of this control technique is to compute a vectorial criterion, $\vec{c}$ that allows to generate optimal current references whatever the mode of operation is (normal or with open-phases). Considering that the machine is star connected, one extra dimension is lost in the current vector. Moreover, the possible disconnection of a phase must be added to the analysis. Hence, the accessible SN-EMF, $\varepsilon^{\vec{acc}}$ must be

computed following the next expression:

$$\varepsilon^{\vec{acc}} = \varepsilon^{\vec{nc}} - \varepsilon^{\vec{z}} \tag{3.22}$$

where $\varepsilon^{\vec{nc}}$ is the accessible SN-EMF vector taking into account non-connected phases, and $\varepsilon^{\vec{z}}$ is a zero-sequence SN-EMF vector expressed in (3.25). This vector is obtained by projecting the accessible SN-EMF vector under non-connected phase topology onto the zero-sequence subspace generated by the star connection.

$$\varepsilon^{\vec{nc}} = \sum_{k=1}^{n} f_k \varepsilon_k \vec{x_k} \tag{3.23}$$

$$\vec{f} = \sum_{k=1}^{n} f_k \vec{x_k} \tag{3.24}$$

$$\varepsilon^{\vec{z}} = (\varepsilon^{\vec{nc}} \cdot \vec{x^z}) \vec{x^z} \tag{3.25}$$

Equation (3.26) shows how $\vec{x^z}$ is the unit zero-sequence vector that generates the zero-sequence subspace.

$$\vec{x^z} = \sum_{k=1}^{n} \frac{f_k \vec{x_k}}{\sqrt{\vec{f} \cdot \vec{f}}} \tag{3.26}$$

Then, the number of connected phases can be easily calculated by:

$$n - m = \vec{f} \cdot \vec{f} = \sum_{k=1}^{n} f_k \tag{3.27}$$

Finally, the current reference can be thus calculated in the following way:

$$\vec{i}^* = \frac{\vec{\varepsilon}^{acc}}{\|\vec{\varepsilon}^{acc}\|^2} T^* = \frac{\vec{\varepsilon}^{nc} - \vec{\varepsilon}^{z}}{\|\vec{\varepsilon}^{nc} - \vec{\varepsilon}^{z}\|^2} T^* \tag{3.28}$$

It may be seen how expressions (3.28) and (3.13), provide the same results, as [7] states. However, the proposed vectorial approach provides several advantages compared with the technique proposed in the previous section. The most remarkable

one is related with the computation time. As the control is carried out in a vectorial way, no matrices are used and hence computations are reduced. In this way it is possible to obtain the current references from a torque one in real time. This is a significant advantage for embedded systems with low memory capacity. Moreover, in (3.28), it can be seen how there is a direct link between the current reference expressions and the physical parameters of the machine (SN-EMF), which does not occur looking to (3.13). Scalar approaches store the computed current waveforms in memory to then send them to feedback controllers as references. With the vectorial approach current references are compute in real time.

The steps that have been followed in the previous lines are graphically represented in the block diagram shown in Fig. 3-3.

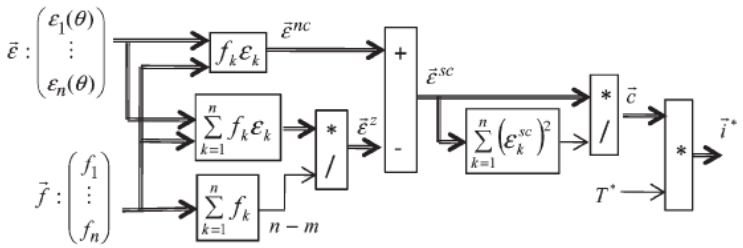

Figure 3-3: Block diagram of the proposed vectorial approach for optimal currents generation [7]

Moreover, Fig. 3-4 shows the control scheme of the whole system. It may be seen how it is quite similar to the one in Fig. 3-2 as the difference between both methodologies is related with the current reference computation.

It must be mentioned that this control strategy has some limitations. First, in particular fault cases, phase currents can have high-frequency components, which at the same time could lead to high core losses. Moreover, the proposed method is only feasible if there is no magnetic saturation, which is usually true when talking about surface PMSMs (SPMSMs).

The performance of the proposed strategy is tested both in simulation and with experimental tests. A five-phase surface-mounted permanent magnet synchronous

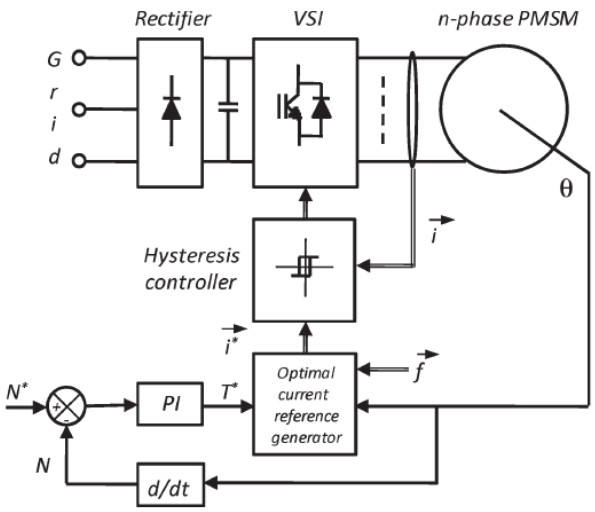

Figure 3-4: Block diagram for the control scheme of the whole system [7]

machine is used. Both simulation and experimental tests proved the feasibility of the proposed methodology. Optimal current references make possible to have even a smoother torque than in the normal mode.

3.3 Fault-Tolerant Control Based On Vector Space Decomposition (FTC-VSD)

In a multi-phase machine, when one of the phases is disconnected, undesirable current harmonics appear, leading to torque pulsations. In order to remove the mentioned current harmonics, the reference voltage vector can be synthesized through a kind of vector spaced decomposition-based space vector modulation (VSD-based SVM). This technique is developed in [16, 22, 23] for dual three-phase PM machines and in [15] for a six-phase induction machine. The dual three-phase PM machine is a non-linear high-order system, making the analysis harder. Vector space decomposition allows to decouple the voltage and current space vectors of the dual three-phase machine in three two-dimensional (2D) orthogonal subspaces [22]. The $\alpha - \beta$ subspace, also known as torque subspace is built by the fundamental components that participate in torque generation. The x-y subspace, known as harmonic subspace is formed by

the low-order harmonic components not participating in torque production. Finally, the zero-sequence subspace ϕ_1-ϕ_2 comprises the zero-sequence components [44]. The decomposition matrix for VSD in an asymmetrical dual three-phase machine (30° phase shift) looks like below [22]:

$$\begin{bmatrix} \alpha \\ \beta \\ x \\ y \\ \phi_1 \\ \phi_2 \end{bmatrix} = \frac{1}{6} \begin{bmatrix} 2 & -1 & -1 & \sqrt{3} & -\sqrt{3} & 0 \\ 0 & \sqrt{3} & -\sqrt{3} & 1 & 1 & -2 \\ 2 & -1 & -1 & -\sqrt{3} & \sqrt{3} & 0 \\ 0 & -\sqrt{3} & \sqrt{3} & 1 & 1 & -2 \\ 2 & 2 & 2 & 0 & 0 & 0 \\ 0 & 0 & 0 & 2 & 2 & 2 \end{bmatrix} \begin{bmatrix} A \\ B \\ C \\ D \\ E \\ F \end{bmatrix} \tag{3.29}$$

In [16, 22] VSD is used to analyse the effects of different faults. Actually, speed-sensor faults, voltage-sensor faults in the DC link, current-sensor faults and open-phase faults are studied. However, the different procedures are quite complex and as the scope of this Master Thesis is more focused in open phase faults, the different processes that are followed in this paper will not be analysed deeper. In fact, a much simpler control strategy that only takes into account the disconnection of one of the phases for a dual three-phase asymmetrical PMSM is carried out in [23]. Fig. 3-5 shows the studied machine fed through a voltage source inverter in healthy operation, while Fig. 3-6 shows the case of an open-circuit fault in phase F.

The stator voltage and flux equations for a PM machine are:

$$U_s = R_s I_s + \frac{d}{dt}\psi_s \tag{3.30}$$

$$\psi_s = L_s I_s + \gamma_s \Psi_m \tag{3.31}$$

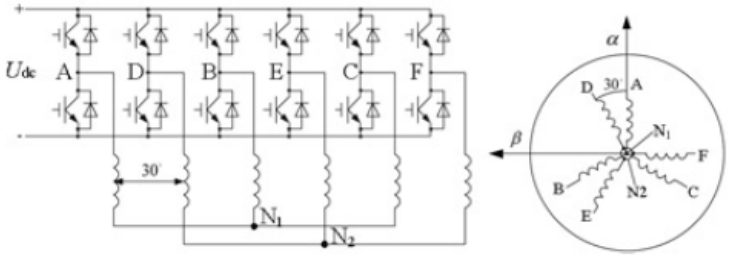

Figure 3-5: Dual three-phase PM machine fed by a voltage source inverter (VSI) [23]

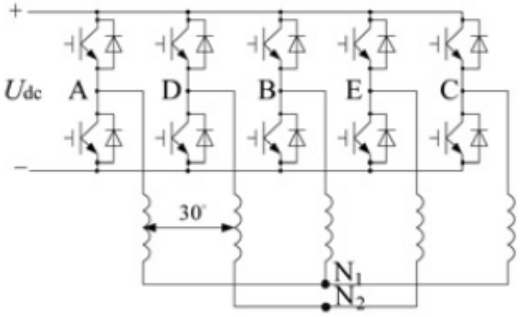

Figure 3-6: Dual three-phase PM machine fed by a voltage source inverter (VSI) with an open-circuit fault in phase F [23]

being,

$$U_s = \begin{bmatrix} u_A & u_B & u_C & u_D & u_E \end{bmatrix}^T$$

$$I_s = \begin{bmatrix} i_A & i_B & i_C & i_D & i_E \end{bmatrix}^T$$

$$\psi_s = \begin{bmatrix} \psi_A & \psi_B & \psi_C & \psi_D & \psi_E \end{bmatrix}^T$$

$$R_s = RI_5$$

$$\gamma_s = \begin{bmatrix} cos(\theta) & cos(\theta - \frac{2\pi}{3}) & cos(\theta - \frac{\pi}{6}) & cos(\theta - \frac{5\pi}{6}) & cos(\theta + \frac{\pi}{2}) \end{bmatrix}^T$$

Ψ_m is the PM flux linkage amplitude, γ_s the flux coefficient matrix, and I_5 the identity 5x5 matrix.

Up to this point, vector space decomposition can be applied. In order to do so, the

static decoupling transformation matrix under open phase faults must be expressed as shown below:

$$T_{5s} = \begin{bmatrix} \alpha & \beta & z_1 & z_2 & z_3 \end{bmatrix}^T \tag{3.32}$$

It may be seen that in this case, there is a missing dimension compared with (3.29). Components $\alpha - \beta$ are related with the torque generation. z_1 subspace stands for the harmonic components. $z_2 - z_3$ subspace is related with the zero-sequence components. It may be seen how, in this paper the harmonic subspace is uni-dimensional. As mentioned in [15], when having two isolated neutrals with a fault in phase F, the second component of the harmonic subspace is no longer controllable by the VSC (voltage source converter).

Following the winding space distribution, α and β can be obtained:

$$\begin{aligned} \alpha^T &= \begin{bmatrix} 1 & -\frac{1}{2} & -\frac{1}{2} & \frac{\sqrt{3}}{2} & -\frac{\sqrt{3}}{2} \end{bmatrix} \\ \beta^T &= \begin{bmatrix} 0 & \frac{\sqrt{3}}{2} & -\frac{\sqrt{3}}{2} & \frac{1}{2} & \frac{1}{2} \end{bmatrix} \end{aligned} \tag{3.33}$$

z_1, z_2, z_3, α and β must be orthogonal to each other:

$$\begin{aligned} &\alpha^T \cdot \beta = 0 \\ &\alpha^T \cdot z_1 = \beta^T \cdot z_1 = 0 \\ &\alpha^T \cdot z_2 = \beta^T \cdot z_2 = z_1^T \cdot z_2 = 0 \\ &\alpha^T \cdot z_3 = \beta^T \cdot z_3 = z_1^T \cdot z_3 = z_2^T \cdot z_3 = 0 \end{aligned} \tag{3.34}$$

There are several matrices that satisfy the previous expressions. Taking into ac-

count that as both neutrals are isolated, zero-sequence components can be avoided:

$$z_2 = \begin{bmatrix} 1 & 1 & 1 & 0 & 0 \end{bmatrix}^T$$
$$z_3 = \begin{bmatrix} 0 & 0 & 0 & 1 & 1 \end{bmatrix}^T$$

As it is noticed that β is not orthogonal to z_3, following the condition of $i_D + i_E = 0$, β can be changed to:

$$\beta^T = \begin{bmatrix} 0 & \frac{\sqrt{3}}{2} & -\frac{\sqrt{3}}{2} & 0 & 0 \end{bmatrix} \tag{3.35}$$

Finally, calculating z_1 in such a way that it fulfills (3.34), the static decoupling transformation matrix can be defined as:

$$T_{5s} = \frac{1}{3} \begin{bmatrix} 1 & -\frac{1}{2} & -\frac{1}{2} & \frac{\sqrt{3}}{2} & -\frac{\sqrt{3}}{2} \\ 0 & \frac{\sqrt{3}}{2} & -\frac{\sqrt{3}}{2} & 0 & 0 \\ 1 & -\frac{1}{2} & -\frac{1}{2} & -\frac{\sqrt{3}}{2} & \frac{\sqrt{3}}{2} \\ 1 & 1 & 1 & 0 & 0 \\ 0 & 0 & 0 & 1 & 1 \end{bmatrix} \tag{3.36}$$

Now, the $\alpha\beta$ to dq rotating transformation matrix, P_5 can be expressed as:

$$P_5 = \begin{bmatrix} cos(\theta) & sin(\theta) & 0 \\ -sin(\theta) & cos(\theta) & 0 \\ 0 & 0 & I_3 \end{bmatrix} \tag{3.37}$$

where I_3 is a three-dimensional unity matrix. Hence, the final transformation

matrix is:

$$T_5 = P_5 T_{5s} \tag{3.38}$$

Fig. 3-7 shows the schematic of the fault-tolerant control strategy. As there is no coupling between the z_1-axis and the dq subspace, the z_1 current controller can be designed independently. However, there is a strong coupling between the $d-$ and the $q-$axis. This coupling may be attenuated by modifying the voltage vector with matrix $A(\theta)$. In this way, the new voltage vector can be defined:

$$U_{d1q1} = A^{-1}(\theta) U_{dq} \tag{3.39}$$

being,

$$A(\theta) = \begin{bmatrix} 0.75 + 0.25cos(2\theta) & -0.25sin(2\theta) \\ -0.25sin(2\theta) & 0.75 - 0.25cos(2\theta) \end{bmatrix} \tag{3.40}$$

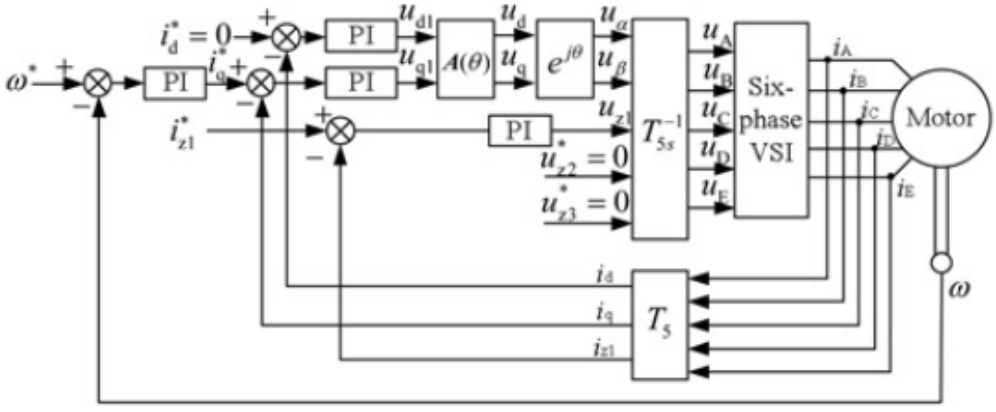

Figure 3-7: Control scheme for the fault-tolerant control of DT-PMSMs based on the reduced order mathematical model. [23]

Depending on the z_1 current reference, it is distinguished between the minimum

stator loss mode and maximum torque output. The feasibility of the proposed method is verified with a surface-mounted PM dual three-phase machine in a way that torque ripple is suppressed effectively while the reliability of the drive is improved.

In [24], the same control strategy is proposed. In this case the analysed machine has the neutral points connected between them and also to the medium point of the DC-link. This makes the transformation matrices change, as now the assumption of no zero-sequence current can not be applied. In any case, the procedure is the same and similar results are obtained.

3.4 Fault-Tolerant Control Strategy Based on Winding Compensation Through Machine Equations (FTC-WCME)

In previous sections it was mentioned that the simplest fault-tolerant technique when talking about multiple-three-phase winding machines consist of isolating the faulty winding, while the rest of them keep the operation. However, this supposes a reduction in the rated power and thus torque. Fault-tolerant control techniques try to take advantage of the healthy phases in the faulty winding to produce torque. A simple idea when talking about a dual three-phase machine consist of compensating the current harmonics in the faulty dq system with the healthy one. This idea is applied in [21, 25]. Four operation modes are described in [21]:

1. Normal mode: Both windings are healthy.
2. Isolated mode: When a fault occurs, the three-phase winding in which the fault is located is isolated, and the healthy is still used.
3. Loss mode: When a fault occurs, the remaining five phase currents are controlled in a way that copper losses are minimized.
4. Torque mode: When a fault occurs, the remaining five phase currents are controlled in a way that the torque capacity is maximized.

The total torque produced by the machine (surface-mounted PM dual three-phase synchronous machine) can be expressed as:

$$T_{e1} = \frac{3}{2} P \psi_{PM} i_{q1s} \tag{3.41}$$

$$T_{e2} = \frac{3}{2} P \psi_{PM} i_{q2s} \tag{3.42}$$

$$T_e = T_{e1} + T_{e2} \tag{3.43}$$

where T_{e12} is the torque generated respectively by winding 1 and 2, T_e is the total produced torque, P is the machine number of pole pairs, and ψ_{PM} is the PM flux linkage.

Up to this point, it is assumed that a fault occurs in phase A, so that $i_A = 0$. Hence:

$$i_B = -i_C = I_m \cdot cos(\theta_{e1} + \gamma_B) \tag{3.44}$$

In order to rotate to a synchronous reference frame, Park transformation is carried out, thus obtaining i_{d1s} and i_{q1s}:

$$P_{3/2}(\theta) = \frac{2}{3} \begin{bmatrix} cos(\theta) & cos(\theta - \frac{2\pi}{3}) & cos(\theta + \frac{2\pi}{3}) \\ -sin(\theta) & -sin(\theta - \frac{2\pi}{3}) & -sin(\theta + \frac{2\pi}{3}) \\ 0.5 & 0.5 & 0.5 \end{bmatrix}$$

$$i_{d1s} = \frac{I_m}{\sqrt{3}} [sin(2\theta_{e1} + \gamma_B) - sin(\gamma_B)]$$

$$i_{q1s} = \frac{I_m}{\sqrt{3}} [cos(2\theta_{e1} + \gamma_B) + cos(\gamma_B)] \tag{3.45}$$

In the previous equations it may be seen how torque can be maximized by setting

γ_B to 0:

$$
\begin{aligned}
i_{d1s} &= \frac{I_m}{\sqrt{3}} sin(2\theta_{e1}) \\
i_{q1s} &= \frac{I_m}{\sqrt{3}} [cos(2\theta_{e1}) + 1]
\end{aligned}
\tag{3.46}
$$

Here is seen how the double-frequency torque ripple appears when a phase is disconnected from the machine. By setting the dq_2 currents to a suitable value, this pulsations can be compensated:

$$
\begin{aligned}
i_{d2s} &= 0 \\
i_{q2s} &= I_T - \frac{I_m}{\sqrt{3}} [cos(2\theta_{e1}) + 1]
\end{aligned}
\tag{3.47}
$$

being,

$$
I_T = \frac{T_e}{\frac{3}{2} P \psi_{PM}} \tag{3.48}
$$

Once the current expressions are known, the loss mode strategy can be defined. System copper losses can be expressed as follows:

$$
p_{Cu} = 1.5 R_s [(i_{d1s}^2 + i_{q1s}^2) + (i_{d2s}^2 + i_{q2s}^2)] \tag{3.49}
$$

Replacing (3.46) and (3.47) in (3.49), the following expression may be obtained:

$$
\vec{p_{Cu}} = 1.5 I_T^2 R_s (\frac{7}{6} \eta^2 - 2\eta/\sqrt{3} + 1) \tag{3.50}
$$

Moving to the per-unit value of p_{Cu}:

$$
k_{Cu} = \frac{\vec{p_{Cu}}}{0.5 I_T^2 R_s} = 3.5\eta^2 - 2\sqrt{3}\eta + 3 \tag{3.51}
$$

Finally, according to [25], k_{Cu} is minimized when:

$$
\eta = \frac{I_m}{I_T} = \frac{2\sqrt{3}}{7} \tag{3.52}
$$

Once the loss mode has been defined, torque mode is proposed. In both normal and isolated modes, all phases have the same copper losses. In order to find out the actual situation of the phase copper losses when running in fault-tolerant mode, Park inverse transform is carried out:

$$\begin{aligned}
\bar{p}_B &= \bar{p}_C = \bar{i_C^2} R_s = 0.5\eta^2 I_T^2 R_s \\
\bar{p}_D &= \bar{i_D^2} R_s = \frac{I_T^2 R_s}{12}\{[3 - 2cos(2\Delta\theta)]\eta^2 - 2\sqrt{3}[2 - cos(2\Delta\theta)]\eta + 6\} \\
\bar{p}_E &= \bar{i_E^2} R_s = \frac{I_T^2 R_s}{12}\{[3 - 2cos(2\Delta\theta + \frac{2\pi}{3})]\eta^2 - 2\sqrt{3}[2 - cos(2\Delta\theta + \frac{2\pi}{3})]\eta + 6\} \\
\bar{p}_F &= \bar{i_F^2} R_s = \frac{I_T^2 R_s}{12}\{[3 - 2cos(2\Delta\theta - \frac{2\pi}{3})]\eta^2 - 2\sqrt{3}[2 - cos(2\Delta\theta - \frac{2\pi}{3})]\eta + 6\}
\end{aligned} \tag{3.53}$$

$$P_{2/3}(\theta) = \begin{bmatrix} cos(\theta) & -sin(\theta) \\ cos(\theta - \frac{2\pi}{3}) & -sin(\theta - \frac{2\pi}{3}) \\ cos(\theta + \frac{2\pi}{3}) & -sin(\theta + \frac{2\pi}{3}) \end{bmatrix} \tag{3.54}$$

Finally, equations in (3.53) are expressed in a per-unit way:

$$\begin{aligned}
k_B &= k_C = \frac{\bar{p}_B}{0.5 I_T^2 R_s} = \eta^2 \\
k_D &= \frac{\bar{p}_D}{0.5 I_T^2 R_s} = \frac{1}{6}\{[3 - 2cos(2\Delta\theta)]\eta^2 - 2\sqrt{3}[2 - cos(2\Delta\theta)]\eta + 6\} \\
k_E &= \frac{\bar{p}_E}{0.5 I_T^2 R_s} = \frac{1}{6}\{[3 - 2cos(2\Delta\theta + \frac{2\pi}{3})]\eta^2 - 2\sqrt{3}[2 - cos(2\Delta\theta + \frac{2\pi}{3})]\eta + 6\} \\
k_F &= \frac{\bar{p}_F}{0.5 I_T^2 R_s} = \frac{1}{6}\{[3 - 2cos(2\Delta\theta - \frac{2\pi}{3})]\eta^2 - 2\sqrt{3}[2 - cos(2\Delta\theta - \frac{2\pi}{3})]\eta + 6\}
\end{aligned} \tag{3.55}$$

The per-unit maximum phase copper loss, k_{max} is defined as:

$$k_{max} = max\{k_B, k_D, k_E, k_F\} \tag{3.56}$$

Maximizing the torque capacity means that k_{max} must be minimized. For a given $\Delta\theta$, $k_{max-min}$ is obtained when $\eta = \eta_{max-min}$. In [21] it is calculated that:

$$k_{max-min} = 0.4422 + 0.202 \cdot cos(2\alpha) \tag{3.57}$$

$$\eta_{max-min} = 0.672 + 0.13 \cdot cos(2\alpha) \tag{3.58}$$

with

$$\alpha = (\Delta\theta + \frac{\pi}{6})\text{mod}\frac{\pi}{3} - \frac{\pi}{6} \tag{3.59}$$

Summarizing, the feature of loss mode is $\eta = \frac{2\sqrt{3}}{7}$ while for torque mode it is $\eta = \eta_{max-min}$. Thus, torque mode and loss mode are two totally independent operation modes.

Once both methods are proposed, their effectiveness is tested in an experiment platform with a surface-mounted dual three-phase permanent magnet synchronous machine (DT-SPMSM). It is found that loss mode is preferred for light loads, while torque mode must be used when the load increases as torque can be increased around a 30%.

3.5 Fault-Tolerant Control Based On Preserving the Magneto Motive Force (FTC-MMF)

In general terms, a PM machine is mainly driven by the electromagnetic torque generated due to the interaction of the fundamental component of rotor and stator field. When operating in normal conditions, both fields rotate at the same speed so that a steady electromagnetic torque is produced. In addition, varying the stator phase currents allows to change the stator field in order to find certain control objectives. This idea is followed in [17] with aim of achieving a fault-tolerant control strategy. A surface-mounted six-phase PM machine in which the six phase windings

are symmetrically distributed around the stator is analysed. Then, the phase currents can be expressed as follows:

$$\begin{aligned} I_A &= Icos(\omega t) & I_B &= Icos(\omega t - 2\alpha) \\ I_C &= Icos(\omega t + 2\alpha) & I_D &= Icos(\omega t - \alpha) \\ I_E &= Icos(\omega t - 3\alpha) & I_F &= Icos(\omega t + \alpha) \end{aligned} \tag{3.60}$$

where α is equal to $\pi/3$, I represents the amplitude of the phase currents, and ω consists of the electrical frequency of the phase currents. Then, the magnetic motive force that each phase current produces can be calculated , and each of them can be divided in two different portions called positive and negative sequence of the MMF, as seen in (3.61):

$$MMF_i = MMF_i^+ + MMF_i^- \tag{3.61}$$

Subscript i, is used for representing each phase winding, while '+' and '-' indicate the positive or the negative sequence of MMF_i. The positive sequence of the magneto motive force is equal for the six-phase windings, both in amplitude and in phase, and can be calculated as:

$$MMF_i^+ = NIcos(\omega t - \theta)/2 \tag{3.62}$$

Hence, the positive sequence of the magneto motive force is equal to six times the positive sequence MMF of each phase. The magnetic field induced by the total positive sequence of the MMF will thus provide the motor with a steady average torque. Fig. 3-8 also shows this effect. In the other hand, the negative sequence of

the magneto motive force is not equal for all the phases, and will be expressed as:

$$
\begin{aligned}
MMF_A^- &= NIcos(\omega t + \theta)/2 \\
MMF_B^- &= NIcos(\omega t + \theta + 2\alpha)/2 \\
MMF_C^- &= NIcos(\omega t + \theta - 2\alpha)/2 \\
MMF_D^- &= NIcos(\omega t + \theta - 2\alpha)/2 \\
MMF_E^- &= NIcos(\omega t + \theta)/2 \\
MMF_F^- &= NIcos(\omega t + \theta + 2\alpha)/2
\end{aligned}
\tag{3.63}
$$

being N the total number of turns in each phase winding, and θ the spatial angle. Considering that MMF^+ rotates in the anticlockwise direction, Fig. 3-8 shows the distribution of MMF_i^+ and MMF_i^-.

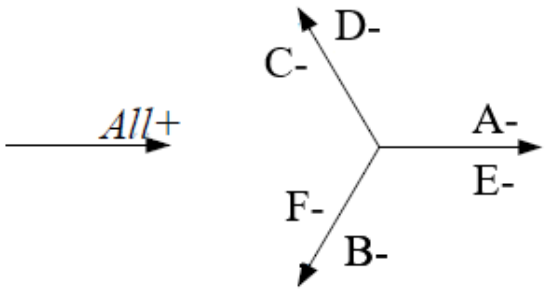

Figure 3-8: Distribution of positive (left) and negative (right) sequence of MMF under healthy condition [17]

It can be seen that MMF_i^- counteracts with each other, being the total sum of MMF^- equal to zero. This implies that torque is only produced by MMF^+ so that a constant electromagnetic torque is generated. Once the analysis for healthy operation is done, it must be repeated assuming an open-circuit fault in phase A.

When an open-circuit fault occurs in phase A, no current flows through that phase, and therefore $MMF_A^+ = MMF_A^- = 0$. Now, the total positive-sequence component of the magneto motive force is five sixth of that in healthy operation, so that the

produced torque is degraded. Moreover, the negative-sequence component of the MMF is not null any more but equals to $-MMF_A^-$, in a way that a magnetic field rotating in the opposite direction of the rotor field is induced. This effect leads to torque pulsations.

The mentioned paper proposes a fault-tolerant control strategy that allows to mitigate this effect. First, the neutral point of the machine windings is connected to the medium point of the DC-link. Besides, phase currents are independent of each other. This implies that the sum of all the phase currents equaling zero is not true any more. Hence, up to four-phase open-circuit faults can be tolerated. Once the faulty phases are detected, two constraints are adopted: the amplitude of each phase current should be the same, and the negative sequence of the magneto motive force should be zero. Now, under an open-circuit fault in phase A, the phase current expressions will be the following ones:

$$\begin{aligned} I_A &= 0 \\ I_B &= Icos(\omega t - 2\alpha + \theta_B) \\ I_C &= Icos(\omega t + 2\alpha + \theta_C) \\ I_D &= Icos(\omega t - \alpha + \theta_D) \\ I_E &= Icos(\omega t - 3\alpha + \theta_E) \\ I_F &= Icos(\omega t + \alpha + \theta_F) \end{aligned} \tag{3.64}$$

Fig. 3-9, shows how MMF_i^+ and MMF_i^- are distributed when an open-circuit fault occurs in phase A

Attending to this new distribution, the following system of equations can be devel-

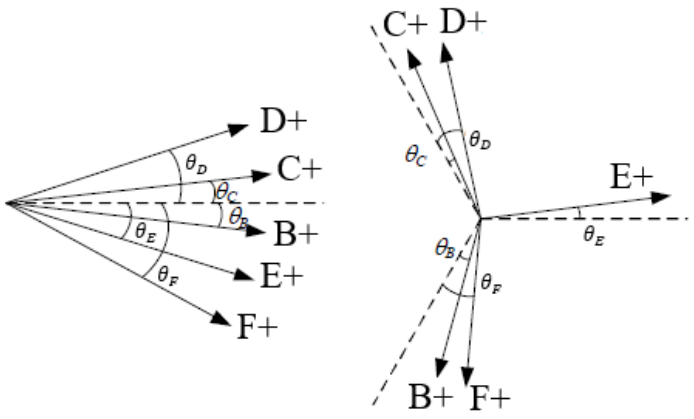

Figure 3-9: Distribution of positive (left) and negative (right) sequence of MMF under A-phase open-circuit fault condition [17]

oped:

$$\begin{aligned}
&\min -(cos\theta_B + cos\theta_C + cos\theta_D + cos\theta_E + cos\theta_F) \\
&sin\theta_B + sin\theta_E + sin\theta_F = sin\theta_C + sin\theta_D \\
&cos\theta_E = sin(\beta - \theta_B) + sin(\beta - \theta_C) + sin(\beta - \theta_D) + sin(\beta - \theta_F) \\
&sin\theta_E + cos(\beta - \theta_C) + cos(\beta - \theta_D) = cos(\beta - \theta_B) + cos(\beta - \theta_F)
\end{aligned} \tag{3.65}$$

Where $\beta = \pi/6$. With aim of maximizing the produced electromagnetic torque, the optimal function in (3.65) is to maximize the horizontal component of MMF_f^+, which is the positive-sequence of the MMF under faulty conditions. The first equation in (3.65) means that MMF_f^+ has no vertical component to preserve the same phase as in healthy condition. The last two equations mean that the negative-sequence of the total MMF, MMF_f^-, equals to zero to reduce the torque ripples. After solving the optimization problem with Matlab, the following results are obtained:

$$\begin{aligned}
&\theta_C = \theta_D = 0.271 \\
&\theta_B = \theta_F = -0.271 \\
&\theta_E = 0
\end{aligned} \tag{3.66}$$

With this solution, the obtained amplitude of MMF_f^+ is 0.809 times of MMF^+. Hence, only the 80.9% of the produced electromagnetic torque in healthy operation can be obtained.

In a similar way, the method can be applied when other open-circuit faults appear. Solving the obtained systems depending on the number of disconnected phases (the method can work up to four open-phase faults) with the help of Matlab, results in Table 3.3 are obtained.

Table 3.3: Calculation results for phase currents under each different fault condition [17]

Fault type	Angle to adjust					Torque output
	θ_B	θ_C	θ_D	θ_E	θ_F	
A	-τ	τ	τ	0	-τ	0.809
AY	-β	β	β		-β	0.577
AB		β	-β	β	-β	0.577
ABC			0	0	0	0.5
ABY		γ	-β		-β	0.289
ABZY						0
ABCY			β		-β	0.289

τ and γ are equal to 0.271 and $\pi/2$ respectively. Finally, the implemented control scheme is shown in Fig. 3-10.

It can be seen how currents are not controlled in the synchronous reference frame but each phase current is controlled. Hence, $e^{-j\theta}$ consists of the coordinate transformation under faulty conditions. This will vary for each situation specified in 3.3. For instance, for a open-circuit fault in phase A, the remaining phase currents will look

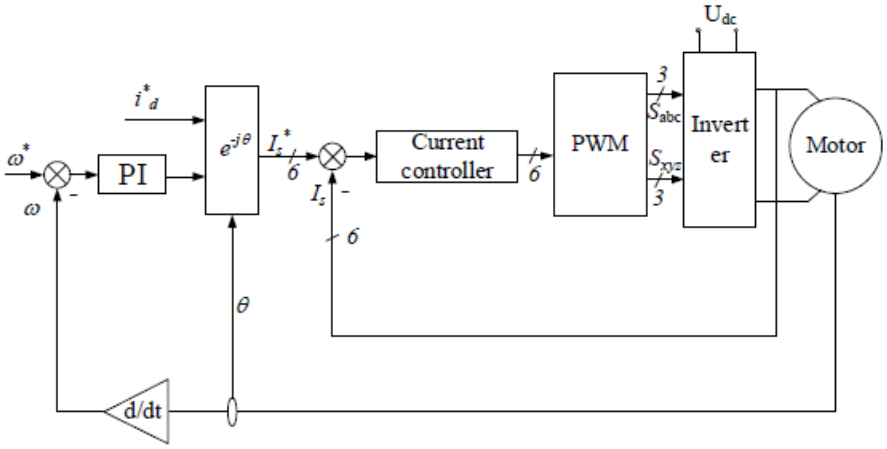

Figure 3-10: Fault-Tolerant Control Scheme for the Six-Phase SPMSM [17]

like:

$$
\begin{aligned}
I_B &= I_d cos(2\alpha - \theta_r + \tau) + I_q sin(2\alpha - \theta_r + \tau) \\
I_C &= I_d cos(-2\alpha - \theta_r - \tau) + I_q sin(-2\alpha - \theta_r - \tau) \\
I_D &= I_d cos(\alpha - \theta_r - \tau) + I_q sin(\alpha - \theta_r - \tau) \\
I_E &= I_d cos(3\alpha - \theta_r) + I_q sin(3\alpha - \theta_r) \\
I_F &= I_d cos(-\alpha - \theta_r + \tau) + I_q sin(-\alpha - \theta_r + \tau)
\end{aligned}
\tag{3.67}
$$

being θ_r the rotor position.

Finally, the paper analyses the effectiveness of the proposed technique in a Matlab/Simulink simulation, finding that the simulating results match with the theoretical analysis.

3.6 Fault-Tolerant Predictive Control (FT-PC)

One option when it is wanted to obtain a fault-tolerant control methodology for a multiphase machine consists of using a predictive model of the analysed machine. It must be mentioned that this technique is used for generating suitable gate commands once the optimal current references have been obtained following certain methods

as the ones proposed in previous sections. This concept is proposed in [26]. The mentioned paper analyses three different model predictive control (MPC) methods. The analysed machine consists of a six-phase surface-mounted PM machine. The analysis begins with the model of the machine in the pre-fault operation:

$$v_s = R_s i_s + L_s \frac{d}{dt} i_s + e_s \tag{3.68}$$

being v_s the phase voltage vector, R_s the resistance of each phase winding, i_s the vector of phase currents, e_s the vector of back-electromotive forces (back-EMFs) of all the phases, and L_s the phase inductance matrix.

Moving to the post-fault operation, it is assumed that an open-circuit fault occurs in phase F. By carrying out some simplifications that are more clearly specified in [26], equation (3.69) shows the mathematical model of the converter, indicating the relationship between the switching states and the machine phase voltages in fault operation:

$$v_{jn} = V_{dc} \cdot S_j - \frac{V_{dc}}{5} \cdot \sum_{j=A}^{E} S_j - \frac{v_{Fn}}{5} \tag{3.69}$$

However, this model shows that v_{Fn} creates a coupling relationship in the converter model, in a way that the remaining healthy phase voltages are also dependent on the faulty phase voltage in addition to the switching state of the power converter. This would complicate the prediction process. With aim of simplifying the predictive model, the virtual phase voltages V_{jn} are chosen to be the output of the converter for the advantage of no common-mode component. Thus, the simplified model of the converter will be:

$$v'_{s5} = V_{dc}/5 \cdot T_c \cdot S_5 \tag{3.70}$$

being:

$$v'_{s5} = \begin{bmatrix} v'_{An} & v'_{Bn} & v'_{Cn} & v'_{Dn} & v'_{En} \end{bmatrix} \tag{3.71}$$

$$S_5 = \begin{bmatrix} S_A & S_B & S_C & S_D & S_E \end{bmatrix} \tag{3.72}$$

$$T_c = \begin{bmatrix} 4 & -1 & -1 & -1 & -1 \\ -1 & 4 & -1 & -1 & -1 \\ -1 & -1 & 4 & -1 & -1 \\ -1 & -1 & -1 & 4 & -1 \\ -1 & -1 & -1 & -1 & 4 \end{bmatrix} \tag{3.73}$$

Substituting v'_{s5} in (3.68), (3.74) is obtained. The subscript $s5$ means that the dimension of the vector or the matrix is reduced from 6 to 5. The superscript $'$ means the parameter is modified from its original physical meaning.

$$v'_{s5} = R_s i_{s5} + L'_{s5} \frac{d}{dt} i_{s5} + e_{s5} + e_F \cdot A \tag{3.74}$$

where

$$A = 0.2 \cdot \begin{bmatrix} 1 & 1 & 1 & 1 & 1 \end{bmatrix}^T \tag{3.75}$$

Fig. 3-11 shows the control scheme of the proposed method.

Instantaneous reference currents, i^*_{s5} are obtained through fault-tolerant methods like minimum copper losses mode or maximum torque capacity mode, as explained in previous sections. Then the current control loop is carried out by predictive control strategies so that the optimized duty cycles of the five-phase legs (i.e. $D_5(k+1)$) in the following period can be obtained. Three different types of predictive current control can be distinguished depending on the modulation strategies: Conventional

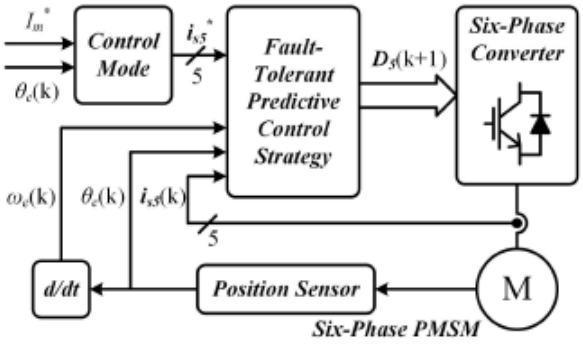

Figure 3-11: Block diagram scheme for the explained method [26]

Model Predictive Control (CMPC), Two-Vector-Based Predictive Control (TVPC) and PWM Predictive Control (PWMPC).

3.6.1 FT-CMPC

The following steps must be followed for implementing CMPC. First of all, the switching states must be transformed to phase voltages through (3.70). Then, the phase currents are predicted by the machine model (3.74). After that, a cost function is used to evaluate the optimum switching state. The optimized voltage vector is applied in the whole sampling period. With aim of implementing the mentioned control strategy in a digital processor, the models must be discretized. Being X the phase currents state vector, U the switching states input, B, C and F coefficient matrices, and U_{opt} the optimal voltage vector: Fig. 3-12(a) shows the total number of possible states. It can be seen how the cost function equals to the amplitude of the error $|X^{err}|$ between the reference state vector $|X^*(k+1)|$ and the i^{th} response vector $|X_i(k+1)|$. The smaller the error the closer to the optimum point. Fig. 3-12(b) shows the switching sequence in a sampling vector, while Fig. 3-12(c) summarizes the whole execution process.

3.6.2 FT-TVPC

As seen in Fig. 3-12(a), most of time there is a huge distance between the reference state and the state response of U_{opt}. The goal of FT-TVPC consists of adding an

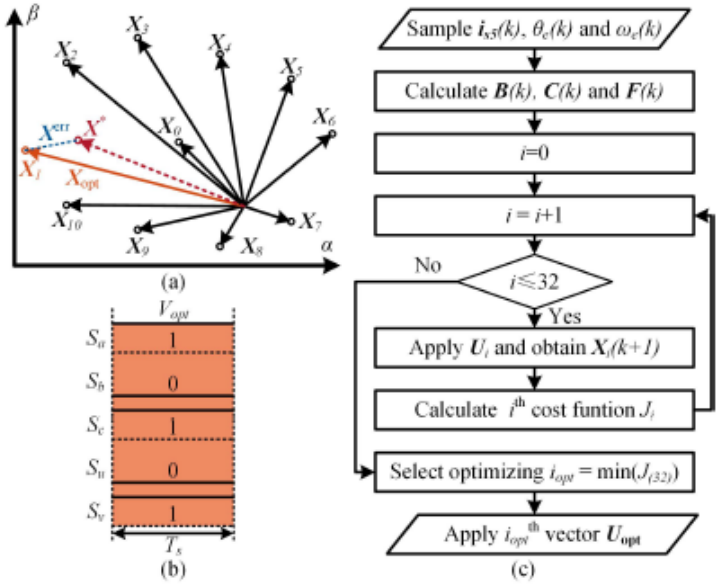

Figure 3-12: FT-CMPC main principles. (a) Vector diagram.(b) Switching sequence. (c) Execution procedure. [26]

extra zero voltage vector that allows to modulate with the optimizing vector, in a way that the phase currents can be closer to the reference values. This is illustrated in Fig. 3-13(a). Fig. 3-13(b) shows the switching pattern of phase legs in a sampling period and the work flow respectively, while Fig. 3-13(c) indicates the execution process of the method. In general, the synthesized voltages generated by FT-TVPC are preferable compared with FT-CMPC.

3.6.3 FT-PWMPC

When more than two voltage vectors are used in each sampling period, as shown in Fig. 3-14(a), it is quite hard for the conventional enumeration method with cost function to determine the optimizing vectors as well as their duration. FT-PWMPC is used for reversing the prediction procedure of CMPC, in such a way that the optimizing duty cycle is determined by substituting the reference phase currents $X(k+1)$ in the state equation. The execution procedure of the proposed FT method is shown in 3-14(b), which is more concise than the previously explained methods. The last outputs of the control methodology are the converter duty cycles. Fig. 3-14(c) shows

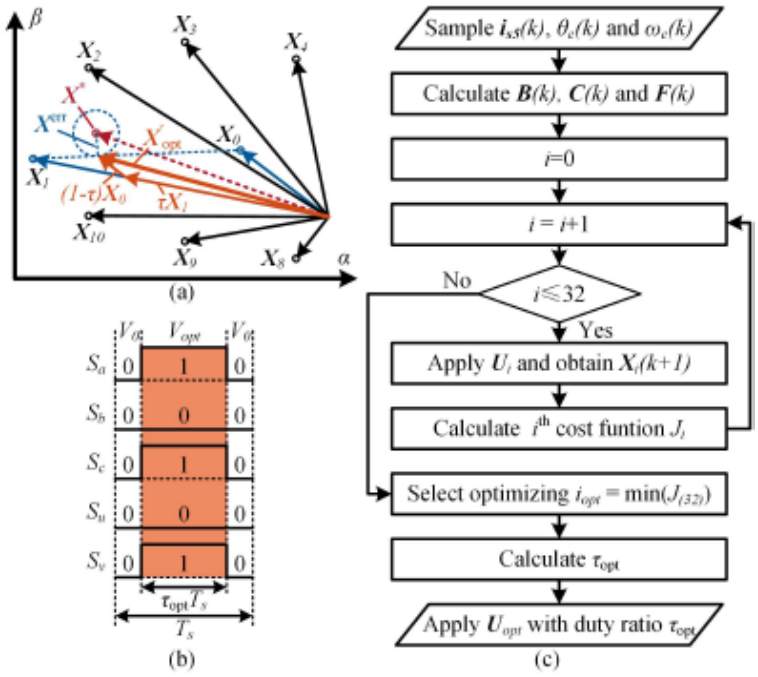

Figure 3-13: FT-TVPC main principles. (a) Vector diagram.(b) Switching sequence. (c) Execution procedure. [26]

the switching pattern of the PWMPC.

3.7 Proposed Fault-Tolerant Control Strategy Based on Winding Compensation Through Sensor Measurements (FTC-WCSM)

As mentioned in previous sections, a dual three-phase machine consists of a six-phase machine, whose phase windings can be split in two independent three-phase systems. Both three-phase windings can be connected (better means for fault-tolerant operation), or isolated (simplify controlability). However, in section 3.4, a FT control technique for a DT-PMSM with isolated neutral points is proposed. The technique principles consisted of compensating the faulty three-phase system with the healthy one. That process was done through machine equations. In this Master Thesis, a similar FTC strategy is proposed. This method allows to compensate the torque

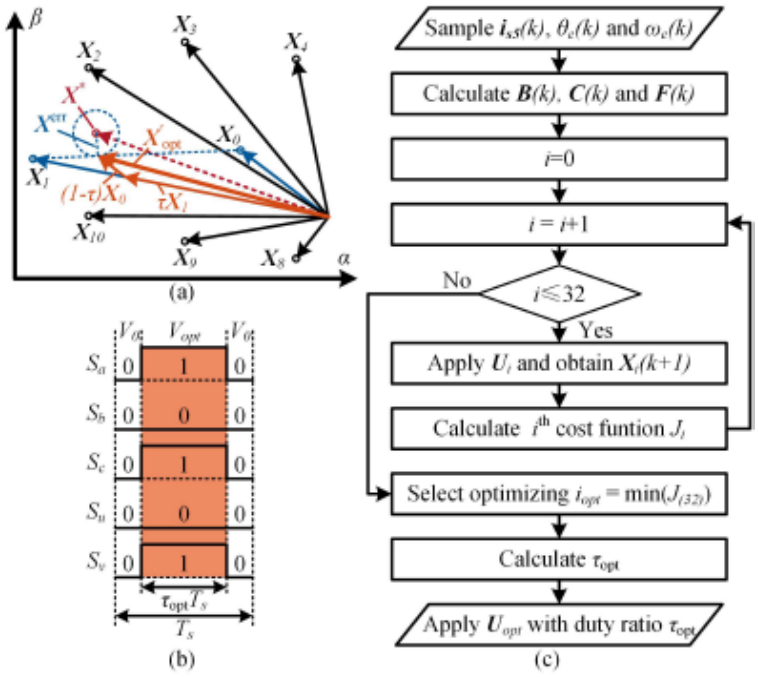

Figure 3-14: FT-PWMPC main principles. (a) Vector diagram.(b) Switching sequence. (c) Execution procedure. [26]

pulsations in a faulty three-phase set by adapting the current references of the healthy one. In order to do so, sensed current measurements are used. Current measurements allow to avoid all the mathematical calculations done in 3.4, being the implementation thus considerably simplified. As higher sensor accuracy as better fault compensation. Negative-sequence PI controllers must be added when increasing the rotating speed in order to track sinusoidal current references. The technique is limited to multi three-phase machines with isolated neutrals, and a perfectly healthy three-phase set is always required.

When controlling the machine with a digital signal processor (DSP), while measuring currents and voltages with sensors, it is possible to have that measurements available in real time through the microcontroller analog-to-digital converter (ADC). The suggested FTC technique is based on calculating the error between the $dq-$axis current reference and the real $dq-$axis current of the faulty three-phase winding so that the $dq-$axis current reference of the healthy winding can be modified in a way that the error is compensated. Therefore, this technique allows to keep constant the

total $dq-$axis current $(i_{dq1} + i_{dq2})$, and thus torque, despite the open-phase fault in one phase. Fig. 3-15 shows the control scheme of the proposed FT control technique.

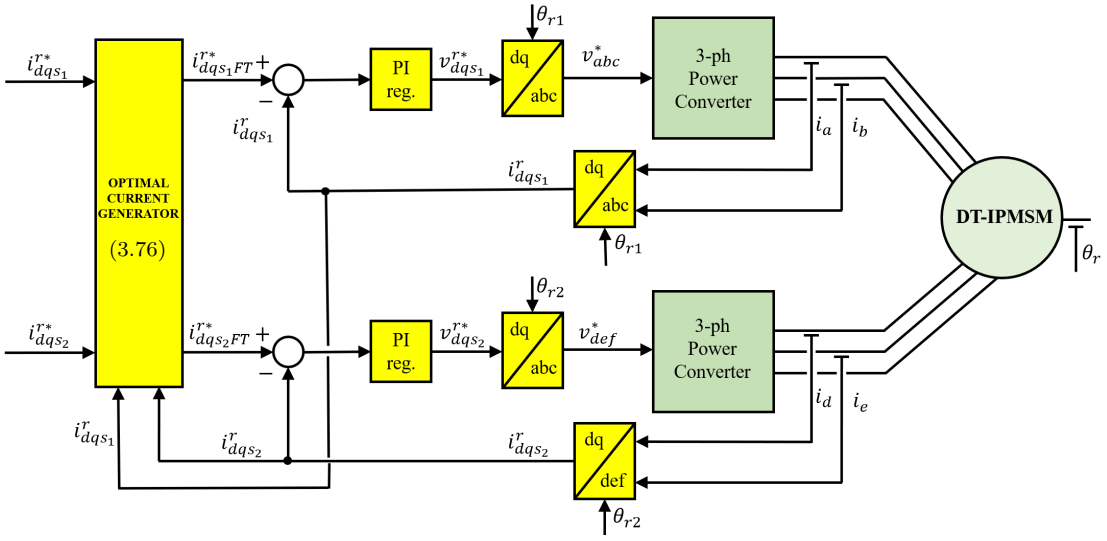

Figure 3-15: Control scheme of the proposed FTC technique

where θ_r is the rotor angle, θ_{r1} is the rotor angle respect to the first three-phase winding. If the rotor is initially aligned with phase A, $\theta_{r1} = \theta_r$. θ_{r2} is the rotor angle respect to the second three-phase winding, so that $\theta_{r2} = \theta_r + \theta_w$, where θ_w is the phase shift between both three-phase windings.

The key point of the FT control strategy is to generate the optimal current references for the healthy three-phase system when a fault is detected. Assuming an open-circuit fault in phase A, according to (3.46), the faulty $dq-$axis currents (i_{dqs_1}) will suffer double rotor frequency pulsations. Hence, the goal of the optimal currents generator will consist of varying the healthy $dq-$axis current references $(i^*_{dqs_2})$ so that the fault is compensated. This can be done in the following way:

$$\begin{aligned} i^*_{ds_2FT} &= i^*_{ds_2} + i^*_{ds_1} - i_{ds_1} \\ i^*_{qs_2FT} &= i^*_{qs_2} + i^*_{qs_1} - i_{qs_1} \end{aligned} \tag{3.76}$$

However, as seen in Fig. 3-15 and as explained below the mentioned FT control

strategy implies to control ac currents (pulsations due to the fault in the faulty winding and due to the error compensation in the healthy winding) with PI controllers. This will result on a poor performance. In [15], the use of dual PI/PR controllers is proposed. Fig. 3-16 shows the implementation of the dual PI:

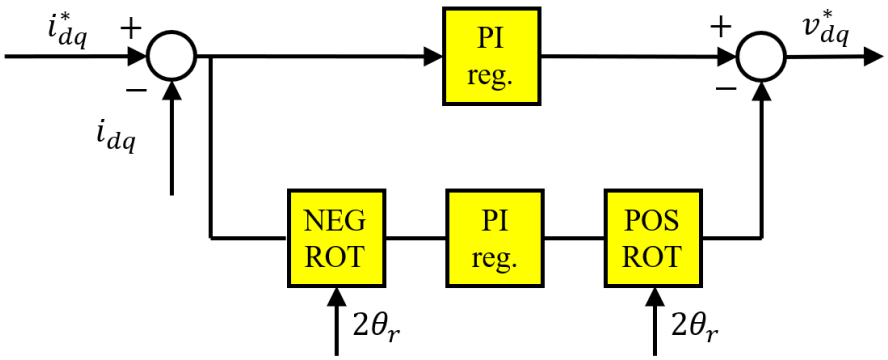

Figure 3-16: Dual PI implementation

It can be seen how, the first PI controller (top one) is in charge of controlling the positive sequence of current, while the second controller (bottom one) controls the negative sequence component of current. In order to do so, the current error is negatively rotated attending to double the rotor angle. Then, the controller control action is positively rotated attending to the same angle in order to recover the initial reference frame.

It must be mentioned that the proposed technique allows to keep the performance of the machine when a single-phase fault occurs in one of the three-phase windings. If two open-circuit faults occur in the same three-phase winding, no current would flow through it, and the current reference for the healthy three-phase winding would be doubled. This could cause currents above the rated values to flow through the healthy three-phase system phases. In this way, current limits can be incorporated in the optimal currents generator. Obviously, this will promote a reduction in the maximum achievable torque. If an open-circuit fault occurs in a phase of both three-phase windings, the proposed technique will not work.

3.8 Conclusions

In this chapter, several fault-tolerant control strategies proposed in literature have been described:

- Based on the instantaneous power balance theory, FTC-IPB assures the operation of the machine by calculating the excitation currents for the healthy phases that allow to keep the produced torque constant. Optimal current references are first calculated and then stored offline in look-up tables. Hysteresis controllers are used for tracking the current references. This fact makes the method not so suitable for its implementation, as for this Master Thesis, currents are wanted to be controlled in a synchronous reference frame with PI controllers.
- FTC-VA improves the performance of the previous described method, as it allows to obtain current references in real time. However, current is also controlled using hysteresis controllers. In addition, the technique is only feasible when there is no magnetic saturation, being this point usually fulfilled for SPMSMs but not for IPMSMs.
- Vector spaced decomposition-based space vector modulation (VSD-based SVM) is used for synthesizing a reference voltage vector so that the current harmonics promoted by an open-phase fault are removed (FTC-VSD). The method is feasible for DT-IPMSMs with isolated neutrals. Currents are controlled in a synchronous reference frame with PI controllers. These facts make the technique attractive to test in simulation and in the test-bench.
- Analyzing the machine equations when suffering an open-phase fault allows to compute the effects of the fault in the phase currents. When distinguishing between two three-phase sets, the healthy one can be used to compensate the error in the faulty one. FTC-WCME applies this technique by using the machine equations to estimate the new current reference for the healthy set that allows to compensate the faulty one. PI controllers are used. The technique can be feasible to implement in simulation and in the test-bench.

- When operating in normal conditions, the positive sequence of the magnetic motive force equals to six times the one of each phase, while the negative components of each phase counteracts with each other so that the sum equals zero. This does not happen any more when an open-phase fault occurs. FTC-MMF tries to mitigate this effect, forcing the sum of the negative-sequence of the MMF of each phase to be zero. Connection of the machine neutral point to the DC-link midpoint is required. This makes the technique not interesting at all for implementation in the test-bench, as isolated neutral points are preferred to simplify the control strategy. In addition, currents are not controlled in a synchronous reference frame with PI controllers.

- Another option for obtaining a FTC technique consists of developing predictive models of the studied machine. It allows to obtain adequate gate commands from the current reference. Three different methods are compared. CMPC, TVPC and PWMPC. However, an additional FT control strategy is required for generating optimal current references. The method is not designed for DT-IPMSMs with isolated neutral points but for six-phase PMSMs with connected neutral points. Implementation of cost functions in the algorithm raises the complexity of the method.

- Finally, FTC-WCSM is proposed. When an open-phase fault occurs, current pulsations (and thus torque) appear in the faulty three-phase system. This pulsations can be attenuated by compensating them with the healthy three-phase set. This was done in FT-WCME by using the machine equations. However, FTC-WCSM carries out the fault compensation by measuring the difference between the current reference and the actual one in the faulty set. Then, the current reference in the healthy system is varied attending to the error in the faulty one so that the pulsations are compensated, and constant torque is achieved. The technique is valid for DT-IPMSMs with isolated neutral points with single phase faults in one of the three-phase sets, making it feasible to implement in the test-bench.

Chapter 4

PM Temperature Estimation

4.1 Introduction

In this chapter, the effect of temperature variation in a PMSM will be discussed. Two temperature estimation methods will be presented: one for estimating the temperature of the permanent magnet (PM), and one for the differential PM temperature estimation.

4.1.1 Temperature dependence on PMSM torque

The performance of PMSMs is considerably affected by the PM temperature. An increase in the magnet temperature reduces the magnet strength [31–33, 45, 46], so that the torque capability of the machine is reduced. PM remanent flux, B_r typically decreases when the temperature is increased, promoting the mentioned drop of the PM strength. Equations (2.2), (2.3) and (2.4), show the expression of the torque produced by a PMSM, and how it can be split in two components: the reluctance torque, T_{re} and the electromagnetic torque, T_e. Both components are influenced by the rotor temperature.

Neodymium magnets, also known as NdFeB magnets are currently the most common choice in PMSMs thought other technologies such as ferrite, [47, 48], SmCo,

[49, 50] and AlNiCo magnets [51–53] can be also found. Table 4.1, [54], shows typical values of the PM thermal remanent flux coefficient, which is defined as the PM remanent flux rate of variation with temperature, α_B [31, 33, 34], PM remanent flux, B_r, and the operating temperature range for commonly used PM materials [54]. It is observed that the coefficient α_B strongly depends on the material; SmCo and AlNiCo magnets presenting low values of α_B [55], which means that the variation of their remanent flux (and hence torque) with temperature is relatively low. Consequently, for machines equipped with this type of magnets, precise estimation of the PM temperature is not a major concern. On the other hand, both ferrite and NdFeB magnets have high values of α_B, thus being the variation with temperature of their remanent flux considerably large. In this case, to carry out a precise control of the torque produced by machines that equip this type of magnets might require precise measurement/estimation of the magnet temperature.

Usually in NdFeB, up to 12% of the neodymium material can be replaced by dysprosium (Dy) [56], ot terbium (Tb), to preserve their magnetic properties at high temperature. However, as seen in Table 4.2, this action penalizes cost. Disprosium price can be up to 5 times higher than NdFeB, and terbium more than ten times. Due to this fact, the interest in the development of Dy- and Tb-free magnets has raised [57].

Table 4.1: Typical values of the PM thermal remanent flux coefficient.

PM material	$\alpha_B(\%/°C)$	$B_r(T)$	Operating Temperature Range (*)
Alnico 5-7	-0.02	1.35	4 K to 520 $°C$
Alnico 8	-0.01	0.85	4 K to 520 $°C$
Ferrite 8	-0.2	0.39	-40 $°C$ to 150 $°C$
Ferrite 9	-0.18	0.45	-40 $°C$ to 150 $°C$
SmCo 1:5	-0.045	0.90	4 K to 520 $°C$
SmCo 2:17	-0.035	1.10	4 K to 520 $°C$
NdFeB 33EH	-0.11	1.15	150 K to 200 $°C$
NdFeB 48M	-0.12	1.39	150 K to 100 $°C$

(*)°C and K are used as this is the format used by the manufacturer [54].

Ferrite, SmCo, AlNiCo or NdFeB permanent magnets can suffer irreversible demag-

netization under certain temperatures and loading (i.e. i_{qd} current) conditions. The effect of demagnetization in PMs has been widely studied [58–60]. Demagnetization is an effect that might appear locally (partial demagnetization), or globally (uniform demagnetization) [58]. The maximum temperature at which the machine can work is defined as the maximum temperature that the PM can withstand without suffering irreversible demagnetization. As seen in Table 4.1, the operating temperature of AlNiCo and SmCo PMs is wider compared with ferrite and NdFeB magnets. In each case, demagnetization due to temperature occurs at a well defined value, so that high accuracy in the estimation of temperature is required to prevent demagnetization if the machine is expected to operate at temperatures close to the temperature limit of the PMs. Thus, measurement or alternatively estimation of the PM's temperature is highly desirable for torque control/monitoring purposes and to prevent demagnetization [61–63].

Table 4.2: China's domestic price of materials contained in a majority of magnets. Source: Bomatec Newsletter September 2016

PM Material	Cost (RMB/Kg)	Cost trend (One year)	Conditions
Terbium metal	3600	↗	min. of 99% purity
Dysprosium metal	1700	⟶	min.of 99% purity
Neodymium metal	320	↗	min. of 99% purity
Samarium metal	87	⟶	min. of 99% purity
Cobalt metal	205	⟶	min. of 99.8% purity

4.1.2 Review of magnet temperature measurement methods

In practise, it is not easy to measure directly the temperature of a PM [64]. It implies modifications of the machine, thus reducing robustness, and typically needing additional electronics for conditioning and filtering, which increases cost [65, 66]. In this manner, PM temperature measurement systems are not usually implemented in standard machines, being their use limited to laboratory prototypes. Temperature measurement methods can use non-contact and contact type sensors. Next, both

types are briefly discussed.

a) Non-contact type sensors

Non-contact type sensors (i.e. IR) [31, 33] require the magnet surface to be visible. This is feasible in many SPMSM's designs, but is not possible in most of the IPMSM's designs. Further concerns related to this type of sensors include price, accuracy, reduced robustness and mounting issues. In [31], the use of an IR (infrared) camera was introduced. The measurement system was tested in two SPMSMs, in which the surface of the magnets was visible. The studied system required drilling the machine end frame in order to have visual access to the magnet, thus compromising the robustness of the machine. The IR camera measures the side face of the magnet, PM temperature distribution measurement in the axial direction not being hence possible. In [33] it is presented the use of an infrared thermometer in such a way that, although the cost was significantly reduced [31], the system also suffered the above mentioned limitations.

b) Contact type sensors

The use of contact-type sensors has been proposed with aim of overcoming some of the limitations of non-contact type sensors [28, 65–67]. Contact type sensors (e.g. PTC thermistors, thermocouples, etc.) stand in need of the use of slip rings and brushes, or alternatively of a wireless transmission system. The prototypes that have been developed up to date provide either a single measurement or the PM temperature distribution in one dimension, typically the axial direction. In [65], a measurement system of this type is analysed. Addressed to induction machines, the rotor was equipped with 6 thermocouples. The method was broadened to IPMSMs in [28, 66, 67]. Four thermocouples are used to measure the temperature at different points of the magnet. The remaining two thermocouples are used to measure the temperature at the rotor yoke. With this system it is possible to obtain information about the temperature distribution in two different points of the magnets. However, the method does not allow to measure asymmetries among poles.

4.1.3 Review of magnet temperature estimation methods

An alternative to PM temperature measurement is PM temperature estimation.

PM temperature estimation methods can be divided into thermal models [29, 30, 68–70], BEMF based methods [71–74] and methods based on the injection of some form of test signal [27, 28, 31, 33].

4.1.3.1 PM temperature estimation using thermal models

A thermal model consists of a set of thermal nodes, each of which stand for an uniform temperature region. The thermal nodes are connected through thermal resistances, which represent the heat transfer. In order to represent the machine power losses (i.e. copper, core and magnet losses), power sources are used, while the capability of storing heat for the different parts of the machine is represented by heat capacitors. Therefore, to build a thermal model requires knowledge of the geometry of both the rotor and the stator, the materials used and the cooling system. Consequently, a thermal model must be developed and calibrated for each specific machine [29, 75].

Thermal models are normally based on a 2D machine model, so that a constant temperature in the axial direction is assumed. Moreover, these models do not consider thermal asymmetries between magnets (e.g. due to lamination grain orientation). Greater precision would be obtained by using thermal 3D models, but its complexity would increase exponentially. Some of the factors that complicate the thermal modeling are, among others, the complex machine geometry, heterogeneous materials, and different modes of heat transfer [69]. Modeling the heat transfer toward the environment is a common problem for all machine types but it can be estimated using external sensors, as this is usually an accessible part.

4.1.3.2 PM temperature estimation using BEMF based methods

BEMF based methods estimate the magnet temperature from the rotor PM flux linkage, which is estimated from the machine terminal voltages and currents [71–74].

The physical principles of the magnet temperature estimation using the BEMF can be obtained from the fundamental model of a PMSM in the synchronous rotor reference frame, which is shown in equation (2.1).

The PM flux, λ_{PM} , only affects to the $q-$axis. Hence, for the estimation of the PM flux, and as result for temperature estimation, only the $q-$axis equation is required (4.1). In (4.1), R_{qs} is function of the stator temperature, T_s, λ_{PM} is function of the magnet temperature, T_r , while L_{ds} and L_{qs} are both function of T_r and i^r_{dqs} current. Therefore, equation (4.1) can be expressed as (4.2), from which the PM flux can be obtained as (4.3).

$$v^r_{qs} = R_{qs} i^r_{qs} + pL_{qs} i^r_{qs} + \omega_r L_{ds} i^r_{ds} + \lambda_{PM}\omega_r \tag{4.1}$$

$$v^r_{qs} = R_{qs(T_s)} i^r_{qs} + pL_{qs(T_r, i^r_{qs}, i^r_{ds})} i^r_{qs} + \omega_r L_{ds(T_r, i^r_q, i^r_d)} i^r_{ds} + \lambda_{PM(T_r)}\omega_r \tag{4.2}$$

$$\lambda_{PM(T_r)} = \frac{v^r_{qs} - \Big(R_{qs(T_s)} i^r_{qs} + pL_{qs(T_r, i^r_{qs}, i^r_{ds})} i^r_{qs} + \omega_r L_{ds(T_r, i^r_{qs}, i^r_{ds})} i^r_{ds}\Big)}{\omega_r} \tag{4.3}$$

$$\lambda_{PM(T_r)} = \lambda_{PM(T_0)}\Big(1 + \beta(T_r - T_0)\Big) \tag{4.4}$$

Equation (4.4) shows how the PM flux varies with temperature, being T_0 the room temperature and β is the magnet flux thermal coefficient. The magnet temperature, T_r is obtained from (4.4).

Obtaining $\lambda_{PM(T_r)}$ from (4.3) when the machine is rotating under no-load condition, i.e $i^r_{dq} = 0$, is relatively simple, and is given by (4.5). Otherwise, obtaining $\lambda_{PM(T_r)}$ when $i^r_{dq} \neq 0$ is not trivial, as knowledge of the stator temperature is needed to estimate the $q-$axis resistance variation using (4.6), where α_{cu} is the copper thermal resistive coefficient. Moreover, previous knowledge of d and $q-$ axis inductance maps is needed (i.e. variation of the d and $q-$axis inductance with i^r_{dq} to compensate their

effect in (4.2)-(4.3)) [71–74].

$$\lambda_{PM(T_r)} = \frac{v_{qs}^r}{\omega_r} \tag{4.5}$$

$$R_{qs(T_s)} = R_{qs(T_0)} + (1 + \alpha_{cu}(T_s - T_0)) \tag{4.6}$$

4.1.3.3 PM temperature estimation based on using signal injection

a) Magnet temperature estimation using rotating voltage injection

When feeding the stator of a PMSM with a high-frequency voltage, the magnet-flux-dependent term in (2.1) can be safely neglected, since it does not contain any high-frequency component, and the high-frequency model is obtained.

Subscript hf in (4.7) represents the high-frequency component of the corresponding machine parameters and variables. Therefore, if the frequency of the injected high-frequency signal is high enough compared to the rotor frequency, the rotor speed dependent terms in (4.7) can be safely neglected. An orientation threshold for this assumption can be $\omega_{hf} > \omega_r + 2\pi 500$. Then, a simplified high-frequency model like the one shown in (4.8) can be obtained.

$$\begin{bmatrix} v_{dshf}^r \\ v_{qshf}^r \end{bmatrix} = \begin{bmatrix} R_{dhf} & 0 \\ 0 & R_{qhf} \end{bmatrix} \begin{bmatrix} i_{dhf}^r \\ i_{qhf}^r \end{bmatrix} + p \begin{bmatrix} L_{dhf} & 0 \\ 0 & L_{qhf} \end{bmatrix} \begin{bmatrix} i_{dhf}^r \\ i_{qhf}^r \end{bmatrix} + \begin{bmatrix} 0 & -\omega_r L_{qhf} \\ \omega_r L_{dhf} & 0 \end{bmatrix} \begin{bmatrix} i_{dhf}^r \\ i_{qhf}^r \end{bmatrix} \tag{4.7}$$

$$\begin{bmatrix} v^r_{dhf} \\ v^r_{qhf} \end{bmatrix} = \begin{bmatrix} R_{dhf} & 0 \\ 0 & R_{qhf} \end{bmatrix} \begin{bmatrix} i^r_{dhf} \\ i^r_{qhf} \end{bmatrix} + p \begin{bmatrix} L_{dhf} & 0 \\ 0 & L_{qhf} \end{bmatrix} \begin{bmatrix} i^r_{dhf} \\ i^r_{qhf} \end{bmatrix} \tag{4.8}$$

The $d-$ and $q-$axis components of the high-frequency resistances, R_{dhf} and R_{qhf}, depend on both the stator and rotor high-frequency resistances (4.9), being R_{hf} ($d-$ or $q-$axis) the high-frequency resistance seen from the stator terminals, R_{shf} the stator circuit contribution to the high-frequency resistance and R_{rhf} ($d-$ or $q-$axis) the rotor high-frequency resistance reflected in the stator. Both the temperature of the stator and the rotor affect the corresponding resistances, as generically shown by (4.10). For the case of the stator $\alpha = \alpha_{cu}$, which is the copper thermal resistive coefficient (stator high-frequency resistance), while for the rotor case, $\alpha = \alpha_{mag}$, which is the magnet thermal resistive coefficient (rotor high-frequency resistance). $R(T_0)$ stands for the stator/rotor resistance at the room temperature. The magnet temperature will affect to the PM strength (4.11), where $B_r(T_0)$ is the remanent PM flux at the room temperature, T is the temperature, and T_0 is the room temperature.

$$R_{hf} = R_{shf} + R_{rhf} \tag{4.9}$$

$$R_T = R_{T_0} + (1 + \alpha(T - T_0)) \tag{4.10}$$

$$B_{rT} = B_{rT_0} + (1 + \alpha_{B(T)}(T - T_0)) \tag{4.11}$$

Combining (4.9) and (4.10), it is possible to express the high-frequency resistance seen at the stator terminals as (4.12) shows, being T_s and T_r the stator and rotor temperatures, respectively.

$$R_{hf}(T_s, T_r) = R_{shf(T_s)} + R_{rhf(T_r)} \tag{4.12}$$

As equation (4.12) shows, the magnet temperature can be estimated from the high-frequency resistance, as long as the high-frequency resistance of the machine at the room temperature and the stator temperature are known. During a commissioning process, the high-frequency resistance of the machine at the room temperature can be measured, while the stator temperature can be easily measured via a contact-type temperature sensor (e.g., thermocouple, resistance temperature detectors, etc.).

The high-frequency resistance may be estimated through different forms of high-frequency excitation. While all these methods respond to the same physical principles, differences will appear in their practical implementation and performance. The use of the rotating voltage injection has already been proposed [31] and is briefly described below for convenience.

When a rotating high-frequency voltage (4.13) is applied to the stator terminals of a PM machine, its high-frequency model is obtained by replacing the p operator in (4.7) by $j\omega_{hf}$, (4.14) being obtained. By solving (4.14), the stator high-frequency currents in the rotor synchronous reference frame (4.15) and (4.16) are obtained.

$$v^r_{dqhf} = V_{hf} e^{j\omega_{hf} t} \tag{4.13}$$

$$\begin{bmatrix} v^r_{dhf} \\ v^r_{qhf} \end{bmatrix} = \begin{bmatrix} R_{dhf} + j\omega_{hf} L_{dhf} & -\omega_r L_{qhf} \\ \omega_r L_{dhf} & R_{qhf} + j\omega_{hf} L_{qhf} \end{bmatrix} \begin{bmatrix} i^r_{dhf} \\ i^r_{qhf} \end{bmatrix} \tag{4.14}$$

$$i^r_{dhf} = \frac{v^r_{dhf} - \omega_r L_{dhf} i^r_{qhf}}{R_{qhf} + j\omega_{hf} L_{qhf}} \tag{4.15}$$

$$i^r_{qhf} = \left[v^r_{dhf} + \frac{\omega_r L_{qhf} v^r_{qhf}}{R_{qhf} + j\omega_{hf} L_{qhf}} \right] \frac{R_{qhf} + j\omega_{hf} L_{qhf}}{(R_{dhf} + j\omega_{hf} L_{dhf})(R_{qhf} + j\omega_{hf} L_{qhf}) + \omega_r^2 L_{dhf} L_{qhf}} \tag{4.16}$$

Obtaining R_{dhf} and R_{qhf} from (4.15) and (4.16) is not trivial. First, there is cross-coupling between the $d-$axis and the $q-$axis. Then, the high-frequency impedances L_{dhf} and L_{qhf} may vary with i^r_d and i^r_q currents when the machine is working under normal operating conditions. Besides, they are multiplied by the rotor speed. Equations (4.15) and (4.16) can be extremely simplified if it can be assumed that $\omega_{hf} \lll \omega_r$, i.e., the high-frequency signal has a frequency significantly larger than the rotor speed (e.g., $\omega_{hf} > \omega_r + 2\pi 500$) [32]. In this case, the off-diagonal terms in (4.14) can be neglected thus simplifying (4.15) and (4.16) to 4.17 and 4.18. In this case, R_{dhf} and R_{qhf} are obtained from the real part of the $d-$ and $q-$axis currents in (4.17) and (4.18) , respectively.

$$i^r_{dhf} = \frac{v^r_{dhf}}{R_{dhf} + j\omega_{hf} L_{dhf}} \tag{4.17}$$

$$i^r_{qhf} = \frac{v^r_{qhf}}{R_{qhf} + j\omega_{hf} L_{qhf}} \tag{4.18}$$

The aforementioned assumption, $\omega_{hf} \gg \omega_r$ may be realistic in SPMSMs but, in general, it cannot be applied to IPMSMs. In this type of machines, the magnets are buried in the rotor lamination, which means that a lower frequency can be needed for the signal to penetrate into the rotor lamination and excite the PMs. Moreover, IPMSMs are often designed to operate at high speeds, which places further restrictions to the assumption that $\omega_{hf} \gg \omega_r$. It is concluded that (4.17) and (4.18) cannot be generally applied to IPMSMs and (4.15) and (4.16) should be used instead to obtain R_{dhf} and R_{qhf}. This complicates the implementation, also significantly increasing the parameter sensitivity.

b) Magnet temperature estimation using pulse voltage injection

In [27, 28] a method to estimate the magnet temperature in PMSMs by exploiting the $d-$axis saturation effects in the steel stator core is developed. A voltage pulse is applied in the $d-$axis while the $d-$axis current is being measured. It is known that the $d-$axis inductance L_d depends heavily on the $d-$axis saturation level of the machine which at the same time is influenced by the magnetization level of the PMs. When a $d-$axis pulse voltage is injected in the stator terminals, it is possible to detect the variation of L_d by measuring the slope of the induced $d-$axis current (4.19). Hence, $d(i_d)/dt$ will change upon changes of the magnetization level of the PMs. This will be used as indicator for the PM temperature when the magnetization state is not influenced by other variables.

$$v_d = L_d \frac{di_d}{dt} \tag{4.19}$$

4.2 Magnet temperature estimation using d-axis pulsating signal injection

In the previous section, the use of a rotating high-frequency voltage injection for temperature estimation was analysed. In order to overcome the discussed limitations, pulsating high-frequency signals (i.e. voltage and current injection) can be used.

4.2.1 Magnet temperature estimation using $d-$axis pulsating current injection

This method is based on injecting a sinusoidal high-frequency current in the $d-$axis of a PMSM, whether it is a SPMSM or an IPMSM, forcing the high-frequency $q-$axis current to be zero (4.20). In order to control this high-frequency current, a proportional-integral (PI) controller would not be enough as it would lead to steady state errors. Hence, a resonant controller will be needed to be designed, in such a way that the resulting commanded high-frequency voltages will have the form shown by

(4.21). The voltage complex vector, $v^{r'}_{dqhf}$ (4.22) may be defined by taking the $d-$axis component of the obtained high-frequency voltage complex vector, v^{r*}_{dqhf} in (4.21). From (4.20) and (4.22), their respective positive ($i^{r'}_{dqhfpc}$ and $v^{r'}_{dqhfpc}$) and negative sequence ($i^{r'}_{dqhfnc}$ and $v^{r'}_{dqhfnc}$) components can be extracted, (4.23) and (4.24), each one having half the magnitude of the original signal. From (4.23) and (4.24), the $d-$axis impedance can be obtained,using either the positive or the negative sequence components (4.27), where φ_{Zd} (4.26) is the phase of the $d-$axis PMSM impedance (4.25).

$$i^{r*}_{dqhf} = \begin{bmatrix} i^{r*}_{dhf} \\ \\ i^{r*}_{qhf} \end{bmatrix} = \begin{bmatrix} I^{*}_{hf}\cos(\omega_{hf}t) \\ \\ 0 \end{bmatrix} \tag{4.20}$$

$$v^{r*}_{dqhf} = \begin{bmatrix} v^{r*}_{dhf} \\ \\ v^{r*}_{qhf} \end{bmatrix} = \begin{bmatrix} (R_{dhf} + j\omega_{hf}L_{dhf})i^{r}_{dhf} \\ \\ 0 \end{bmatrix} \tag{4.21}$$

$$\begin{aligned} v^{r'}_{dqhf} = \begin{bmatrix} v^{r*}_{dhf} \\ \\ 0 \end{bmatrix} &= \begin{bmatrix} (R_{dhf} + j\omega_{hf}L_{dhf})I^{*}_{hf}\cos(\omega_{hf}t) \\ \\ 0 \end{bmatrix} \\ &= \begin{bmatrix} V^{r'}_{dqhf}\cos(\omega_{hf}t + \varphi_{Zd}) \\ \\ 0 \end{bmatrix} \end{aligned} \tag{4.22}$$

$$i_{dhf}^{r*} = \frac{I_{hf}}{2} e^{j\omega_{hf}t} + \frac{I_{hf}}{2} e^{-j\omega_{hf}t} = i_{dqhfpc}^{r*} + i_{dqhfnc}^{r*} \tag{4.23}$$

$$v_{dhf}^{r*} = \frac{|v_{dqhf}^{r'}|}{2} e^{j(\omega_{hf}t - \varphi_{Zd})} + \frac{|v_{dqhf}^{r'}|}{2} e^{j(-\omega_{hf}t - \varphi_{Zd})} = v_{dqhfpc}^{r'} + v_{dqhfnc}^{r'} \tag{4.24}$$

$$Z_d = R_{dhf} + j\omega_{hf} L_{dhf} \tag{4.25}$$

$$\varphi_{Zd} = \tan^{-1}\left(\frac{\omega_{hf} L_{dhf}}{R_{dhf}}\right) \tag{4.26}$$

$$Z_d = R_{dhf} + j\omega_{hf} L_{dhf} = \frac{v_{dqhfpc}^{r'}}{i_{dqhfpc}^{r*}} = \frac{v_{dqhfnc}^{r'}}{i_{dqhfnc}^{r*}} \tag{4.27}$$

The overall $d-$axis resistance (4.28) can be split into the stator and rotor contributions $R_{dshf(T_s)}$ and $R_{drhf(T_r)}$ (4.29), which depend on the stator and rotor temperatures T_s and T_r, respectively.

$$R_{dhf} = Z_d \cos(\varphi_{Zd}) \tag{4.28}$$

$$R_{dhf(T_s,T_r)} = R_{dshf(T_s)} + R_{drhf(T_r)} \tag{4.29}$$

$$R_{dhf(T_s,T_r)} = R_{dshf(T_0)}(1 + \alpha_{cu}(T_s - T_0)) + R_{drhf(T_0)}(1 + \alpha_{mag}(T_r - T_0)) \tag{4.30}$$

Figure 4-1 shows the control scheme and the signal processing block diagrams needed for the temperature estimation when injecting a pulsating high-frequency current. In the current feedback, a band-stop filter ($BSF1$) is used with aim of preventing the fundamental current controller to react against the injected high-frequency current, while a band-pass filter ($BPF1$) is used to isolate the high-frequency component

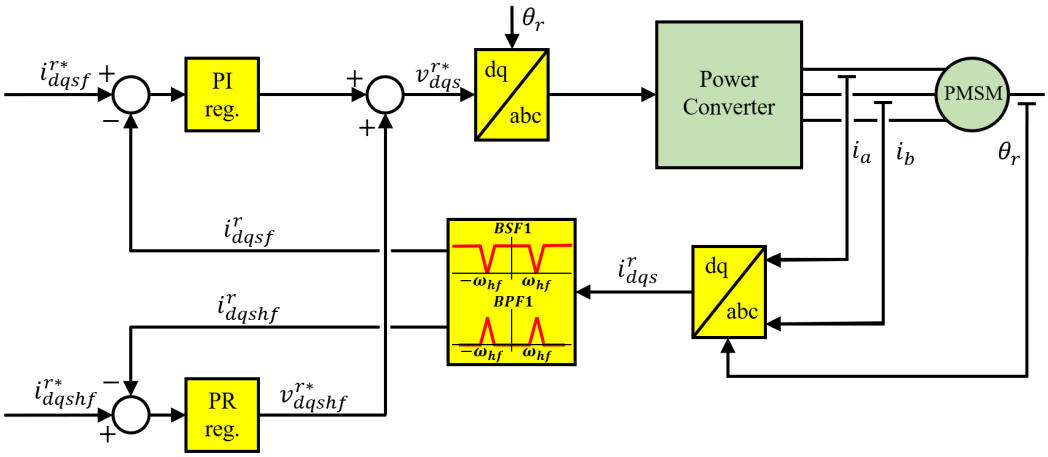

Figure 4-1: Implementation of the $d-$axis pulsating current injection

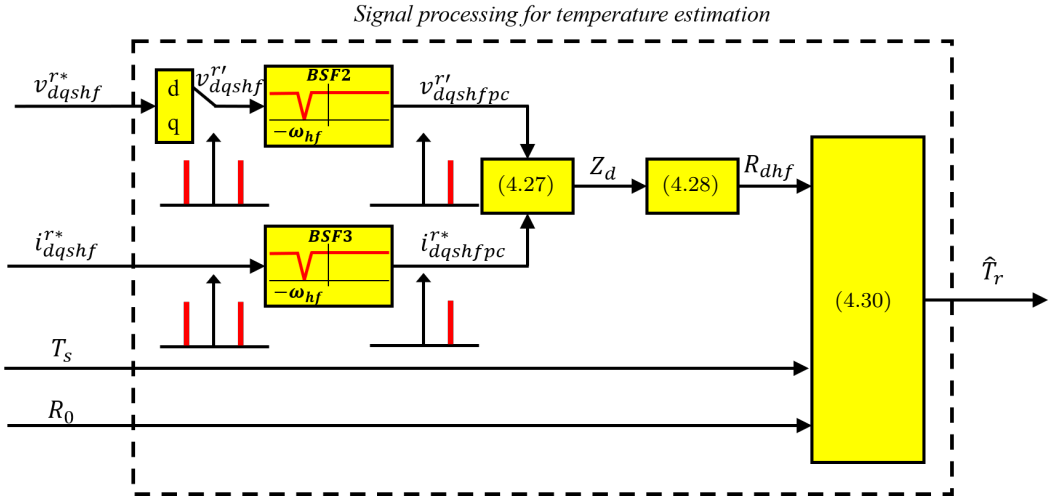

Figure 4-2: Signal processing for the $d-$axis pulsating current injection

of the overall stator current. As mentioned before, a high-frequency proportional-resonant (PR) current controller is designed for tracking the high-frequency component of current (4.31) with zero steady state error, being K_p the proportional gain, $\omega = \omega_{hf}$ the resonant frequency, and c the location of the zero of the controller.

$$PR(s) = K_p \frac{(s+c)^2 + \omega^2}{s^2 + \omega^2} \tag{4.31}$$

About the signal processing block diagram (see Fig. 4-2), their inputs consist of the output voltage of the high-frequency resonant controller, it means the control action of the resonant controller v^{r*}_{dqhf} (4.21), the high-frequency current command

i^{r*}_{dqhf} (4.20), the temperature in the stator T_s, and the stator resistance at the room temperature R_0. The $d-$axis impedance Z_d (4.25) is estimated from the positive sequence component of the commanded high-frequency current i^{r*}_{dqhf} (4.23) and the $d-$axis component of the high-frequency current resonant controller output voltage $v^{r'}_{dqhf}$ (4.24). In order to remove the negative sequence components, two band-stop filters are used ($BSF2$ and $BSF3$ in Fig.4-2). Finally, the magnet temperature can be estimated by combining equations (4.28) and (4.30).

4.2.2 Magnet temperature estimation using $d-$axis voltage injection and $q-$axis current cancellation

In the previous section, the injection of a sinusoidal high-frequency current in the $d-$axis, with the $q-$axis one being forced to be zero was proposed. However, it is possible to inject a high-frequency voltage in the $d-$axis instead of a high-frequency current. When injecting a high-frequency voltage signal in the $d-$axis (4.32), combined with the application of a current cancellation strategy applied to the $q-$axis (4.33), the obtained high-frequency current and voltage complex vectors, in the synchronous rotor reference frame, are respectively (4.35) and (4.34). If only the real part of (4.34) is taken, the resulting complex vector will be (4.36). Both (4.35) and (4.36) can be expressed as two rotating signals, having each of them half the amplitude of the original signal, with opposite rotating direction, (4.37) and (4.38), respectively. Then, the $d-$axis impedance can be obtained from (4.37) and (4.38) using either the positive or the negative sequence components (4.39).

$$v^{r*}_{drhf} = V_{hf}\cos(\omega_{hf}t) \tag{4.32}$$

$$i^{r*}_{qrhf} = 0 \tag{4.33}$$

$$v^r_{dqhf} = \begin{bmatrix} v^{r*}_{dhf} \\ \\ v^r_{qhf} \end{bmatrix} = \begin{bmatrix} V_{hf}\cos(\omega_{hf}t) \\ \\ \omega_r L_{dhf} i^{r*}_{dhf} \end{bmatrix} \tag{4.34}$$

$$i^r_{dqhf} = \begin{bmatrix} i^r_{dhf} \\ \\ i^{r'}_{qhf} \end{bmatrix} = \begin{bmatrix} V^r_{dhf}/(R_{dhf} + j\omega_{hf}L_{dhf}) \\ \\ 0 \end{bmatrix} \tag{4.35}$$

$$v^r_{dqhf} = \begin{bmatrix} v^{r*}_{dhf} \\ \\ v^r_{qhf} \end{bmatrix} = \begin{bmatrix} V_{hf}\cos(\omega_{hf}t) \\ \\ 0 \end{bmatrix} \tag{4.36}$$

$$i^r_{dqhf} = \frac{|i^r_{dhf}|}{2}e^{j\omega_{hf}t} + \frac{|i^r_{dhf}|}{2}e^{-j\omega_{hf}t} = i^r_{dqhfpc} + i^r_{dqhfnc} \tag{4.37}$$

$$v^{r*}_{dhf} = \frac{V_{hf}}{2}e^{j(\omega_{hf}t-\varphi_{Zd})} + \frac{V_{hf}}{2}e^{j(-\omega_{hf}t-\varphi_{Zd})} = v^{r'}_{dqhfpc} + v^{r'}_{dqhfnc} \tag{4.38}$$

$$Z_d = R_{dhf} + j\omega_{hf}L_{dhf} = \frac{v^{r'}_{dqhfpc}}{i^r_{dqhfpc}} = \frac{v^{r'}_{dqhfnc}}{i^r_{dqhfnc}} \tag{4.39}$$

Fig. 4-3 and Fig. 4-4 show the control scheme and the signal processing block diagrams needed for the temperature estimation when injecting a pulsating high-frequency voltage in the $d-$axis while applying a current cancellation strategy in the $q-$axis. As well as in Fig. 4-1, a band-stop filter ($BSF1$ in Fig. 4-3) is used in the fundamental current feedback control loop with aim of avoiding the current regulator to react against the high-frequency signal. Similarly, in order to isolate the

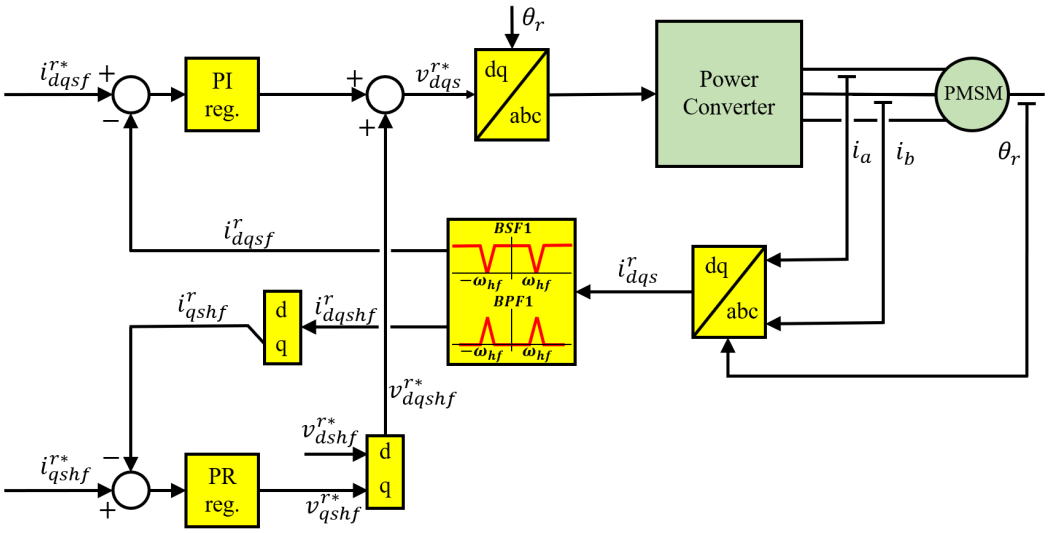

Figure 4-3: Implementation of the $d-$axis pulsating voltage injection with $q-$axis current cancellation

high-frequency current, a bandpass filter ($BPF1$ in Fig. 4-3) is used. Eventually, to assure that no high-frequency current circulates through the $q-$axis, a resonant controller, whose reference is (4.33) is used. The commanded $d-$axis high-frequency voltage v^{r*}_{dhf} is (4.32).

About the signal processing block diagram (see Fig. 4-4), their inputs consist of the commanded high-frequency voltage v^{r*}_{dhf}, (4.32), the obtained high-frequency current i^r_{dqhf} (4.35), the temperature in the stator T_s, and the resistance at the room temperature R_0. The $d-$axis impedance Z_d (4.39) is estimated from the positive sequence components of the obtained high-frequency current i^r_{dqhfpc} (4.37) and the $d-$axis high-frequency voltage command $v^{r'}_{dqhfpc}$ (4.38), which are obtained after removing the negative sequence components from the overall high-frequency current i^r_{dqhf} and voltage $v^{r'}_{dqhf}$, respectively. Finally, the magnet temperature can be estimated combining equations (4.28) and (4.30).

Although the methods described in sections 4.1.3.3, 4.2.1 and 4.2.2, are based on the same physical principles, there are differences in their performance that may be significant in practice. Equation (4.40) provides the relationship between the $d-$axis high-frequency voltage and current both for the case of pulsating $d-$axis high-frequency current injection (4.20) and for the case of $d-$axis high-frequency voltage

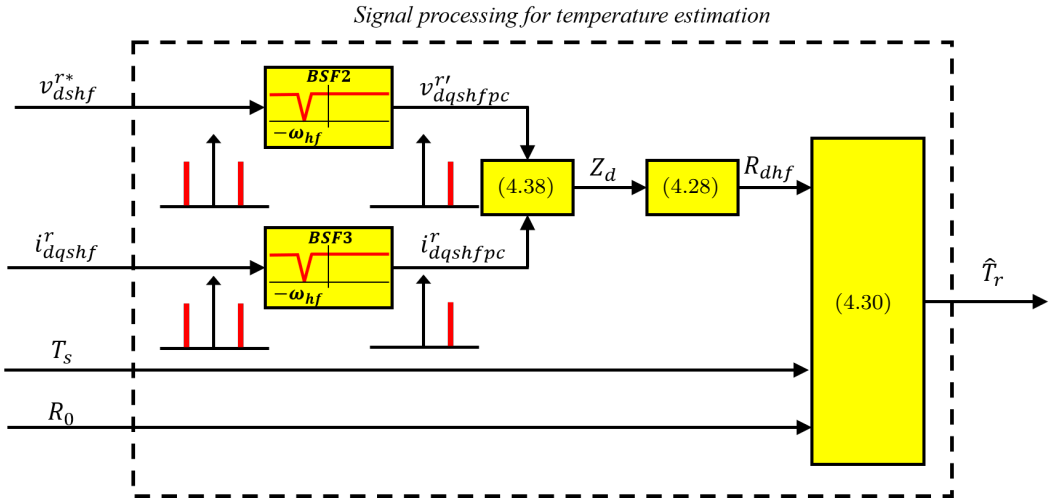

Figure 4-4: Signal processing for the $d-$axis pulsating current injection

injection, that were described in sections 4.2.1 and 4.2.2. On the other side, equation (4.16) establishes the relationship between the $d-$axis high-frequency voltage and current, for the case of a rotating high-frequency voltage injection (4.13) described in section 4.1.3.3. For the case of a pulsating $d-$axis voltage injection (4.41), the aforementioned relationship is given by (4.42).

$$i_{dhf}^{r*} = \frac{v_{dhf}^{r*}}{R_{dhf} + j\omega_{hf} L_{dhf}} \tag{4.40}$$

$$v_{dqhf}^{r*} = \begin{bmatrix} v_{dhf}^{r*} \\ \\ v_{qhf}^{r*} \end{bmatrix} = \begin{bmatrix} V_{hf}^{*} \cos(\omega_{hf} t) \\ \\ 0 \end{bmatrix} \tag{4.41}$$

$$i_{dhf}^{r} = \frac{v_{dhf}^{r*}(R_{qhf} + j\omega_{hf} L_{qhf})}{(R_{dhf} + j\omega_{hf} L_{dhf})(R_{qhf} + j\omega_{hf} L_{qhf}) + \omega_r^2 L_{dhf} L_{qhf}} \tag{4.42}$$

The benefits of injecting a $d-$axis pulsating high-frequency current or voltage com-

bined with a $q-$axis current cancellation strategy, against injecting whether a rotating voltage or a pulsating voltage become clear after analysing the previous equations. From (4.40) it may be observed that the resistive component of the high-frequency current (i.e., the component of the current in phase with the high-frequency voltage) only depends on the $d-$axis high-frequency resistance, so that it is not affected by the rotor speed or by the $d-$ and $q-$axis inductances. On the other hand, the resistive component of the obtained high-frequency current for the case of high-frequency voltage injection (either rotating (4.16), or pulsating (4.41)) given by (4.16) and (4.42), respectively, depends on the speed and on the inductances, in a way that the sensitivity of the method to the machine operating conditions raises.

4.2.3 High-frequency signal selection

Criteria for the selection of the magnitude and frequency of the injected high-frequency signal are discussed in this section.

a) Frequency Selection

Increasing the frequency will increase the spectral separation with the fundamental excitation frequency, making filtering easier. However, when frequency is increased, the weight of the inductive component (undesired component) will also increase over the resistive component (desired component) in the overall high-frequency impedance. In principal, low frequencies would be thus preferred.

a) Magnitude Selection

Increasing the magnitude of the injected high-frequency current is helpful for improving the accuracy of the method, as it increases the signal-to-noise ratio of the measured current signals. On the contrary, increasing the magnitude of the high-frequency current magnitude will increase the rotor and stator losses added to an increase in the acoustic noise and vibration.

4.3 PM temperature distribution estimation

In previous sections it was mentioned that the permanent magnets of a PMSM are exposed to irreversible demagnetization if their temperature exceeds the maximum one [31, 33]. The demagnetization process in a PM can be partial, if the spatial temperature distribution is not uniform [58, 76] or global [58], if the temperature throughout the magnet is uniform. In this way, the only estimation of the average temperature may be not enough in order to prevent demagnetization of the PMs. Moreover, to estimate the spatial temperature distribution can be used with aim of compensating the machine's torque ripple.

Temperature estimation methods explained in previous sections (i.e., BEMF based methods in section 4.1.3.2 and high-frequency resistance based methods in sections 4.1.3.3 and 4.2.1), provide a lumped temperature, but no information about the PM temperature spatial distribution.

In this section, the effect of a non-uniform magnet temperature distribution on the BEMF harmonics, added to its use for magnet differential temperature estimation issues will be analysed.

4.3.1 Temperature Estimation using BEMF

As mentioned, BEMF methods allow the estimate the magnet temperature from the PM flux linkage (λ_{PM}), which at the same time is obtained from the machine terminal currents and voltages. The PM flux is quite easy to obtain as long as $i_{dq} = 0$. However, whenever $i_d \neq 0$ or $i_q \neq 0$, the process becomes challenging. In this case, knowledge of several machine parameters is required (i.e. d and $q-$axis inductance maps with i_{dq}), so that the parameter sensitivity of the method raises. On the other hand, no additional signal needs to be injected.

Equation (2.1) shows the fundamental model of a PM machine in the synchronous rotor reference frame. For this method, only the $q-$axis voltage equation (4.1) is needed as the PM flux λ_{PM} is only present in the $q-$axis equation of the machine

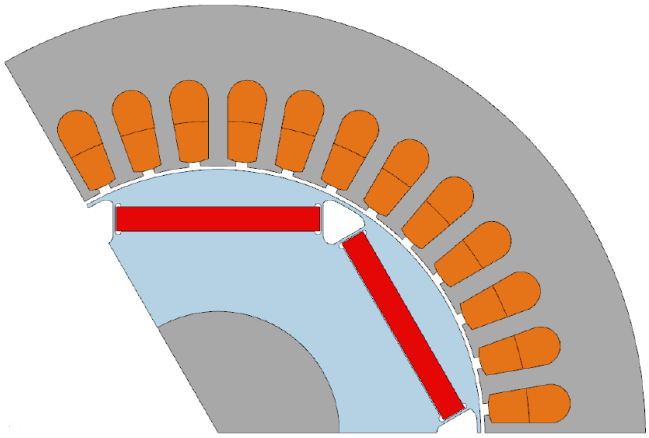

Figure 4-5: One thrid of the cross section of the IPMSM used for simulations and experimental results [77]

(2.1).

In (4.1), it may be seen how R_{qs} depends on the stator temperature, T_s, λ_{PM} is function of the magnet temperature, T_r, while L_{ds} and L_{qs} are both of them dependent on the rotor temperature, T_r, and on the d and $q-$axis currents, i_{dq}. Hence, (4.1) can be expressed as (4.2), so that λ_{PM} may be obtained following equation (4.3). Assuming that $i_{dq} = 0$, the PM flux can be obtained from (4.5). The variation of the PM flux with the magnet temperature can be expressed as (4.4), being T_0 the room temperature and β the magnet flux thermal coefficient. Eventually, using (4.43) the magnet temperature, T_r, can be obtained. However, as in the high-frequency signal injection methods, the estimated temperature is a lumped one, so that it does not provide any information about its spatial distribution.

$$[H]T_r = \frac{1}{\beta}\left[\frac{\lambda_{PM(T_r)}}{\lambda_{PM(T_0)}} - 1\right] + T_0 \tag{4.43}$$

4.3.2 Estimation of the magnet temperature distribution

Fig. 4-5 shows the IPMSM design used in [35] both for simulation and experimental verification. The machine has 36 slots and 6 poles, and is equipped with NdFeB magnets (N-42SH). Fig. 4-6(a) and Fig. 4-6(b) show the uniform and non-uniform

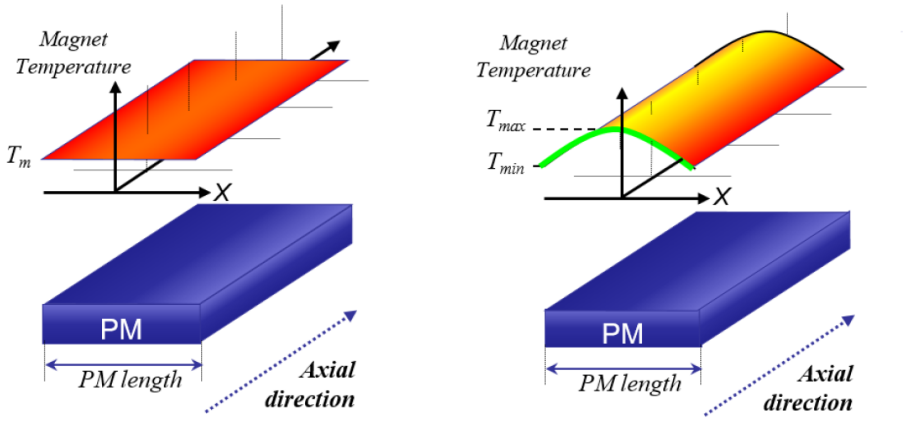

(a) Uniform Temperature Profile (b) Non-uniform Temperature Profile

Figure 4-6: Magnet temperature distribution [77]

temperature profiles considered, respectively . For the non-uniform temperature distribution, a quadratic law (4.44) was found to adequately fit with the temperature distribution experimentally measured. The PM dimensions in (4.44) are indicated in Fig. 4-6, where T_{min}, T_{max} and T_r are the minimum, maximum and mean PM temperature respectively, and PM_{length} is the permanent magnet length.

$$T_{magnet} = \frac{T_{min} - T_{max}}{(PM_{length}/2)^2} X^2 + T_{max} = \frac{T_{min} - T_{max}}{(PM_{length}/2)^2} X^2 + \left(T_r + \frac{T_{max} - T_{min}}{2} \right) \tag{4.44}$$

Magnet temperature distribution may be obtained using (4.44). To do so, the mean PM temperature T_r and the differential PM temperature T_{min}–T_{max} need to be estimated. Then, the different methods that allow this are shown.

4.3.3 Estimation of the mean magnet temperature

This section analyses how the mean PM temperature estimation using both BEMF (4.43) and a pulsating $d-$axis high-frequency current signal injection are evaluated [35]. Uniform and non-uniform temperature distribution cases are discussed. Finite

element analysis (FEA) are used for the analysis. Table 4.3 shows the temperature profiles that were used for simulation. In Fig. 4-7 the FFT of the BEMF for both the case of a uniform and a non-uniform magnet temperature distributions can be observed (see Table 4.3). The results are normalized in *per unit* (*p.u.*) with respect to the 1^{st} harmonic of the BEMF. A logarithmic scale is used for the magnitudes. While the harmonic content is the same for uniform and non-uniform temperature distributions, differences in the harmonic magnitudes can be appreciated. Three components of interest are observed: ω_r, $13\omega_r$ and $-11\omega_r$ harmonics [77].

Table 4.3: Case of study for different temperature distribution conditions [77]

Cases	Uniform Magnet temperature distribution	Non-uniform Magnet temperature distribution		
	$T_r(^\circ C)$	$T_{max}(^\circ C)$	$T_{min}(^\circ C)$	$T_r(^\circ C)$
1	100	100	100	100
2	90	100	90	94
3	80	100	80	88
4	70	100	70	82
5	60	100	60	76
6	50	100	50	70
7	–	100	40	64
8	–	100	30	58

Fig. 4-8 shows how the magnitude of the 1^{st} harmonic of the BEMF (component at ω_r, 50Hz), which corresponds to v_q^r in (4.5), varies with the mean magnet temperature, T_r (see Table 4.3). As predicted by (4.5)-(4.4), magnitude decreases as well as the mean magnet temperature increases. It is observed that independently of the magnet temperature distribution (uniform or not uniform), the same BEMF magnitude is induced. Hence, it may be concluded that the 1^{st} harmonic of the BEMF does not provide any information about the magnet temperature distribution. However, it can be used for mean PM temperature estimation.

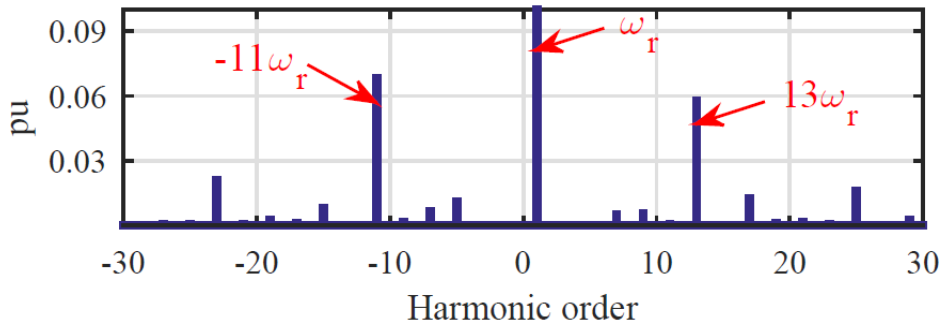

(a) Uniform magnet temperature distribution

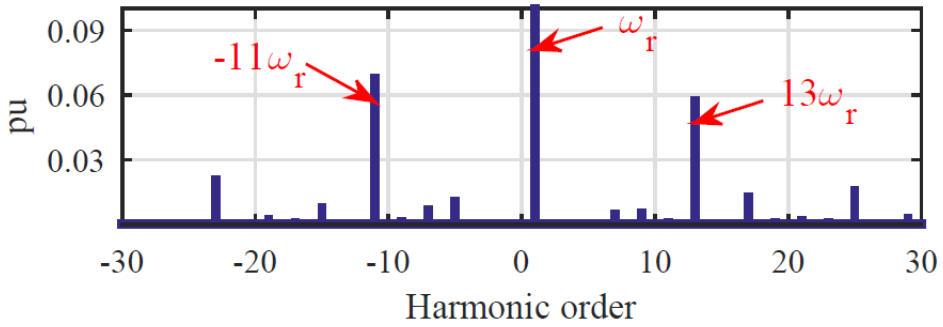

(b) Non-uniform magnet temperature distribution

Figure 4-7: BEMF frequency spectrum $\omega_r = 2\pi 50\ rad/s$ [77].

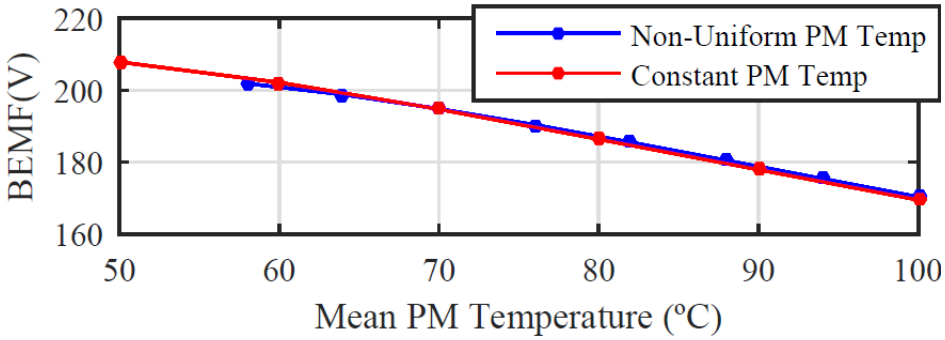

Figure 4-8: Fundamental component of the BEMF vs. mean magnet temperature. I_d= I_q=0 $p.u.$ and $\omega_r = 2\pi 50\ rad/s$ [77].

Fig. 4-9 shows the estimation of the rotor $d-$axis high-frequency resistance, R_{drhf} (T_r) (4.30), when injecting a pulsating $d-$axis high-frequency current, for the cases of a uniform and a non-uniform magnet temperature distribution. It is observed that its magnitude decreases as well as the mean magnet temperature decreases (see equation (4.30)). It is also seen that the variation of the estimated $d-$axis high-frequency resistance with the mean PM temperature is higher for the non-uniform magnet

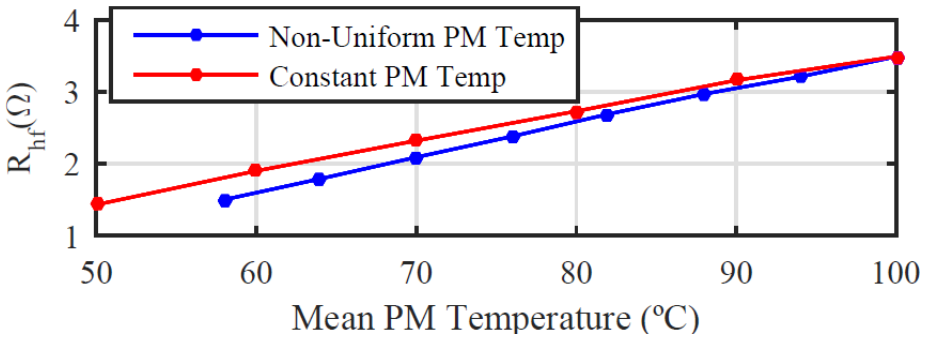

Figure 4-9: Estimated $d-$axis high-frequency resistance. Pulsating $d-$axis high frequency current injection, $\omega_{hf} = 2\pi 250\ rad/s$, I_{hf}=0.05 pu. I_d= I_q=0 $p.u.$ and $\omega_r = 2\pi 50\ rad/s$ [77].

temperature distribution case, compared to the uniform temperature distribution case. This means that different PM temperatures would be estimated for the same PM high-frequency resistance, so that an error would be thus induced in the estimated temperature. This variation could be potentially used with aim of estimating the differential magnet temperature T_{min}-T_{max}. This is an ongoing research topic.

4.3.4 Differential magnet temperature estimation

This subsection is devoted to analyse the differential PM temperature estimation using the BEMF harmonics. Simulation details are the same as the ones for mean PM temperature estimation. In Fig. 4-7 it may be seen the frequency spectrum of the BEMF, where three components of interest are observed: ω_r, $13\omega_r$ and -$11\omega_r$. As it was analysed in the previous subsection, the component at ω_r does not provide any information of the differential PM temperature; however, it can be used to estimate the mean PM temperature. On the other hand, $13\omega_r$ and -$11\omega_r$ harmonics can be used for PM differential temperature estimation. This will be analysed following.

Fig. 4-10(a) shows the magnitude of the BEMF 13^{th} harmonic (see Fig. 4-7), depending on the mean magnet temperature, while Fig. 4-10(b) shows the same harmonic as a function of the BEMF's fundamental component. The $p.u.$ value of the 13^{th} respect to the fundamental component of the BEMF is shown in both cases. This normalization is carried out in order to compensate the effects of the

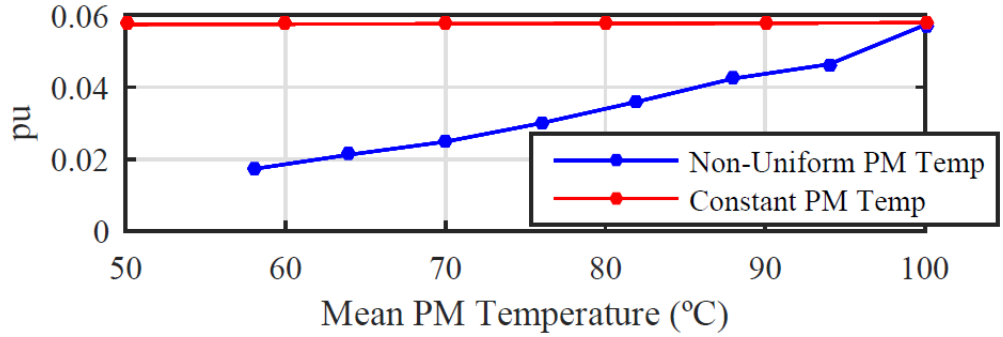

(a) BEMF 13^{th} harmonic magnitude vs. mean magnet temperature

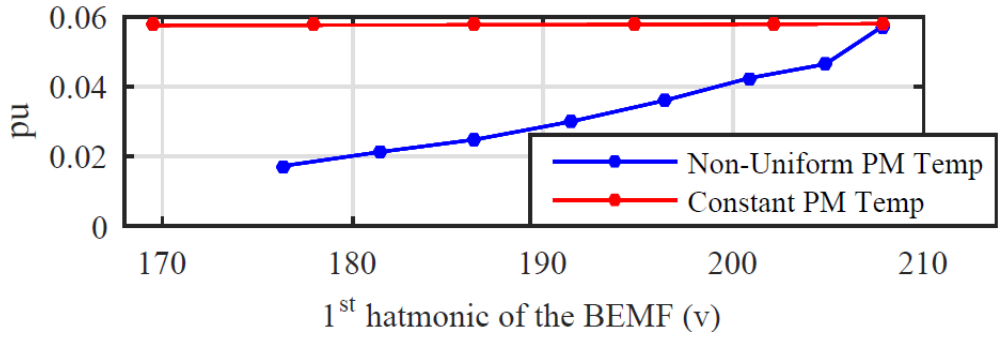

(b) BEMF 13^{th} harmonic magnitude vs. the 1^{st} harmonic magnitude of the BEMF.

Figure 4-10: BEMF 13^{th} harmonic magnitude vs. mean magnet temperature and vs. the 1^{st} harmonic magnitude of the BEMF. ω_r =2π 50 rad/s [77].

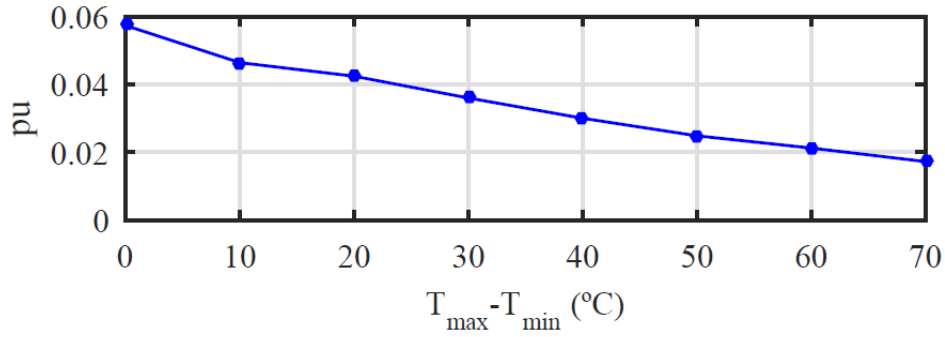

Figure 4-11: Back-EMF 13^{th} harmonic magnitude vs. differential magnet temperature, i.e. (T_{max}-T_{min}). $\omega_r = 2\pi 50\ rad/s$ [77].

average temperature variation. From Fig. 4-10, it may be seen that for the case of a uniform magnet temperature distribution, the relative magnitude of the 13^{th} harmonic is almost insensitive to the variations of the mean magnet temperature and of the fundamental component of the BEMF. On the other side, it is observed that the 13^{th} harmonic magnitude raises with the mean magnet temperature for the case of the non-uniform magnet temperature distribution, as well as with the magnitude of the BEMF's fundamental component. As a consequence, the *p.u.* value of the 13^{th} harmonic decreases as T_{max}-T_{min} increases. As different behaviors of the 13^{th} harmonic are obtained for the case of a uniform and a non-uniform temperature distribution, it can be potentially used to estimate the differential temperature due to a non-uniform magnet temperature distribution.

Fig. 4-11 shows the 13^{th} harmonic component magnitude vs. the differential magnet temperature, i.e. T_{max}-T_{min}, for the case of non-uniform temperature distribution. It can be observed that the magnitude varies almost linearly with the differential temperature. This relationship can be used to estimate T_{max}-T_{min}, which combined with the mean PM temperature, T_r allows to obtain an estimation of the magnet temperature distribution from (4.44). As shown before, T_r can be estimated either by injecting a high-frequency signal (see Fig. 4-9), or from the fundamental component of the BEMF (see Fig. 4-8 and (4.43)). It may be observed that although the 13^{th} harmonic of the BEMF has been used in the previous discussion, the 11^{th} harmonic seems to have a similar behavior. Although higher order harmonics could be also used, the magnitude of the voltage harmonic decreases with the harmonic order. Then, the signal-to-noise ratio is reduced, thus compromising the accuracy of the method.

Chapter 5

Simulations

Prior to experimental testing, it is advisable to check in simulation the correct implementation of the desired control technique as well as a suitable performance of the machine under that control strategy. With this aim, Matlab and Simulink are going to be used. First, the model of the DT-IPMSM must be included in the simulation. The closer the simulation model gets to the real machine, the more similar will be the obtained results to the experimental ones. Thus, the Simulink model of the machine will be carried out following the dynamic model described in section 2.2.2. Likewise, to implement the control strategy in the simulation in a similar way that it will be done in the microcontroller for the experimental tests will facilitate the transition from simulation to reality. Fig. 5-1 shows how the simulation looks in the Simulink interface. First, the inverter is fed with a DC voltage source. Then, the six phases of the inverter are connected to the machine. Inside the model of the machine, each phase will have a current source connected in series, being them connected building two stars. In addition, the phase voltages are measured. Applying (2.8) and (2.9) the synchronous reference frame voltages of both three-phase systems are obtained. Then, (2.5) and (2.6) build the electrical model of the machine and allow to compute the synchronous reference frame currents. Next, the synchronous currents are transformed to $abc - def$ coordinates, (2.10), (2.11), so that the phase currents are obtained. These phase currents will drive the previously mentioned

current sources. Finally, torque will be calculated with (2.7). About the mechanical model of the machine, speed will be fixed by a load machine so that DT-IPMSM angle will be simply computed integrating this speed (2.14).

About the control scheme, C-Caller block allows to implement the control strategy in C-code as well as will be done in Code Composer Studio for the experimental tests. Inputs to the C-Caller block are the analog measurements, as well as the created input variables in the real implementation. The outputs of this block are the six PWM duty cycles. Then, the PWM signals are created, and the same dead-time (DT) that in the real implementation is included.

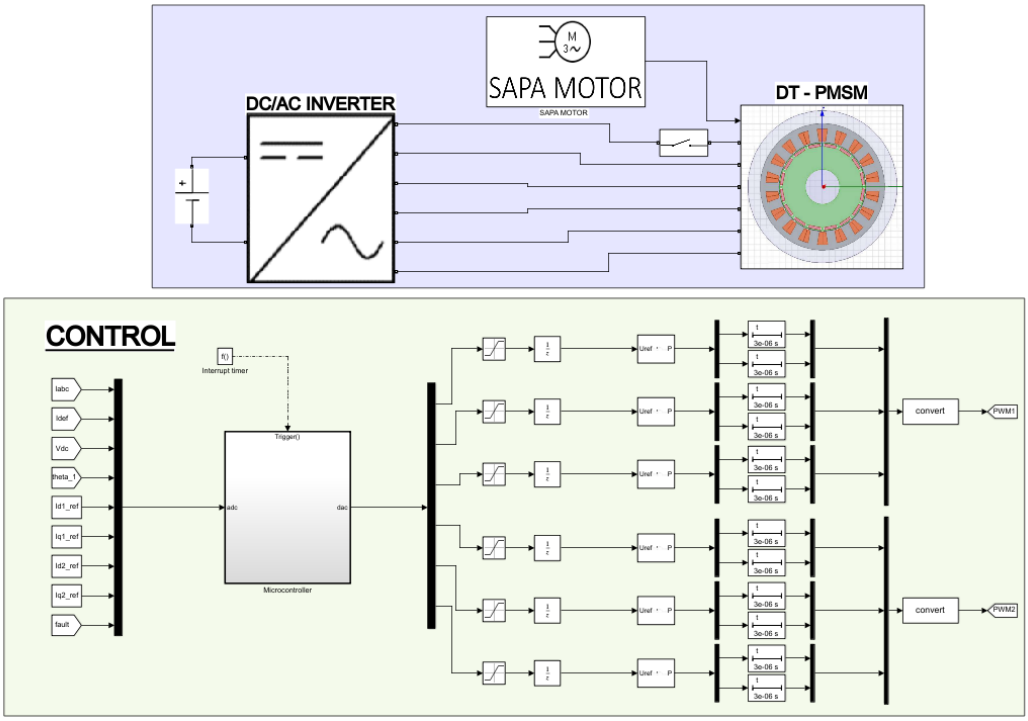

Figure 5-1: Simulink interface of the machine's control simulation

5.1 Simulation of FTC-WCSM

In this section, the simulation results of the fault-tolerant control strategy based on winding compensation through machine equations are included. The control tech-

nique is explained on section 3.7 and the schematic is shown in Fig. 3-15.

In this simulation, initially no fault will be included to test the current control in healthy situation. Then, an open-phase fault in phase A will be simulated to test the performance of the fault-tolerant control strategy. The initial conditions will be:

$$i_{d_1}^* = i_{d_2}^* = 0A$$

$$i_{q_1}^* = i_{q_2}^* = 4A$$

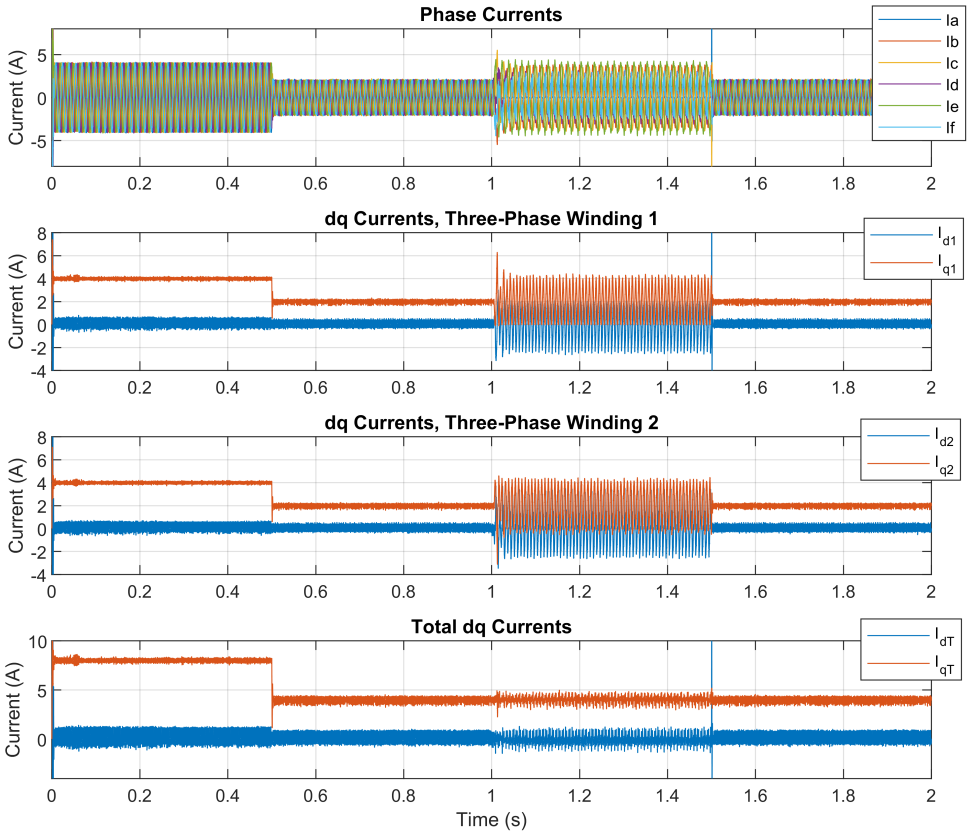

Figure 5-2: Simulation results when applying the FTC-WCSM under an open-phase fault

The rotating speed will be fixed in 200 rpm. Low speeds allow low current pulsations when disconnecting a phase, so that inverse-sequence PI controllers are not needed to track the current references in faulty operation. Then, in $t = 0.5s$ the $q-$axis current reference is varied from $4A$ to $2A$. After that, in $t = 1s$, phase A

is disconnected to simulate the open-phase fault. Finally, at $t = 1.5s$ the healthy operation is recovered.

Fig. 5-2 shows the obtained results in the simulation. First, the correct performance of the current control strategy during healthy operation is checked, as the current reference variations are correctly tracked. Then, when phase A is disconnected ($t = 1.5s$), the $d-$ and $q-$axis currents in the first three-phase winding begin to suffer oscillations at twice the rotating frequency. Then, the current references of the healthy three-phase winding are varied in order to compensate the error in the faulty one. Therefore, as seen in the bottom plot, the total $d-$ and $q-$axis currents are kept constant despite the open-circuit fault. This will lead to negligible torque pulsations despite the fault, which at the end is the main goal of a fault-tolerant control technique.

5.2 Simulation of FTC-VSD

Another fault-tolerant control method that was analysed in chapter 3 was the one based on vector space decomposition (FTC-VSD). The method is explained in section 3.3. In this case, the control strategy does not distinguish between two three-phase systems but it analyses the six phase windings as a single dq system. In order to analyse all possible faults, matrices T_{5s} and T_{5s}^{-1} are calculated for all possible faults as well as for the healthy operation. Now, the matrices are built for a phase shift between three-phase sets of 60º to be the same than the studied DT-IPMSM (see Fig. A-8). Depending on the machine state (healthy operation or open-phase operation), rotations from synchronous to stationary reference frame and vice versa are made with the corresponding matrices. In this way, the simulation will begin in healthy operation with $i_q^* = 15A$. Then, in $t = 0.25s$ phase A is open to test the fault-tolerant operation. After 0.1 seconds, the healthy operation will be recovered. From this point the fault-tolerant operation under open-circuit faults in the remaining phases is checked.

Fig. 5-3 shows the obtained results. It may be seen that when the fault occurs, the harmonic current component, I_{z1} is no longer null (compensate the error), but the $d-$ and $q-$axis components of current, responsible of creating torque are kept constant. However, as seen in $t = 0.75s$, in some situations the transition from one transformation matrix to another (going from one operation state to another) can be aggressive so that the $d-$ and $q-$axis currents can suffer a strong transient. In any case, the suitable operation is recovered relatively fast.

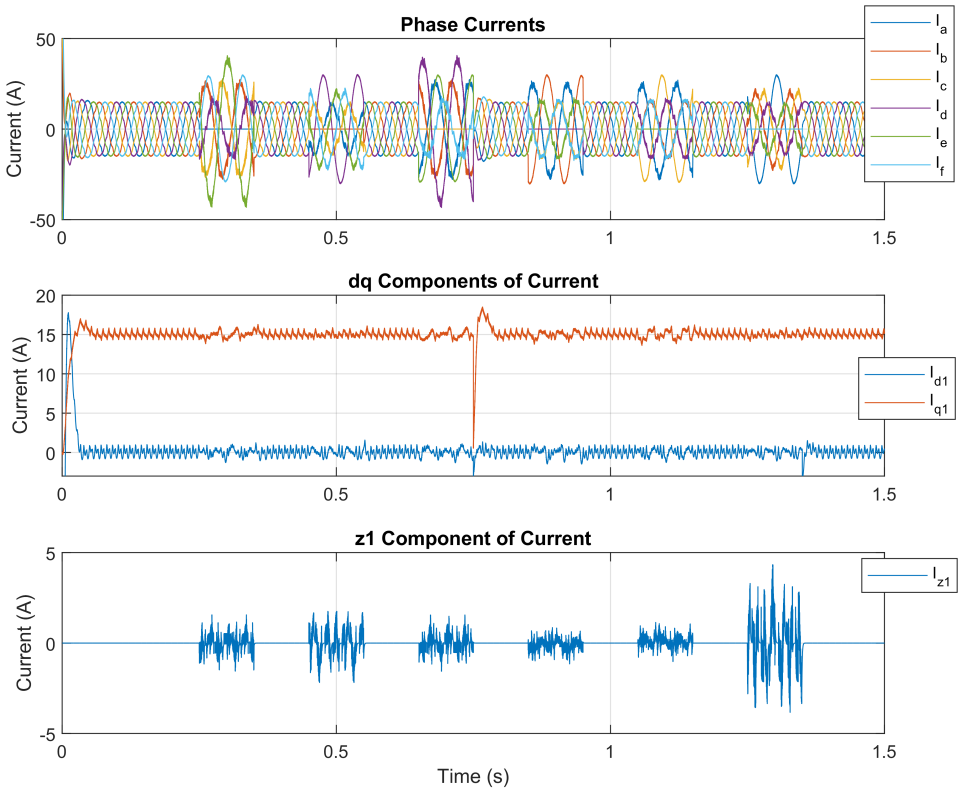

Figure 5-3: Simulation results when applying the FTC-VSD under an open-phase fault in each phase

5.3 Simulation of the PM temperature estimation method based on a $d-$axis high-frequency pulsating current signal injection

Before implementing it on the experimental test-bench, PM temperature estimation based on $d-$axis pulsating current signal injection is tested in Matlab/Simulink. The method is explained in section 4.2.1. Fig. 4-1 shows the block diagram of the control scheme for the proposed method. To bring the simulation as close as possible to reality, the control is implemented in C-code as well as will be done in the microcontroller. To simulate the temperature variation in the machine, the following steps are followed:

- The simulation will be run several times for different rotor temperatures.
- The stator temperature will be kept constant and equal to the room temperature (25°C).
- The value of the machine's resistance in the dynamic model of the machine (see (2.5) and (2.6)) is varied each time the simulation is run attending to the new rotor temperature following (4.10). In the same way, the PM flux linkage will be varied following (4.4). This is done to simulate the machine's heating.
- Then, following the process in Fig. 4-2, temperature can be estimated from the machine's measured voltages and currents.

Simulation is carried out commanding 5A for both $q-$axis currents and 0A for both fundamental $d-$axis currents. Then, a pulsating high-frequency current signal is commanded in the $d-axis$. The amplitude of the signal is 0.5A, while its frequency will consist of 500 Hz. Temperature variations for the different simulations are introduced following the heating curve of a PMSM seen in [78]. Fig. 5-4 shows the estimated and measured (values introduced in the simulation as inputs) values for the high-frequency resistance and rotor temperature.

It can be seen that the estimated machine's resistance always has an offset. Es-

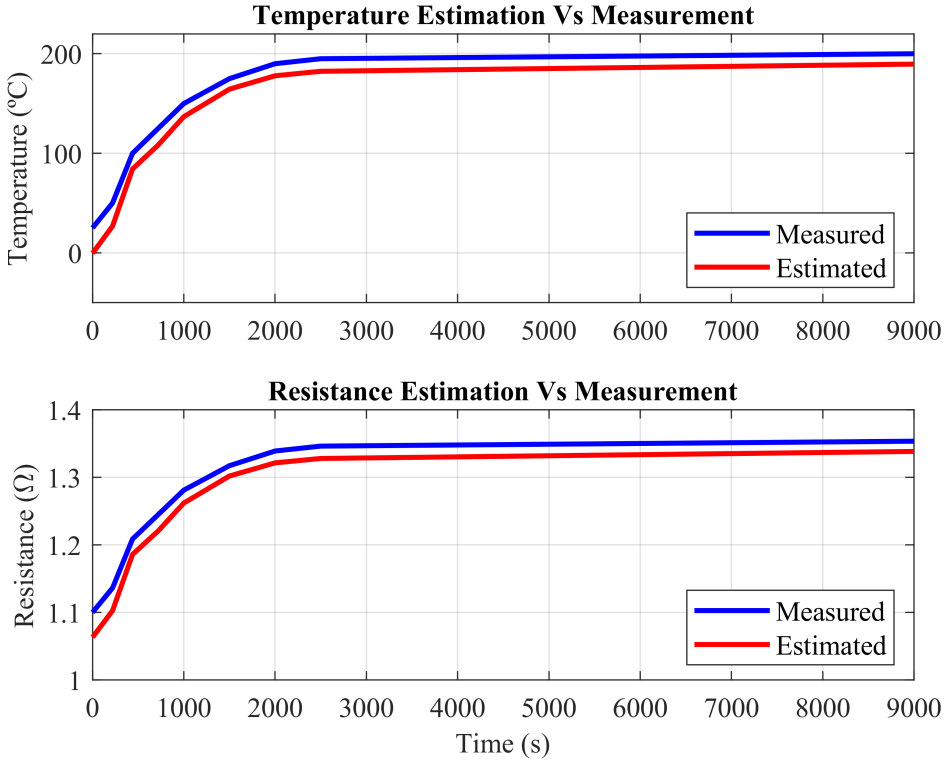

Figure 5-4: Measured and estimated machine's resistance and rotor temperature when applying the described method

timations below the real value are always obtained. Hence, when calculating the estimated rotor temperature, it can be seen that the error in the estimation of the resistance is also moved to the temperature estimation.

After analysing the simulation, it was found that this offset might come from the calculation of the $d-$axis current from the $d-$axis voltage following the electrical model in (2.5) . It can be seen that to calculate the current, an integration must be carried out. Mathematically, this integration introduces a delay in the calculated current respect to the $d-$axis voltage. Further research must be done to justify this assumption. In any case, this error is due to mathematical issues of the simulation that will not appear in the real implementation.

Chapter 6

Experimental Tests

This chapter is devoted to describe the experimental tests carried out during the development of this Master Thesis. First, the proposed FTC technique was assessed. Then, one of the explained temperature estimation methodologies was also tested.

6.1 Experimental testing of FTC-WCSM

In this section the experimental testing of the proposed fault-tolerant control strategy (see section 3.4) is analysed. The different elements that build the test-bench used for the mentioned experimental tests are mentioned and developed in depth in Appendix A. In order to make the disconnection of one of the phases to test the fault-tolerant capability of the control strategy, additional hardware is incorporated as explained in section A.4.5. The followed steps will be similar to the ones carried out in simulation (see section 5.1). Initially, the three-phase load machine will fix the rotating speed in 200 rpm. As well as in simulation, the test will be done at low speed to avoid the $dq-$axis current pulsations when disconnecting a phase to have a high-frequency. As in this initial tests no inverse-sequence PI controllers are used, high speeds would lead to high-frequency pulsations that could not be tracked by the direct-sequence PI current controllers. At the beginning, 0 $dq-$axis current is commanded. Then, the $q-$axis current reference of both three-phase windings is raised

to 2A, while the $d-$axis ones are kept in 0A. After that, phase A is disconnected. The machine continues working in faulty operation. Finally, phase A is reconnected and the healthy operation is recovered. Fig. 6-1 shows the effects in current of the mentioned variations in the machine's control. It can be seen that at the beginning,

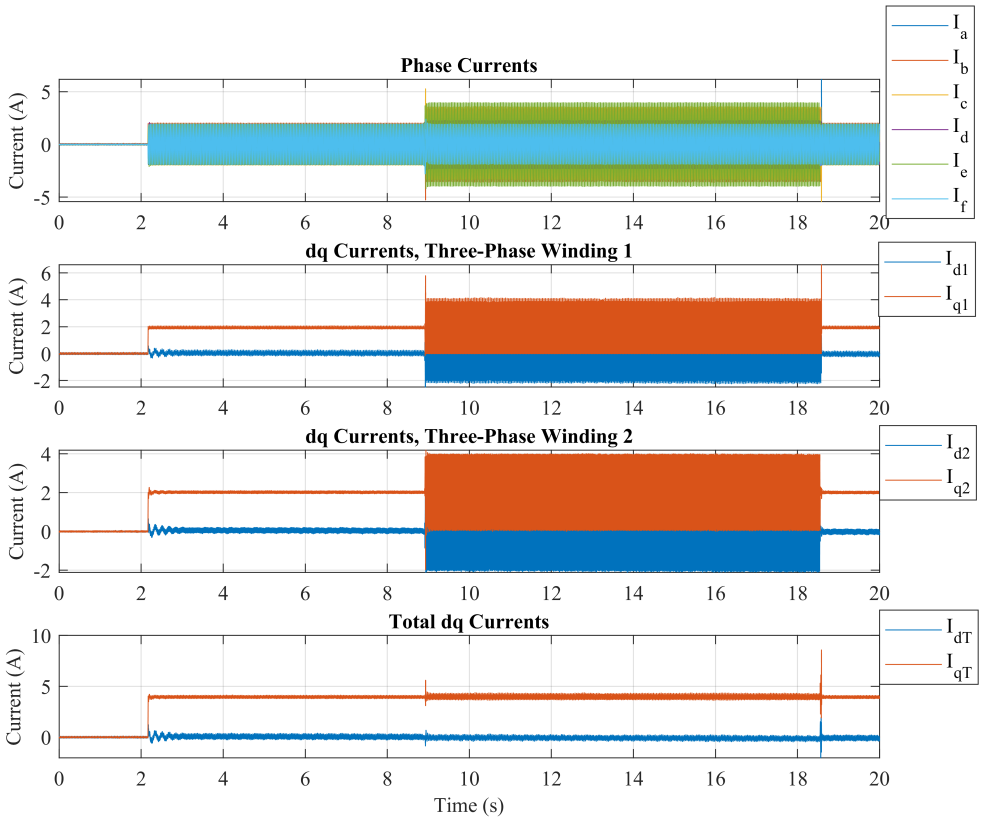

Figure 6-1: Phase, dq_1, dq_2 and total dq currents under variations in the machine operating conditions

the 2A $q-$axis current command is correctly followed. Then, when the phase disconnection occurs, the $d-$ and $q-$axis currents of the first three-phase winding start to suffer pulsations. In that moment, the fault-tolerant control strategy is activated so that the current references in the second three-phase winding are varied in order to have current pulsations counteracting the ones caused by the fault in the first three-phase winding. This will imply phase currents to have higher amplitudes that the initial ones. Finally, a constant total $dq-$axis current is obtained as seen in the bottom plot of Fig. 6-1. This will allow to avoid torque pulsations in the machine despite the fault. Fig. 6-2 shows the key transitions of Fig. 6-1 in an enlarged form.

From left to right, the enlarged transitions are: $q-$axis command variation from 0 to 2A, open-circuit fault, and return to the healthy operation.

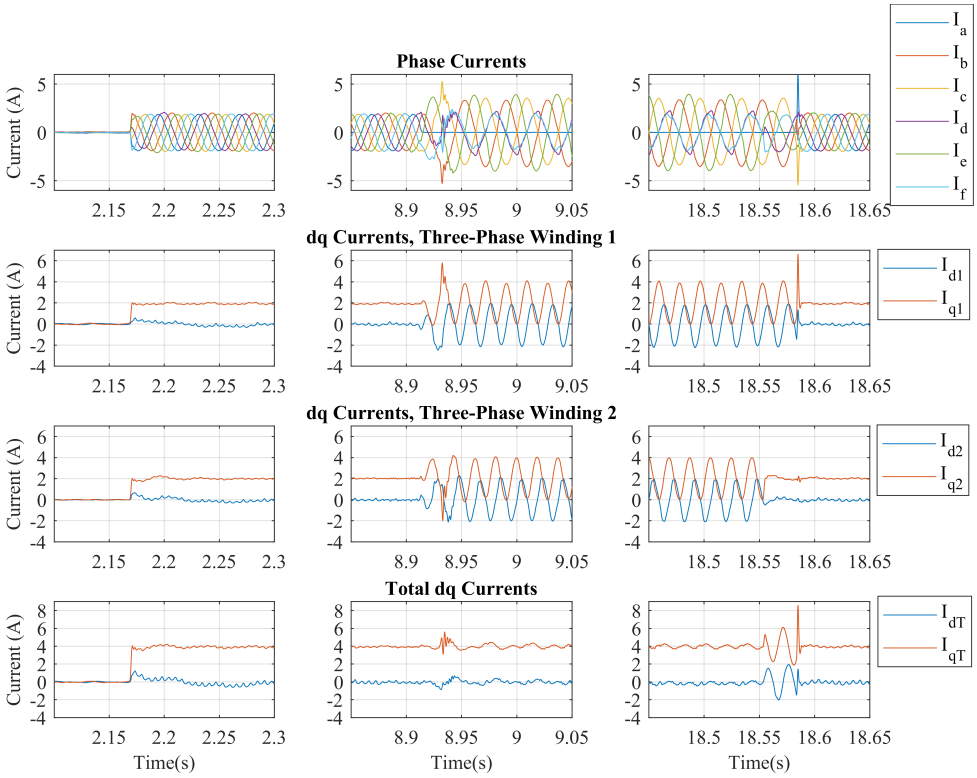

Figure 6-2: Enlarged transitions in the phase, dq_1, dq_2 and total dq currents under variations in the machine operating conditions

However, as seen in the bottom plot of Fig. 6-1 and Fig. 6-2, when the fault occurs, the total $q-$axis current remains practically constant but the ripple is slightly increased. This can be due to the fact that a PI controller is used to track an ac current, so that reference tracking might not be good enough. This is analysed in Fig. 6-3. It can be seen that initially the current references of both three-phase systems are equal. When the fault occurs, the first dq system can not continue tracking the reference. Then, the current reference in the second dq system is varied to counteract the error in the first one. In principle, this references are correctly followed. However, it can be seen that there is a small error in the peaks of the sine waves. This error leads to the increase in the $dq-$axis current ripple when the fault occurs. As aforementioned, this error might be attenuated by adding an inverse

sequence PI controller when going into fault operation in parallel with the direct sequence one. A proportional-resonant (PR) controller could be another option. PR controllers must be tuned for tracking an ac current with certain frequency. However, the frequency of the current pulsations when disconnecting a phase vary depending on the rotor speed, which make the implementation not practical. This will be framed as a future work.

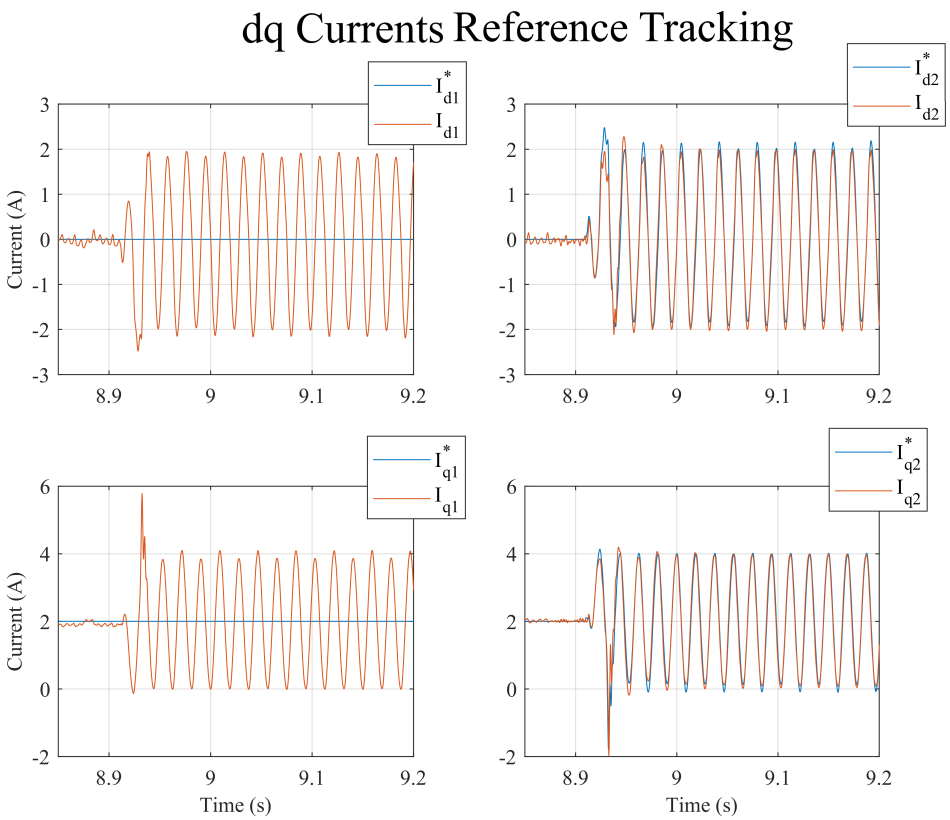

Figure 6-3: Analysis of the PI controllers reference tracking during faulty operation

6.2 Experimental testing of the PM temperature estimation method based on d-axis pulsating current signal injection

After testing the performance of the proposed FT control technique in the experimental test-bench, the other objective of this Master Thesis consists of applying one of the described PM temperature estimation methods. PM temperature estimation will be tested by injecting a pulsating HF signal in the d-axis (see section 4.2.1). Fig. 4-1 shows the block diagram of the applied control method. A proportional resonant (PR) controller is used for controlling the injected high-frequency current signal. In addition, Fig. 4-2 shows how the obtained signals must be processed in order to obtain suitable results. In (4.30), it can be seen how the method requires previous information of both the stator and rotor resistances at room temperature. The estimation of the mentioned parameters is developed in A.4.4. Added to the resistances values, information about the stator temperature is required. Hence, eight thermocouples are connected in different points of the stator. Table 6.1 shows the corresponding coil (see Fig. A-7) in which each thermocouple is connected. T_{cj} stands for the cold junction measured temperature, which is the room temperature, T_0. It can be seen that more than one thermocouple is located in a single coil.

Table 6.1: Stator Thermocouples

T_{cj}	T_{s1}	T_{s2}	T_{s3}	T_{s4}	T_{s5}	T_{s6}	T_{s7}	T_{s8}
T_0	11(a)	11(b)	17(a)	2(a)	17(b)	2(b)	2(c)	17(c)

Moreover, in order to measure the rotor temperature while the test is being carried out, a thermocouple is connected to one of the permanent magnets. This thermocouple will be rotating with the rotor. Hence, measurements can not be read in a computer through wires. In this way, thermocouples are connected to a PCB in which the measurements are sent to a computer via Wi-Fi. Fig. 6-4(a) shows the support coupled to the motor shaft in order to locate the PCB. In Fig. 6-4(b) it can be seen

the mentioned PCB. Finally, Fig. 6-4(c) shows the PCB coupled to the rotor shaft through the support.

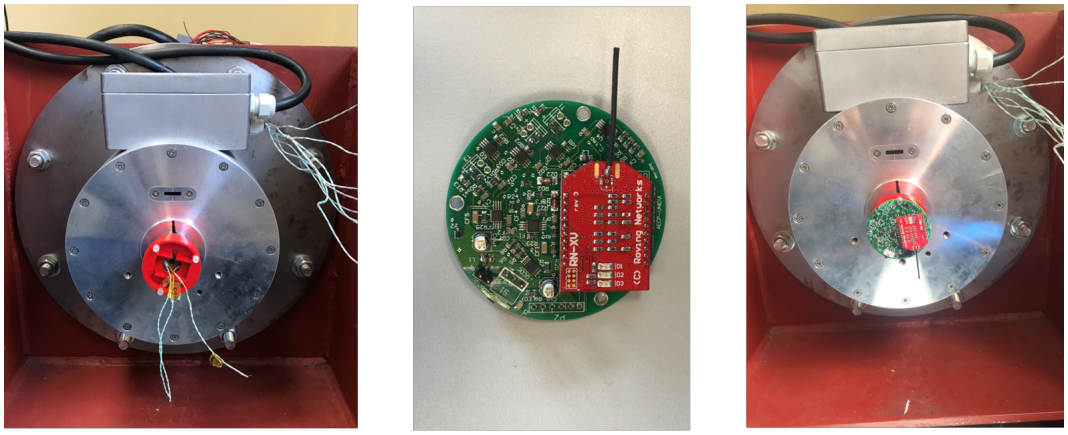

(a) (b) (c)

Figure 6-4: Placement of the PCB that sends the rotor temperature measurements to the computer via Wi-Fi

Once the experimental set-up is fully prepared, the experimental test is carried out. Both $q-$axis current references will be fixed in 5A, while the fundamental $d-$axis ones will be 0A. In addition a $d-$axis high-frequency signal will be injected in both three-phase sets. The amplitude of this signal will be 0.5A while its frequency will consist of 500 Hz. This frequency is selected to have a large spectral distance between the fundamental and the HF components. The rotating speed of the rotor will be fixed in 200 rpm. As Fig. 6-5 shows, the duration of the test was close to six hours so that the stator reached almost 70ºC in certain points while the PM ended up at 60ºC. During the test, the battery that feeds the Wi-Fi PCB was discharged and had to be replaced. At that time the machine got cold as seen between hours 3 and 4 in Fig. 6-5.

Throughout the test, phase current and phase to phase voltage measurements were taken at the following rotor temperatures: 23º (room temperature), 40ºC and 50º before cooling. After that, measurements were taken at 45ºC, 50ºC, 55ºC and 60ºC. Then, the signal processing seen in Fig. 4-2 is followed to obtain the high-frequency resistance. Figs. 6-6 (a1), (b1) and (c1) show the estimated high-frequency $d-$axis

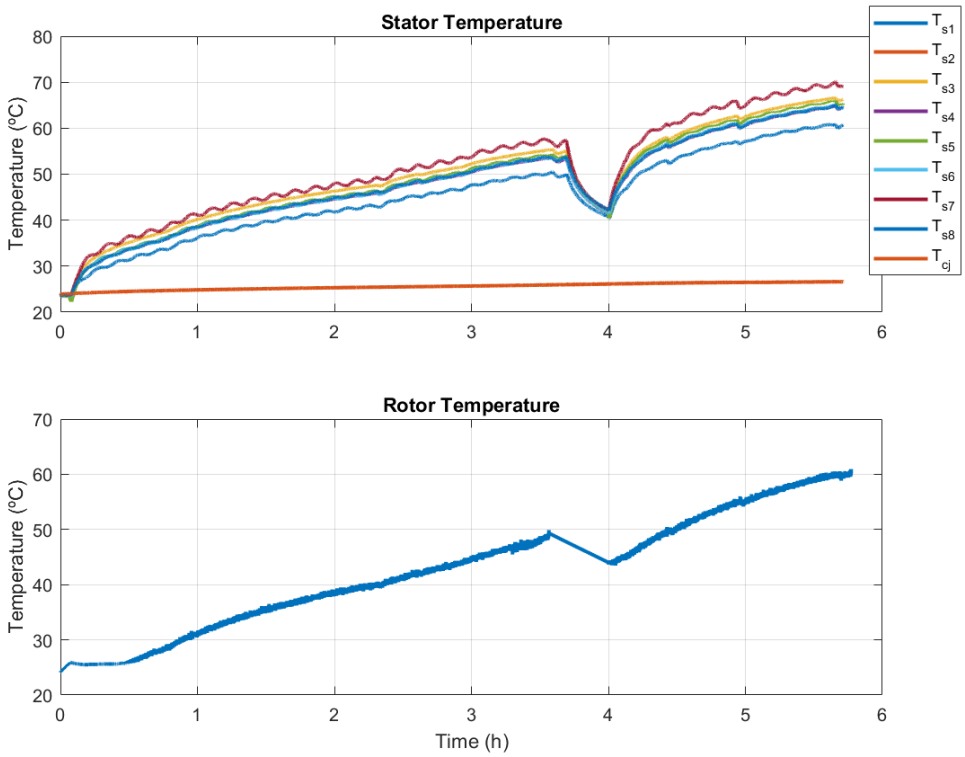

Figure 6-5: Evolution of the stator and rotor temperature during the PM temperature estimation test

resistance, inductance as well as the impedance angle before cooling respectively, depending on the rotor temperature. Figs. 6-6 (a2), (b2) and (c2) show the estimated high-frequency $d-$axis resistance, inductance as well as the impedance angle after cooling respectively, depending on the rotor temperature.

It can be seen how despite the rotor temperature increases, the variation of the high-frequency resistance is not proportional to the temperature variation as was expected. Moreover, the variations are larger than expected. Hence, bad temperature estimation results will be obtained. However, the obtained poor results can be explained, as several important aspects have not being covered during the experimental testing. Following, the aforementioned facets that have not been considered, and have a crucial effect in the PM temperature estimation process are summarized.

First, in Fig. 6-6(c1) and (c2) it can be seen how the angle of the estimated impedance is always close to 90º during the test. This means that the resistive

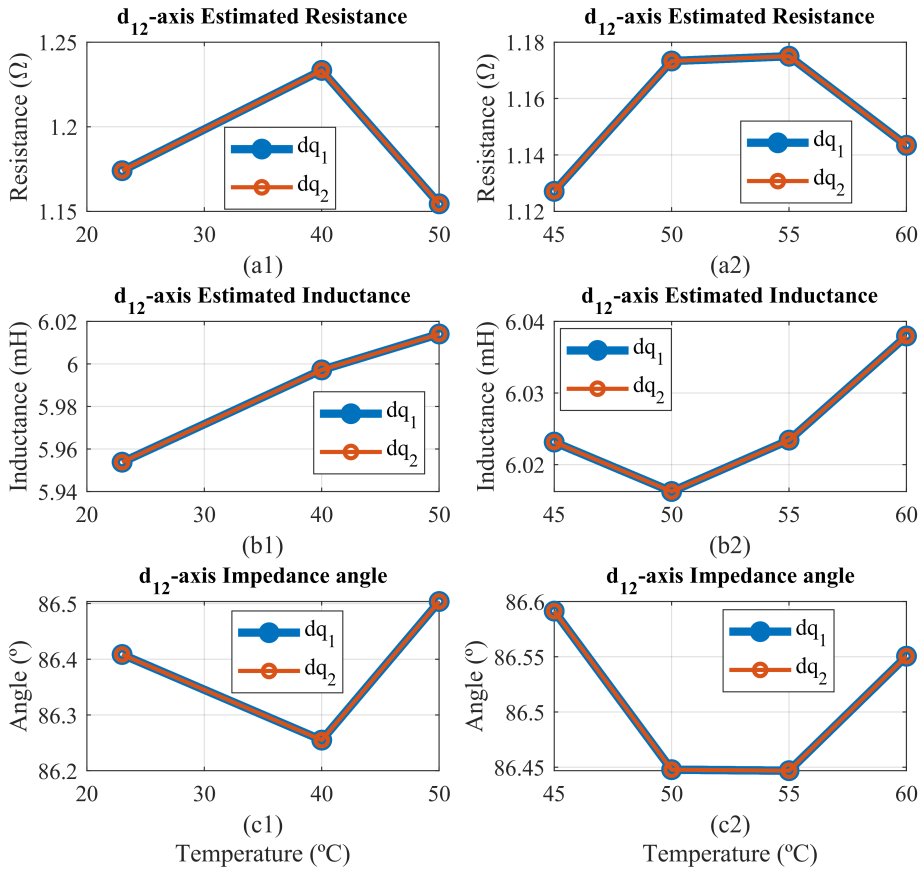

Figure 6-6: Estimated HF resistance (a1-a2), inductance (b1-b2) and impedance angle (c1-c2) after and before cooling

component is very low compared to the inductive reactance. The machine has become very inductive. Then, any small error during measurement (e.g. electromagnetic noise) will have a huge effect in the estimated resistance but a low one in the reactance. This explains why the estimated resistance varies so much from a measurement to another when the temperature variation is low. This error can be mitigated by reducing the frequency of the injected HF signal. As lower the frequency of the injected signal, as higher the weight of the resistance in the machine's impedance, and lower the one of the reactance.

Another aspect to take into account is related with the stator measured temperature. In Fig. 6-5 it can be seen how the stator temperature varies a lot depending on the point on which the thermocouple is placed. For instance, when heating the

machine the temperature of a coil will not be homogeneous for the whole coil. Then, when estimating the temperature the introduced stator temperature in (4.30) will lead to errors. Hence, it is advisable to take the measurements during machine's cooling. As seen in Fig. 6-5, during cooling, the different measured points have a more homogeneous temperature value than when heating the machine.

Finally, it is possible that during the test the estimated HF resistance was not considering the rotor one. Current flowing through the machine windings create a variable magnetic field. The interaction of these magnetic fields with the rotor promotes the flow of Eddy currents [79,80] through the rotor lamination. In addition, due to the injection of a high-frequency current, skin effect will promote Eddy currents to circulate through the surface of the rotor. Then, following Faradays's cage theory, Eddy currents will generate a magnetic field that will oppose the stator one. This will promote the creation of a *'shield'*. This *'shield'* will block the interaction of the stator and rotor magnetic field. This effect is positive when the machine is working at low frequencies since the shield will not block the interaction of the fundamental components of the stator and rotor fields, but it will block the interaction of high-frequency harmonics. This is one of the advantages of IPMSMs respect to SPMSMs. However, as higher the injected frequency, Eddy currents will flow closer to the surface of the rotor and thus, the interaction of rotor and stator fields will be more limited. Fig. 6-7 represents this effect.

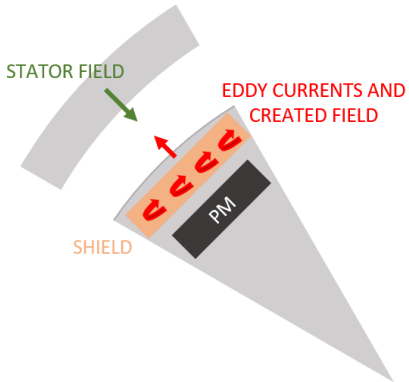

Figure 6-7: PMSM cross section, highlighting the effect of Eddy currents

Summarizing, there are several aspects that have not being covered during the development of this experimental test. Some of these facets have been just described. That's where poor results come in. Results for both $dq-$systems are pretty much the same. Further research is required to optimize the realization of the tests so that better results can be obtained.

Chapter 7

Conclusions and Future Work

7.1 Conclusions

The present Master Thesis focuses on the study of fault-tolerant control (FTC) strategies for multi-phase PMSMs as well as PM temperature estimation methods. Chapter 2 introduces the dynamic model of a multi-phase PMSM:

- An in-depth analysis of multi-phase machines has been done. Non-three-phase series type (five-phase, seven-phase, eleven-phase, etc.) and three-phase series type can be distinguished. These last ones can be divided in non-multi three-phase (six-phase, nine-phase, etc.) and multi-three-phase machines (dual three-phase, triple three-phase, etc.). Multi-three-phase machines are advantageous as conventional three-phase machine's theory can be applied.
- The dynamic model of a multi-phase machine has been developed to be simulated in Simulink. This allows to integrate the machine's control in the simulation. From the phase to phase voltage measurements, the phase currents are obtained by applying the electrical model of the machine. Then, current sources are used to set the value of the phase currents in the previously calculated one.

Chapter 3 describes some of the FTC methods present in literature. In addition, a novel fault-tolerant control technique is proposed.

- After analysing the most significant FTC techniques in literature, it is found that: Methods based on the instantaneous power balance theory require to use hysteresis controllers to track current references. Online implementation is limited to SPMSMs. Strategies based on vector spaced decomposition-based space vector modulation (VSD-based SVM) require offline implementation of transformation matrices. Compensating a fault in a three-phase winding with a healthy one allows online implementation while controlling currents in the synchronous reference frame. Finally, neutral connection to the DC-link provides more possibilities in terms of FT controlability, while increasing the complexity of the control.

- This Master Thesis proposes a fault-tolerant control technique for multi-phase machines with isolated neutral points. This method is based on compensating the current harmonics in the faulty three-phase winding by modifying the control strategy in the healthy sets. In this case, the current reference variation is carried out based on the current measurements. Constant torque and equal to the pre-fault one during fault operation is achieved. Precise current sensors are required. Implementation of negative-sequence PI controllers is advisable in order to track ac current references. The technique is limited to multi-three machines, and a perfectly healthy winding is required.

Chapter 4 focuses on the study of PM temperature estimation methods. After introducing PM temperature estimation techniques using thermal models, and methods based on the BEMF, two PM temperature estimation methods based on high-frequency signal injection are mainly analysed:

- The first technique is based on the injection of a pulsating $d-$axis high-frequency current signal. This method provides a lumped estimation of the PM temperature, i.e. it provides an averaged PM temperature. The limitations of rotating high-frequency voltage injection methods, such as the sensitivity to the machine speed and to L_q and L_d changes are overcome.

- The second technique is intended for PM temperature distribution estimation,

which is obtained from the mean and differential PM temperature. Differential magnet temperature estimation is based on the modification of the harmonic content of the BEMF, due to the changes produced in PM flux linkage between the rotor and the stator, by a non-uniform temperature profile in the magnet. As any parameter estimation method based on BEMF, it cannot operate at low/zero speed. Mean PM temperature can be estimated using either the fundamental component of the BEMF or injecting a pulsating $d-$axis high-frequency current signal and measuring the $d-$axis high-frequency resistance.

Chapter 5 is dedicated to test in simulation (Matlab/Simulink) some of the described control strategies as well as PM temperature estimation methods:

- First, the proposed fault-tolerant control technique is tested in Simulink after creating the model of the studied DT-IPMSM. Control is implemented with C-code as well as done in the real implementation. The test is carried out at low speed as well as reduced current levels to avoid the need of using dual PI controllers in order to track ac current references when an open-circuit fault occurs. Results show that in the moment that a phase is open, the current references in the healthy three-phase set are varied in a way that the total $d-$ and $q-$axis currents are kept constant despite the fault. It is found that the method has an acceptable performance. However, implementation of inverse-sequence PI controllers will be necessary to improve the current reference tracking when increasing current and rotating speed.
- Fault-tolerant control based on VSD is also tested in simulation. A single open-phase fault is assessed for each phase. It is found that, when a fault occurs, the harmonic component $z1$ is not zero any more, but the $d-$ and $q-$axis currents are kept constant so that torque pulsations are removed despite the fault. Good performance is obtained. However, the performance of the method does not improve the one of the proposed technique while the implementation complexity raises.
- When simulating the PM temperature estimation method based on the injection

of a $d-$axis HF signal, it is found that the estimation presents always an offset respect to the real temperature value. This offset might be produced due to the delay promoted by the integration during current calculation. Further research is required to solve this issue. In any case, this is a mathematical problem that will not affect the real implementation of the method.

Chapter 6 explains the experimental tests that were carried out in the test-bench to assess the proposed FT control strategy as well as one PM temperature estimation method:

- The proposed fault-tolerant control strategy was tested in the experimental test-bench. In order to carry out the disconnection of one of the phases to emulate the open-phase fault, a contactor driven by a programmable relay is incorporated. As well as in simulation, the test was carried out at low-speed and with low currents in order to avoid the need of using negative-sequence PI controllers. Similar results to the simulation ones are obtained. Current compensation is carried out successfully. Implementation of inverse-sequence PI controllers is required to keep the performance of the method with larger current and speed levels.
- When carrying out the simulated PM temperature estimation method in the test-bench, poor results are obtained. Estimated high-frequency resistances do not follow the temperature tendency. Large value of the inductive component of the high-frequency impedance compared to the resistive one, non-homogeneous stator temperatures, and creation of Eddy currents in the rotor lamination are some of the reasons why the method did not work. It is analysed that the reduction of the injected signal's frequency, as well as voltage and current measurement during machine's cooling instead of heating might improve the performance of the method.

7.2 Future Work

Added to the research work covered in this document, more aspects can be included in future following the research line of this Master Thesis.

- As already mentioned throughout the document, negative-sequence PI controllers must be added to the control scheme of the proposed FT control technique to improve the performance of the method.
- The implementation in the test-bench of different fault-tolerant control strategies will allow to compare their performances for the same machine, so that better conclusions can be achieved.
- Apply all the aspects that have not being considered during the experimental tests related with the PM temperature estimation, so that better results can be reached.
- Study the possibilities offered by the fact of having two dq systems in the DT-IPMSM regarding the injection of high-frequency signals for estimating temperature or even torque.
- Development of permanent magnet temperature estimation techniques under faulty working conditions.
- Integration of the machine thermal estimation in the machine control strategy to improve the robustness and fault tolerance of the drive.
- Added to temperature, implement PM magnetization state (MS) estimation techniques.

Appendix A

Development of the test-bench

Chapter 6 presented the experimental tests that were carried out during the development of this Master Thesis as well as the obtained results. This appendix will be devoted to describe the different steps that were done before achieving the desired performance of the test-bench. Fig. A-1 shows the main elements that build the test-bench, which are:

- The dual three-phase interior permanent magnet synchronous machine (DT-IPMSM).
- A three-phase IPMSM shaft-connected to the DT-IPMSM to fix the rotating speed.
- A three-phase inverter for driving the three-phase IPMSM.
- Two three-phase inverters (six-phase inverter) for driving the DT-IPMSM.
- A three-phase rectifier that feeds the DC-link of the inverters.
- A three-phase transformer used for raising the grid voltage that feeds the three-phase rectifier.
- Two computers that control the three-phase IPMSM's inverter and the DT-IPMSM's ones respectively.

Each inverter is driven by two PCBs (Printed Circuit Boards): the control PCB,

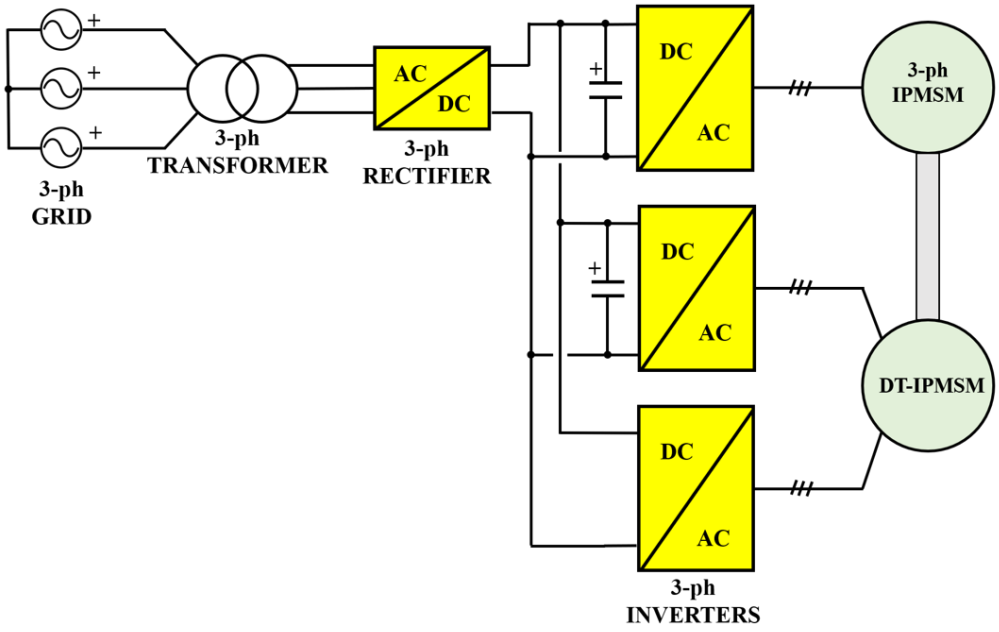

Figure A-1: Scheme of the test-bench main elements

and the power PCB. In section A.1 the functioning of the different PCBs is analysed.

A.1 PCB Analysis

A.1.1 Control PCB

The control PCB is in charge of reading the analog measurements, in order to allow the digital signal processor (DSP) to make the analog to digital conversion. Then, the microcontroller applies the designed control strategy to finally send the gate signals to the power PCB. The utilized DSP is the TMS320F28335 (Texas Instruments), while Code Composer Studio v9 (CCS) is the software used for reading the ADC measurements and generate adequate PWM signals through the designed control strategy. There are two control PCBs, one for the three-phase inverter that runs the three-phase IPMSM and another for running the six-phase inverter (two three-phase ones) that drives the DT-IPMSM. Most important elements of the mentioned PCB are highlighted in Fig. A-2.

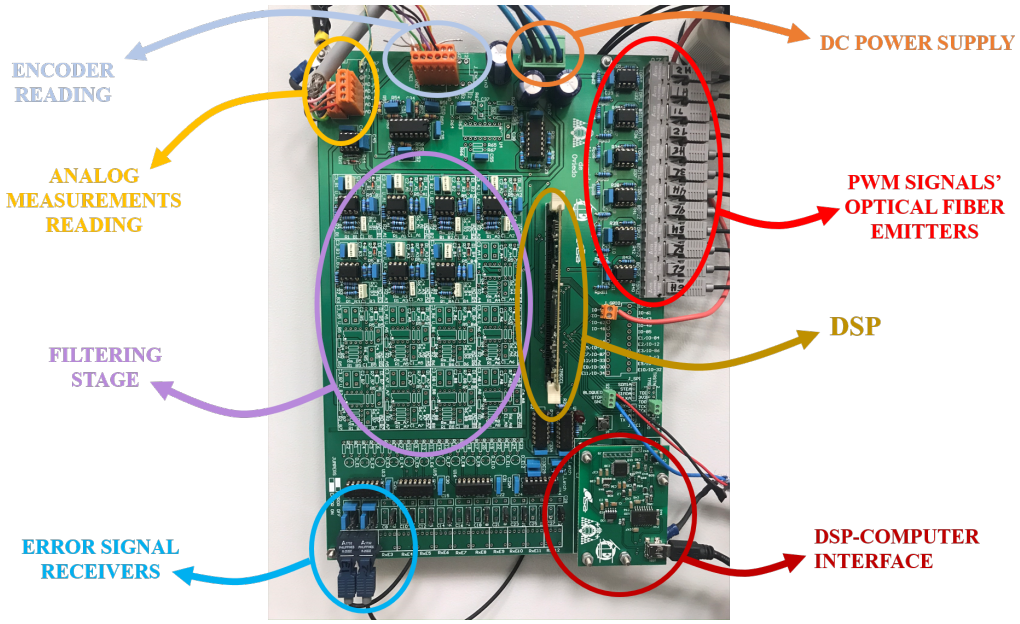

Figure A-2: Control PCB main parts

A.1.1.1 Filtering Stage

The filtering stage of the control PCB is basically an adaptation stage that allows to move the analog sensed measurements to the ranges allowed by the DSP. Hence, as seen in Fig. A-2 seven filtering stages can be distinguished (six for each phase current measurement, and another for the DC-link voltage measurement). The first part of each filter uses a measurement resistance for adapting the current provided by the sensors to the corresponding voltage that will be read by the microcontroller ADC [0-3V]. The second part is a second order multiple feedback Bessel filter of 3.5 kHz, gain 1 and phase-shift of 180º that acts as anti-aliasing filter. The circuit was sized following [81] and at the output it has a zener-diode in order to protect the microcontroller if the filter fails.

A.1.1.2 PWM optical fiber emitters

Communications through optical fiber allow to reduce noise compared with usual wires. Hence, the PWM signals generated by the DSP are sent to the power PCB through optical fiber. Optical fiber emitters are used to convert an electrical signal into a corresponding light signal that can be injected into the fiber.

A.1.1.3 Error signal optical fiber receivers

As well as the PWM signals, the error signals provided by the IGBT module are also transmitted to the control PCB through optical fiber. Optical fiber receivers are used to perform the actual reception of the optical signal and convert it into electrical pulses.

A.1.1.4 Encoder Reading

This part of the control PCB is used to read the different signals that the incremental encoder provides (see section A.4.1).

A.1.2 Power PCB

The main goal of the power PCB is to read the PWM signals sent by the control PCB, and adapt their voltages values to the ones required by the inverter IGBTs. In addition, the power PCB incorporates a DC-link voltage sensor, whose measurement is sent to the control PCB. Each three-phase inverter has a power PCB that drives the IGBTs voltages. Fig. A-3 shows the most important parts of the power PCB.

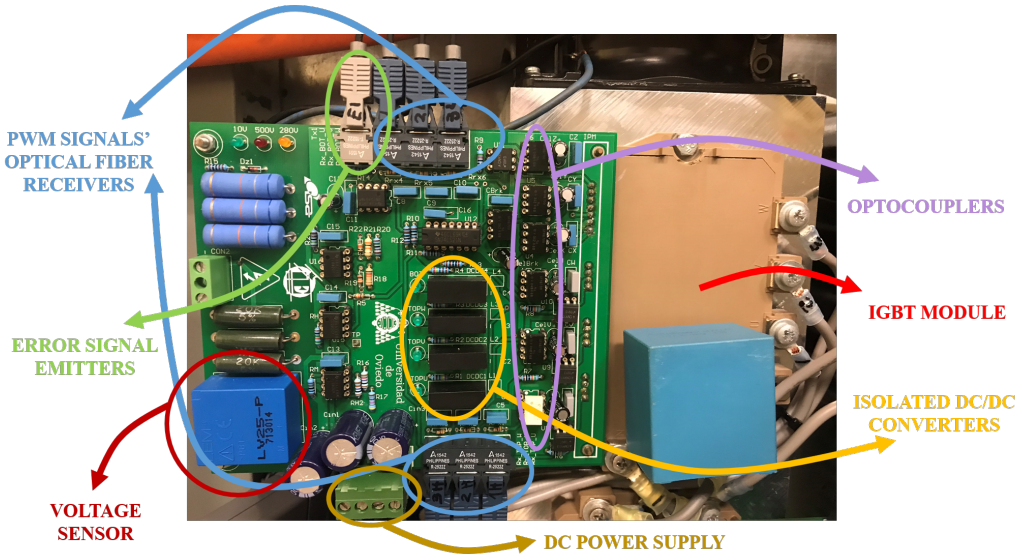

Figure A-3: Power PCB main parts

A.1.2.1 PWM signal optical fiber receivers

In the power PCB, optical fiber receivers are used to get the signals provided by the DSP in the control PCB through optical fiber.

A.1.2.2 Error signal optical fiber emitter

When the IGBT module generates an error signal, this one will be sent to the control PCB through optical fiber in order to allow the DSP to read this error.

A.1.2.3 Driver

The driver is in charge of sending suitable PWM signals to the IGBT's gates. Once the PWM signal is received, it is sent to optocouplers. Optocouplers are electronic components that interconnect two separate electrical circuits by means of a light sensitive optical interface. In this way, electrical isolation is provided. Finally, the optocoupler outputs are sent to each IGBT gate. Isolated DC/DC converters are used for feeding the electronic devices of the power PCB.

A.1.2.4 Voltage Sensor

The voltage sensor is in charge of reading the DC link voltage. Voltage is measured in an suitable-designed measurement resistance available in a test-point of the power PCB. This test-point is connected to the voltage measurement's filter in the control PCB through a wire.

A.2 Converter tests

In this section the initial tests and control strategies that were developed to check the correct performance of the converter are defined. First, the implemented control strategies were tested with a RL load. Once the control techniques were checked to have a correct performance, the DT-IPMSM substituted the load.

A.2.1 Converter test with a RL load

In a first approach, in order to avoid damaging the DT-IPMSM when the inverter control was initially tested, a RL load was connected to the six-phase inverter. Two three-phase RL loads are connected to both three-phase inverters building two star connections. The load values are $R = 56\ \Omega$ and $L = 1.283$ mH. The DC-link of the inverter is fed by a 30V DC voltage source. Two control techniques are applied to the inverter: Volts/Hertz control (V/Hz) and current control.

A.2.1.1 Volts/Hertz Control (V/Hz)

Volts/Hertz control is an open loop control, so that it allows sensorless regulation. However, as there is no feedback loop, the system loses dynamic performance. The input of the control is the electric frequency, which is obtained according to the wanted synchronous speed:

$$f_s = \frac{\omega_{rm} \cdot P}{60} \tag{A.1}$$

being ω_{rm} the rotor synchronous speed, P the machine number of pole pairs, and f_s the electric frequency. The voltage is set in order to keep the stator flux constant. The RMS value of the induced voltage in AC motors is given by:

$$E_f = \sqrt{2} f_s N_s k_w \phi \tag{A.2}$$

Where E_f is the RMS value of the induced voltage, N_s is the stator coil turns of wire, ϕ the flux passing through a coil, and k_w is a geometry constant. If the voltage drop caused by the resistance of the stator is neglected and steady conditions are assumed, the magnetic flux can be written as:

$$\phi = \frac{V_{sph}}{\sqrt{2} f_s N_s k_w} = c \frac{V_{sph}}{f_s} \tag{A.3}$$

As a consequence, in order to maintain the stator flux constant at its rated value the voltage-to-frequency ratio should be kept constant. If the stator flux is over its rated value the motor will be overexcited [82, 83]. Fig. A-4 shows the block diagram of the V/Hz control strategy. When the reference voltage (V_n^*) is got, it is used to calculate the duty cycles of the PWM signals used in inverter:

$$d_n = 0.5 + V_n^*/V_{dc} \tag{A.4}$$

Being V_{DC} the voltage on the DC bus.

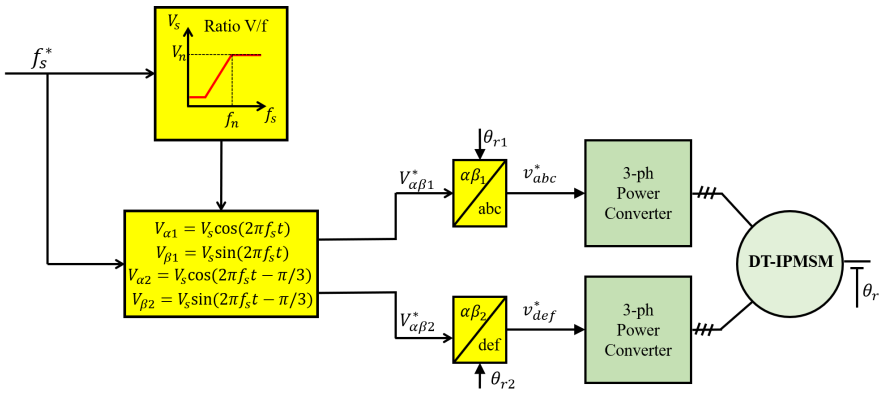

Figure A-4: Schematic of the V/Hz open-loop control strategy

However, during the experimental tests, the explained technique was slightly modified. First, $d-$ and $q-$axis voltage references are commanded, added to a frequency command. Once this is done, in order to reach V_n^* and apply (A.4) the voltage references V_d^* and V_q^* are rotated using the Park transformation with the angle obtained from f_{ref} (θ_{ref}).

$$\begin{bmatrix} V_{\alpha_1} \\ V_{\beta_1} \\ V_{0_1} \end{bmatrix} = \begin{bmatrix} cos(\theta_{ref}) & -sin(\theta_{ref}) & 0 \\ sin(\theta_{ref}) & cos(\theta_{ref}) & 0 \\ 0 & 0 & 1 \end{bmatrix} \cdot \begin{bmatrix} V_{d_1} \\ V_{q_1} \\ V_{0_1} \end{bmatrix} \tag{A.5}$$

$$\begin{bmatrix} V_a \\ V_b \\ V_c \end{bmatrix} = \begin{bmatrix} 1 & 0 & 1 \\ -\frac{1}{2} & \frac{\sqrt{3}}{2} & 1 \\ -\frac{1}{2} & -\frac{\sqrt{3}}{2} & 1 \end{bmatrix} \cdot \begin{bmatrix} V_{\alpha_1} \\ V_{\beta_1} \\ V_{0_1} \end{bmatrix} \tag{A.6}$$

$$\begin{bmatrix} V_{\alpha_2} \\ V_{\beta_2} \\ V_{0_2} \end{bmatrix} = \begin{bmatrix} cos(\theta_{ref} - \frac{\pi}{3}) & -sin(\theta_{ref} - \frac{\pi}{3}) & 0 \\ sin(\theta_{ref} - \frac{\pi}{3}) & cos(\theta_{ref} - \frac{\pi}{3}) & 0 \\ 0 & 0 & 1 \end{bmatrix} \cdot \begin{bmatrix} V_{d_2} \\ V_{q_2} \\ V_{0_2} \end{bmatrix} \tag{A.7}$$

$$\begin{bmatrix} V_d \\ V_e \\ V_f \end{bmatrix} = \begin{bmatrix} 1 & 0 & 1 \\ -\frac{1}{2} & \frac{\sqrt{3}}{2} & 1 \\ -\frac{1}{2} & -\frac{\sqrt{3}}{2} & 1 \end{bmatrix} \cdot \begin{bmatrix} V_{\alpha_2} \\ V_{\beta_2} \\ V_{0_2} \end{bmatrix} \tag{A.8}$$

A.2.1.2 Current control

Once the converter operation with an open-loop control is tested, the next step will be moving to a closed loop one. It will consist of controlling the synchronous reference frame currents of each three-phase RL load. Fig. A-5 shows the schematic of the defined closed-loop control. The *dq*-axis currents are controlled with proportional-integral (PI) controllers as they allow to reach zero steady-state error. The control action of the described controllers will be the synchronous reference frame voltage references $v^*_{dqs_{12}}$. Carrying out a *dq*-to-*abc* rotation, the phase voltage references are

computed. Eventually, applying (A.9) the duty cycles corresponding to the PWM signals in charge of driving the inverter IGBT's are obtained.

$$d_i = 0.5 + \frac{V_i^*}{V_{dc}} \tag{A.9}$$

being $i = A, B, C, D, E, F$ the indicator of each phase.

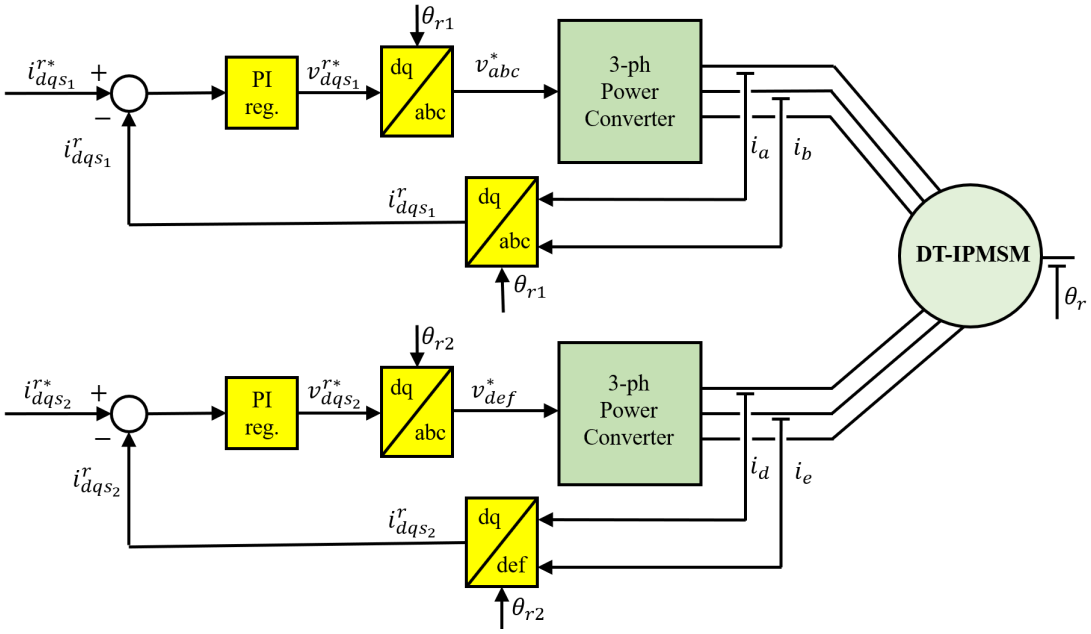

Figure A-5: Schematic of the current control strategy

It must be mentioned that up to this point no encoder has been used, so that rotations are made with a test phase created in the microcontroller code.

A.2.2 Converter test with the DT-IPMSM

After checking the correct performance of the converter with the implemented control strategies when having a load connected, it is safe to replace the load with the electric machine. The DC-link of the inverters is then feed by the grid through the step-up transformer. As well as before, the inverter feeding the machine was initially tested in open-loop. Volts/Hertz control led to some problems when the machine was connected: since current is not being controlled, when voltage and speed (frequency) commands variations are required, the machine suffers some type of vibrations and

had difficulties to recover a fluid rotation. In this way, current control was directly implemented following the scheme in Fig. A-5.

A.3 Studied Dual Three-Phase IPMSM (DT-IPMSM)

The use of a dual three-phase interior permanent magnet synchronous machine (DT-IPMSM) is mentioned throughout this Master Thesis. However, up to this point, the characteristics of the machine with which all the tests included in this document have been carried out have not being studied in depth. Fig. A-6 presents the cross-section of the analysed machine.

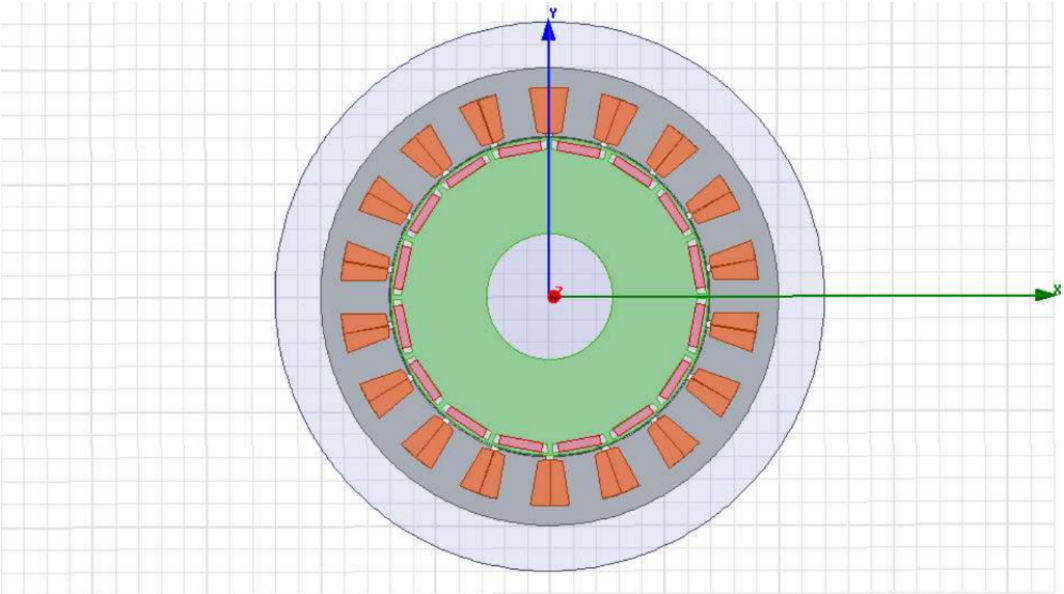

Figure A-6: Cross-section of the studied DT-IPMSM [Finite Element Analysis (ANSYS Maxwell 2D)]

Finite element analysis (FEA) allows to estimate certain parameters of the machine as Table A.1 shows.

In addition, it can be seen at a glance that the machine has 16 poles and 18 slots. This provides several possibilities. In order to have the machine configured as a DT-IPMSM, each phase is built by the combination of three coils so that six phases are obtained. However, if phases were built by two coils, a nine-phase machine would be built, while if six coils formed each phase the obtained machine would be a three-

Table A.1: Estimated DT-IPMSM Parameters (FEA)

Rated current	10.2 A_{RMS}, 14.4A_{peak}
Copper-Losses	175 W
Rated Speed	1125 rpm (150 Hz)
Mechanical Power	7 kW
Rated Torque	59.08 Nm

phase one. Fig. A-7 shows the DT-IPMSM's coil connection that allows to get the six-phase arrangement.

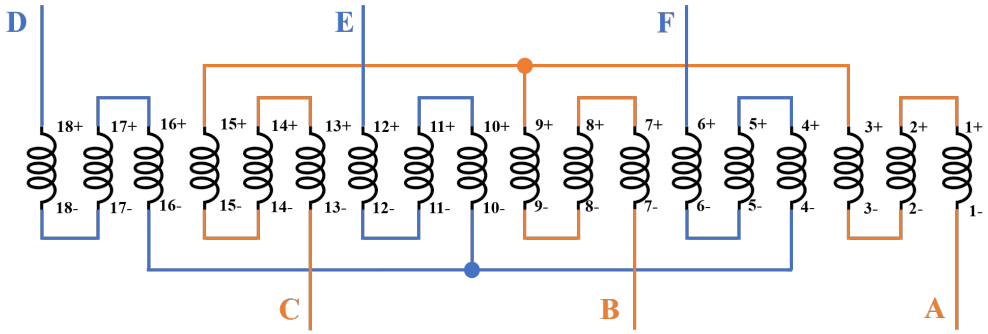

Figure A-7: DT-IPMSM coil's connection

The physical arrangement of the machine windings will follow the structure in Fig. A-8.

Then, in order to get an anti-clockwise rotation direction (from A to D), current must be injected following a direct-sequence, with the phase winding *def* currents lagging 60º the *abc* ones.

A.4 Machine's coupling

Up to this point, experimental tests were done in the DT-IPMSM without load. Hence, the next step will consist of coupling a three-phase machine on the shaft. This machine will set the rotating speed of the assembly while the DT-IPMSM will control the produced torque. Several steps were followed to reach this configuration.

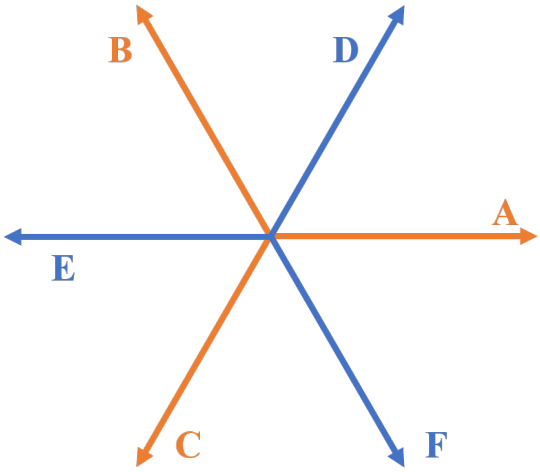

Figure A-8: Physical arrangement of the machine's windings

A.4.1 Incremental Encoder

As said before, until now no encoder was used so that a test phase had to be created in the microcontroller. Now, as speed control is going to be implemented in the three-phase machine, an encoder is needed in order to have information about the machine position in real-time. An encoder allows to transform an angular movement in a series of digital pulses. The generated pulses can be used to control angular displacements. The utilized incremental encoder provides the following signals:

- A square signal A, that provides 1024 pulses per full turn.
- A square signal B, that provides 1024 pulses per full turn, with a 90º phase shift with respect to A.
- A signal Z that allows to know the direction of rotation by providing the absolute 0 position of the encoder axis

By detecting the rising and falling edges of A and B, one full mechanical turn is divided into 4096 pulses. Then, by applying (A.10) it is possible to get the electrical angle in radians.

$$\theta_e = \frac{\text{counts}}{4096} \cdot 2\pi \cdot P \tag{A.10}$$

being, 'counts' the number of pulses that have being counted from the last step through 0, and P the machine's number of pole pairs.

A.4.2 Machine's alignment

To have the rotor of both machine's adequately aligned with the stator is a crucial point in order to obtain a correct performance of both machines. Despite there are two machines, only one encoder will be used as its measurements will be read by both the microcontroller of the DT-IPMSM and the one of the three-phase machine. Hence it is important to have both machines operating in the same situation. The ideal way would be to point out the point at which a magnet of the rotor is completely aligned with the phase A for both machines, and take always this rotor position as the initial one. This will allow to have maximum electromagnetic torque, T_e when $q-$axis current is injected and negligible one when current is injected in the $d-$axis. To mark the rotor position at which phase A is aligned with a magnet can be easily done for each machine independently by injecting voltage in open-loop in phase A. If the injected voltage is high enough, the rotor will turn until the closer magnet is completely aligned to phase A. Once the alignment points of each machine are identified, the machines can be coupled.

However, it is possible that the alignment after the coupling is still not perfect. As the DT-IPMSM has 16 poles, small variations in the mechanical position of the rotor will imply high variations in the electrical one ($\theta_e = \theta_m \cdot P$). Then, in order to assure 0 torque generation when injecting $d-$axis current and maximum torque generation when injecting $q-$axis current, an offset must be included in (A.10). For instance, if the three-phase machine initially has a magnet aligned with its phase A, while the DT-IPMSM has the magnet lagged with respect to its phase A, an offset can be included in (A.10) with the DT-IPMSM microcontroller. Hence, when θ_e of the three-phase machine is already 0, θ_e of the DT-IPMSM must be a bit behind, in a way that when the rotor rotates and the magnet aligns phase A, (A.10) equals 0 for the DT-IPMSM.

A.4.3 Speed Control

After having the machines coupled, aligned and the incremental encoder installed, the new step consists of implementing the desired control strategy in the three-phase machine's inverter. As mentioned before, this machine will be used to fix the speed, so that a closed-loop speed control must be implemented. The control scheme will be similar to the one in Fig. A-5, but now an external speed loop must be implemented in the $q-$axis. The speed feedback will be calculated with the encoder data. The $d-$ axis current reference will be kept on 0. Fig. A-9 shows the schematic for the three-phase machine speed control.

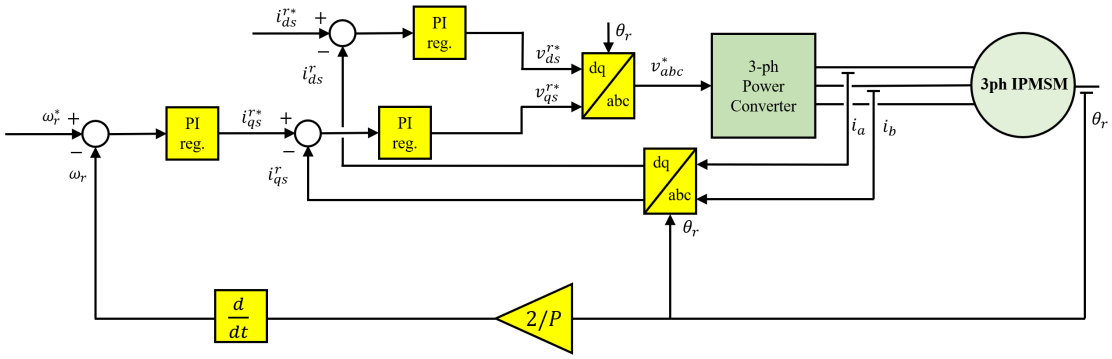

Figure A-9: Schematic of the speed control strategy

A.4.4 RL Estimation

Table A.1 presents some parameters of the DT-IPMSM that were estimated from FEA. However, there is no information about key parameters of the machine as the winding inductances and resistances are. Once the test-bench is fully prepared, it is possible to carry out some methods to analyze these parameters. The idea consists of injecting dq voltage in open-loop with the rotor blocked ($\omega_r^* = 0$), obtain the current response and analyze the transient behavior. It is known that the machine windings

can be studied as a RL circuit. Hence:

$$R_{dq} = \frac{V_{dq}^{ss}}{I_{dq}^{ss}} \tag{A.11}$$

$$L_{dq} = \tau \cdot R_{dq} \tag{A.12}$$

meaning the superscript ^{ss} 'in steady-state'. τ is the circuit time constant. However this method led to inaccurate results, especially when injecting voltage in the $q-$axis as the machine was generating torque and thus some pulsations appeared in the transient responses.

Matlab incorporates a function called $tfest$ that estimates a continuous-time transfer function with specified number of poles, from their input and output. Then, as it is known:

$$G_{I_{dq}V_{dq}} = \frac{I_{dq}}{V_{dq}} = \frac{1}{L_{dq} \cdot s + R_{dq}} \tag{A.13}$$

Hence, once the transfer function is known, it is straightforward to get the inductance and resistance parameters.

Several experimental tests were carried out in order to obtain the R_{dq} and L_{dq} values for different values of injected voltage. Fig. A-10(a) shows the evolution of the estimated resistance for both the $d-$ and the $q-$axis, for each dq system depending on the injected voltage. Fig. A-10(b) shows the evolution of the estimated inductance for both the $d-$ and the $q-$axis, for each dq system depending on the injected voltage. Finally, Fig. A-10(c) shows the almost linear relationship between the injected voltage and the obtained current (both measured). It must be mentioned that, as the machine is blocked while injecting a constant voltage, phase currents during the test are DC ones. DC current flowing through a coil generates a constant magnetic field that does not interact with the rotor magnetic field. Thus, losses in the stator and not in the rotor are only considered.

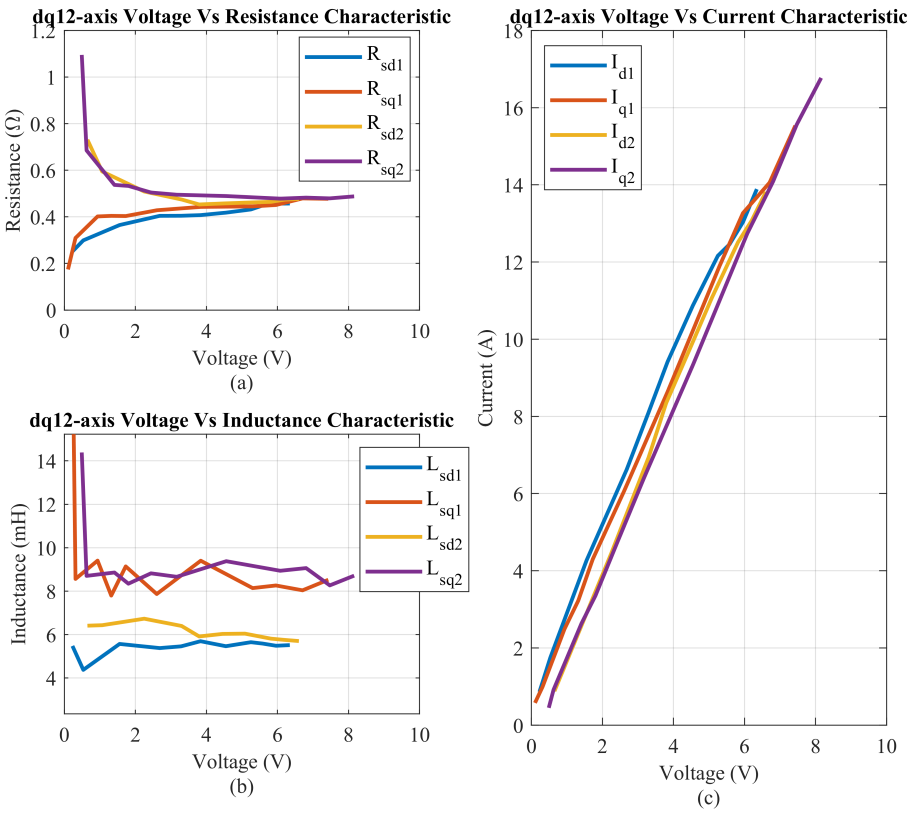

Figure A-10: (a) Stator resistance estimation depending on the injected voltage, (b) Stator inductance estimation depending on the injected voltage, (c) Voltage - Current Characteristic

Once the results are analysed, it could be concluded that:

$$R_{s_{d_1}} \approx R_{s_{d_2}} \approx R_{sq_1} \approx R_{s_{q_2}} = 0.47\ \Omega$$

$$L_{s_{d_1}} \approx L_{s_{d_2}} = 5.7\ mH$$

$$L_{s_{q_1}} \approx L_{s_{q_2}} = 8.5\ mH$$

However, as seen in equation (4.27) rotor temperature can be estimated with prior knowledge of the rotor resistance as well as the stator one. Hence, the resistance of the PMs must be also calculated. In order to achieve an interaction between the stator magnetic field and the rotor one promoted by the PMs, a rotatory magnetic field must be created by the stator. The test will be quite similar to the previous one. However, now instead of injecting constant synchronous voltages that, as the machine

is stopped promote DC phase currents, a pulsating high-frequency (HF) synchronous voltage will be injected in the machine's windings. This will lead to ac phase currents that generate a rotatory magnetic field that interacts with the magnetic field created by the magnets. The test is only done in one of both $dq-$sets, injecting only voltage in the $d-$axis, as the $d-$axis resistance is the one of interest. In addition, both $d-$ and $q-$axis resistances should seem similar as seen in Fig. A-10 for the stator case. About the inductance, its value should remain constant as the test is done at 500 Hz. High-frequencies tend to reduce the inductance value in this type of machines but in the range of kHz's. The obtained data will be treated using the *Fast Fourier Transform*, FFT in order to clearly distinguish the frequency components, as seen in Fig. A-11.

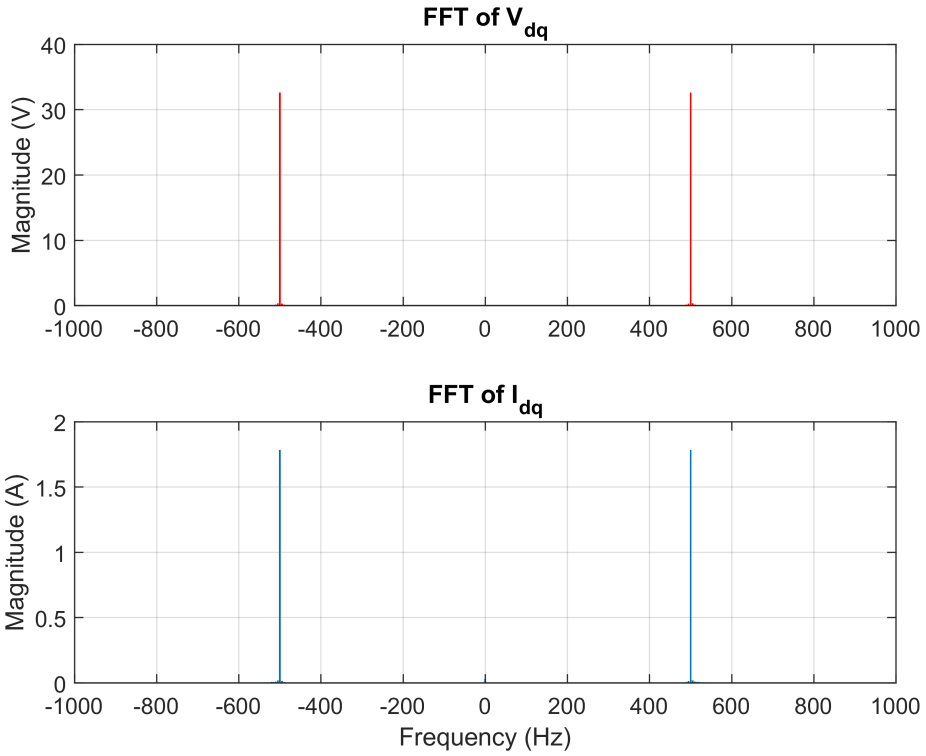

Figure A-11: $d-$axis voltage and current FFT's when injecting a pulsating high-frequency voltage (500 Hz)

It can be seen how the positive and the negative sequence components of current at the injected voltage frequency are clearly distinguished. Then, dividing the complex

component of voltage over the current one, the impedance of the combination of both rotor and stator is obtained. The real part is related with the resistance, while the reactance consists of the imaginary part. Dividing the reactance over the high-frequency, the inductance is obtained. The test was repeated for different amplitudes of the injected voltage, obtaining the following results:

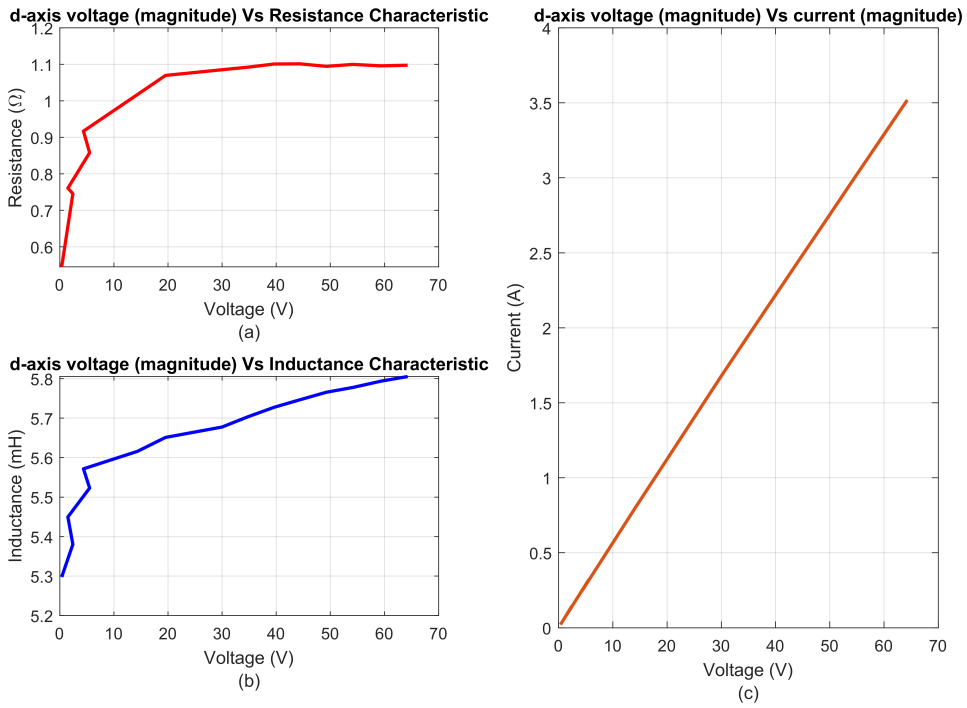

Figure A-12: (a) Rotor resistance estimation depending on the injected voltage, (b) Rotor inductance estimation depending on the injected voltage, (c) Voltage - Current Characteristic

As mentioned before, it can be seen how the inductance values are between 5.6 mH and 5.8 mH which matches with the ones obtained when injecting constant DC voltages. About the resistance, it stabilizes in a value around 1.1 Ω. Hence, the rotor

resistance in the $d-$axis can be computed as follows:

$$
\begin{aligned}
&R_{tot_d} \approx 1.1\ \Omega \\
&R_{s_d} \approx 0.47\ \Omega \\
&R_{r_d} = R_{tot_d} - R_{s_d} \approx 0.63\ \Omega
\end{aligned}
\tag{A.14}
$$

A.4.5 Additional hardware for emulating an open-phase fault

As stated before, one of the goals of this Master Thesis is to implement a fault-tolerant control strategy. Hence, emulating an open-circuit fault in one of the DT-IPMSM phases must be done in a safe way. In order to do so, the following elements will be used:

- Contactor
- Programmable relay
- DSP GPIO output

Phase A will be connected from the inverter to the DT-IPMSM through the contactor, whose coil will be connected to the single-phase grid through the relay. When the contactor's coil is fed, it will be closed so that phase A will be connected to the electric machine. On the other hand, if the coil is not fed, the contactor will be open, and the machine will suffer an open-phase fault. Hence, the connection of phase A will depend on the state of the programmable relay. This relay allows to open and close a contact depending on the value of a digital input signal. This input signal will come from a DSP GPIO output whose value can be managed from the computer. Then, if the GPIO signal is set to 0, the relay will keep the contact open and as the contactor's coil will not be fed, there will be an open-phase fault. Otherwise, when the DSP GPIO signal is turned to 1, the programmable relay will close its contact, so that the contactor's coil will be fed. Hence, the contactor will be closed and phase A will be connected to the machine.

Bibliography

[1] International Energy Agency. "IEA Technology Collaboration Programme on Energy Efficient End-Use Equipment (4E). Annual Report 2017". Available at https://www.iea-4e.org/document/416/4e-2017-annual-report, accessed 16-April-2020.

[2] International Energy Agency. "Global EV Outlook 2019". Available at https://www.iea.org/reports/global-ev-outlook-2019, accessed 16-April-2020.

[3] M. J. Duran and F. Barrero. "Recent Advances in the Design, Modeling, and Control of Multiphase Machines—Part I". *IEEE Trans. Ind. Electr. Journal*, 63(1):449–458, January 2016.

[4] M. J. Duran and F. Barrero. "Recent Advances in the Design, Modeling, and Control of Multiphase Machines—Part II". *IEEE Trans. Ind. Appl., Journal*, 63(1):459–468, January 2016.

[5] M. Ruba and D. Fodorean. "Analysis of Fault-Tolerant Multiphase Power Converter for a Nine-Phase Permanent Magnet Synchronous Machine". *IEEE Trans. Ind. Appl. Journal*, 48(6):2092–2101, November 2012.

[6] F. Aghili. "Energy-Efficient and Fault Tolerant Control of Multiphase Nonsinusoidal PM Synchronous Machines". *IEEE Trans. Ind. Mechatronics, Journal*, 20(6):2736–2751, December 2015.

[7] X. Kestelyn and E. Semail. "A Vectorial Approach for Generation of Optimal Current References for Multiphase Permanent-Magnet Synchronous Machines in Real Time". *IEEE Trans. Ind. Electr. Journal*, 58(11):5057–5065, November 2011.

[8] N.Nguyen, F. Meinguet, E. Semail, and Xavier Kestelyn. "Fault-Tolerant Operation of an Open-End Winding Five-Phase PMSM Drive With Short-Circuit Inverter Fault". *IEEE Trans. Ind. Electr. Journal*, 63(1):595–604, January 2016.

[9] J. M. Guerrero and O. Ojo. "Flux Level Selection in Vector-Controlled Dual Stator Winding Induction Machines". *Electric Power Applications, IET Journal*, 3(6):562–572, 2009.

[10] J. M. Guerrero and O. Ojo. "Total Airgap Flux Minimization in Dual Stator Winding Induction Machines". *Power Electronics, IEEE Transactions Journal*, 24(3):787–795, 2009.

[11] L. Parsa and H. A. Toliyat. Fault-tolerant five-phase permanent magnet motor drives. In *Conference Record of the 2004 IEEE Industry Applications Conference, 2004. 39th IAS Annual Meeting.*, volume 2, pages 1048–1054 vol.2, 2004.

[12] A. Ashoush, S. M. Gadoue, A. S. Abdel-Khalik, and A. L. Mohamadein. Current optimization for an eleven-phase induction machine under fault conditions using genetic algorithm. In *8th IEEE Symposium on Diagnostics for Electrical Machines, Power Electronics Drives*, pages 529–534, 2011.

[13] Nounou Kamal, Mohamed Benbouzid, Khoudir Marouani, Jean Charpentier, and Abdelaziz Kheloui. Performance comparison of open-circuit fault- tolerant control strategies for multiphase permanent magnet machines for naval applications. *Electrical Engineering*, 100:1827–1836, 09 2018.

[14] S. Dwari and L. Parsa. An optimal control technique for multiphase pm machines under open-circuit faults. *IEEE Transactions on Industrial Electronics*, 55(5):1988–1995, 2008.

[15] H. S. Che, M. J. Duran, E. Levi, M. Jones, W. Hew, and N. A. Rahim. Postfault operation of an asymmetrical six-phase induction machine with single and two isolated neutral points. *IEEE Transactions on Power Electronics*, 29(10):5406–5416, 2014.

[16] X. Wang, Z. Wang, Z. Xu, and M. Cheng. Fault diagnosis and tolerance of dual three-phase pmsm drives. In *2018 IEEE Energy Conversion Congress and Exposition (ECCE)*, pages 325–330, 2018.

[17] Y. Feng, Y. Liao, H. Lin, and L. Yan. Fault-tolerant control of six-phase permanent-magnet synchronous machine drives under open-phase faults. In *2019 22nd International Conference on Electrical Machines and Systems (ICEMS)*, pages 1–5, 2019.

[18] L. Alberti and N. Bianchi. Experimental tests of dual three-phase induction motor under faulty operating condition. *IEEE Transactions on Industrial Electronics*, 59(5):2041–2048, 2012.

[19] M. A. Parker, C. Ng, and L. Ran. Fault-tolerant control for a modular generator–converter scheme for direct-drive wind turbines. *IEEE Transactions on Industrial Electronics*, 58(1):305–315, 2011.

[20] J. O. Estima and A. J. M. Cardoso. A fault-tolerant permanent magnet synchronous motor drive with integrated voltage source inverter open-circuit faults diagnosis. In *Proceedings of the 2011 14th European Conference on Power Electronics and Applications*, pages 1–10, 2011.

[21] W. Wang, J. Zhang, M. Cheng, and S. Li. Fault-tolerant control of dual three-phase permanent-magnet synchronous machine drives under open-phase faults. *IEEE Transactions on Power Electronics*, 32(3):2052–2063, 2017.

[22] X. Wang, Z. Wang, Z. Xu, M. Cheng, W. Wang, and Y. Hu. Comprehensive diagnosis and tolerance strategies for electrical faults and sensor faults in dual three-phase pmsm drives. *IEEE Transactions on Power Electronics*, 34(7):6669–

6684, 2019.

[23] Z. Changpan, T. Wei, S. Xiang dong, Z. Zhaoji, Y. Guijie, and S. Jianyong. Control strategy for dual three-phase pmsm based on reduced order mathematical model under fault condition due to open phases. *The Journal of Engineering*, 2018(13):489–494, 2018.

[24] W. Zhang, Y. Xu, and B. Chen. Control of dual three-phase permanent magnet synchronous motor under open phase fault conditions. In *2016 IEEE Vehicle Power and Propulsion Conference (VPPC)*, pages 1–5, 2016.

[25] M. Shamsi-Nejad, B. Nahid-Mobarakeh, S. Pierfederici, and F. Meibody-Tabar. Fault tolerant and minimum loss control of double-star synchronous machines under open phase conditions. *IEEE Transactions on Industrial Electronics*, 55(5):1956–1965, 2008.

[26] H. Lu, J. Li, R. Qu, D. Ye, and Y. Lu. Fault-tolerant predictive control of six-phase pmsm drives based on pulsewidth modulation. *IEEE Transactions on Industrial Electronics*, 66(7):4992–5003, 2019.

[27] M. Ganchev, C. Kral, and T. Wolbank. Compensation of speed dependency in sensorless rotor temperature estimation for permanent magnet synchronous motor. In *2012 XXth International Conference on Electrical Machines*, pages 1612–1618, 2012.

[28] M. Ganchev, C. Kral, H. Oberguggenberger, and T. Wolbank. Sensorless rotor temperature estimation of permanent magnet synchronous motor. In *IECON 2011 - 37th Annual Conference of the IEEE Industrial Electronics Society*, pages 2018–2023, 2011.

[29] A. J. Grobler, S. R. Holm, and G. van Schoor. Thermal modelling of a high speed permanent magnet synchronous machine. In *2013 International Electric Machines Drives Conference*, pages 319–324, 2013.

[30] T. Huber, W. Peters, and J. Böcker. A low-order thermal model for monitoring critical temperatures in permanent magnet synchronous motors. In *7th IET International Conference on Power Electronics, Machines and Drives (PEMD 2014)*, pages 1–6, 2014.

[31] D. D. Reigosa, F. Briz, P. García, J. M. Guerrero, and M. W. Degner. Magnet temperature estimation in surface pm machines using high-frequency signal injection. *IEEE Transactions on Industry Applications*, 46(4):1468–1475, 2010.

[32] D. Reigosa, F. Briz, M. W. Degner, P. García, and J. M. Guerrero. Temperature issues in saliency-tracking based sensorless methods for pm synchronous machines. In *2010 IEEE Energy Conversion Congress and Exposition*, pages 3123–3130, 2010.

[33] D. D. Reigosa, F. Briz, M. W. Degner, P. Garcia, and J. M. Guerrero. Magnet temperature estimation in surface pm machines during six-step operation. *IEEE Transactions on Industry Applications*, 48(6):2353–2361, 2012.

[34] D. D. Reigosa, D. Fernandez, H. Yoshida, T. Kato, and F. Briz. Permanent-magnet temperature estimation in pmsms using pulsating high-frequency current injection. *IEEE Transactions on Industry Applications*, 51(4):3159–3168, 2015.

[35] D. D. Reigosa, D. Fernandez, T. Tanimoto, T. Kato, and F. Briz. Permanent-magnet temperature distribution estimation in permanent-magnet synchronous machines using back electromotive force harmonics. *IEEE Transactions on Industry Applications*, 52(4):3093–3103, 2016.

[36] E. Levi. Multiphase electric machines for variable-speed applications. *IEEE Transactions on Industrial Electronics*, 55(5):1893–1909, 2008.

[37] Y. Miyama and K. Akatsu. Technical arrangement of high-performance techniques achieved by multi-phase permanent magnet synchronous motor systems. In *2018 IEEE Energy Conversion Congress and Exposition (ECCE)*, pages 1574–1580, 2018.

[38] H. Zhang, B. Zhao, J. Gong, Y. Xu, D. T. Vu, N. Ky Nguyen, E. Semail, and T. J. dos Santos Moraes. Torque optimization of a seven-phase bi-harmonic pmsm in healthy and degraded mode. In *2019 22nd International Conference on Electrical Machines and Systems (ICEMS)*, pages 1–6, 2019.

[39] X. Ma, Y. Yu, H. Zhang, W. Wang, and L. Liu. Study on direct torque control of dual y shift 30 degree six-phase pmsm. In *2015 IEEE 10th Conference on Industrial Electronics and Applications (ICIEA)*, pages 1964–1968, 2015.

[40] M. Kozovsky, P. Blaha, and P. Vaclavek. Verification of nine-phase pmsm model in d-q coordinates with mutual couplings. In *2016 6th IEEE International Conference on Control System, Computing and Engineering (ICCSCE)*, pages 73–78, 2016.

[41] M. Barcaro, N. Bianchi, and F. Magnussen. Analysis and tests of a dual three-phase 12-slot 10-pole permanent-magnet motor. *IEEE Transactions on Industry Applications*, 46(6):2355–2362, 2010.

[42] S. Maekawa, M. Sugimoto, A. Yokoyama, and K. Yasui. Proposal of electrolytic capacitor-less and reactor-less drive system using triple three phase pmsm. In *2019 21st European Conference on Power Electronics and Applications (EPE '19 ECCE Europe)*, pages P.1–P.6, 2019.

[43] J. F. Gieras. *Permanent Magnet Motor Technology: Design and Applications, Third Edition.* Boca Raton, 3 edition, September 2009.

[44] Yifan Zhao and T. A. Lipo. Space vector pwm control of dual three-phase induction machine using vector space decomposition. *IEEE Transactions on Industry Applications*, 31(5):1100–1109, 1995.

[45] T. Sebastian. Temperature effects on torque production and efficiency of pm motors using ndfeb magnets. *IEEE Transactions on Industry Applications*, 31(2):353–357, 1995.

[46] G. Feng, C. Lai, K. L. V. Iyer, and N. C. Kar. Torque ripple modeling and min-

imization for pmsm drives with consideration of magnet temperature variation. In *2016 XXII International Conference on Electrical Machines (ICEM)*, pages 612–618, 2016.

[47] H. Liu, H. Lin, Z. Q. Zhu, M. Huang, and P. Jin. Permanent magnet remagnetizing physics of a variable flux memory motor. *IEEE Transactions on Magnetics*, 46(6):1679–1682, 2010.

[48] K. Sakai, K. Yuki, Y. Hashiba, N. Takahashi, and K. Yasui. Principle of the variable-magnetic-force memory motor. In *2009 International Conference on Electrical Machines and Systems*, pages 1–6, 2009.

[49] B. Gagas, T. Fukushige, T. Kato, and R. D. Lorenz. Operating within dynamic voltage limits during magnetization state increases in variable flux pm synchronous machines. In *2014 IEEE Energy Conversion Congress and Exposition (ECCE)*, pages 5206–5213, 2014.

[50] C. Yu, T. Fukushige, A. Athavale, B. Gagas, K. Akatsu, D. Reigosa, and R. D. Lorenz. Zero/low speed magnet magnetization state estimation using high frequency injection for a fractional slot variable flux-intensifying interior permanent magnet synchronous machine. In *2014 IEEE Energy Conversion Congress and Exposition (ECCE)*, pages 2495–2502, 2014.

[51] A. Toba, A. Daikoku, N. Nishiyama, Y. Yoshikawa, and Y. Kawazoe. Recent technical trends in variable flux motors. In *2014 International Power Electronics Conference (IPEC-Hiroshima 2014 - ECCE ASIA)*, pages 2011–2018, 2014.

[52] Hengchuan Liu, Heyun Lin, Shuhua Fang, and Xueliang Huang. Investigation of influence of permanent magnet shape on field-control parameters of variable flux memory motor with fem. In *2008 World Automation Congress*, pages 1–4, 2008.

[53] R. Owen, Z. Q. Zhu, J. B. Wang, D. A. Stone, and I. Urquhart. Review of variable-flux permanent magnet machines. In *2011 International Conference on Electrical Machines and Systems*, pages 1–6, 2011.

[54] Arnold Magnetics. *Catalogs and literature.* Available at `https://www.arnoldmagnetics.com/resources/catalogs-literature/`, accessed 28-April-2020.

[55] B. M. Ma, Y. L. Liang, J. Patel, D. Scott, and C. O. Bounds. The effect of fe on the temperature dependent magnetic properties of sm(co,fe,cu,zr)/sub z/ and smco/sub 5/ sintered magnets at 450/spl deg/c. *IEEE Transactions on Magnetics*, 32(5):4377–4379, 1996.

[56] Arnold Magnetics. *The important role of dysprosium in modern permanent magnets.* Available at `https://www.arnoldmagnetics.com/resources/technical-publications/`, accessed 28-April-2020.

[57] J. D. McFarland, T. M. Jahns, A. M. EL-Refaie, and P. B. Reddy. Effect of magnet properties on power density and flux-weakening performance of high-speed interior permanent magnet synchronous machines. In *2014 IEEE Energy Conversion Congress and Exposition (ECCE)*, pages 4218–4225, 2014.

[58] S. Ruoho, J. Kolehmainen, J. Ikaheimo, and A. Arkkio. Interdependence of demagnetization, loading, and temperature rise in a permanent-magnet synchronous motor. *IEEE Transactions on Magnetics*, 46(3):949–953, 2010.

[59] K. . Kim, S. . Lim, D. . Koo, and J. Lee. The shape design of permanent magnet for permanent magnet synchronous motor considering partial demagnetization. *IEEE Transactions on Magnetics*, 42(10):3485–3487, 2006.

[60] D. Torregrossa, A. Khoobroo, and B. Fahimi. Prediction of acoustic noise and torque pulsation in pm synchronous machines with static eccentricity and partial demagnetization using field reconstruction method. *IEEE Transactions on Industrial Electronics*, 59(2):934–944, 2012.

[61] S. Moon, J. Lee, H. Jeong, and S. W. Kim. Demagnetization fault diagnosis of a pmsm based on structure analysis of motor inductance. *IEEE Transactions on Industrial Electronics*, 63(6):3795–3803, 2016.

[62] X. Xiao and C. Chen. Reduction of torque ripple due to demagnetization in pmsm using current compensation. *IEEE Transactions on Applied Superconductivity*, 20(3):1068–1071, 2010.

[63] G. Choi and T. M. Jahns. Post-demagnetization characteristics of permanent magnet synchronous machines. In *2015 IEEE Energy Conversion Congress and Exposition (ECCE)*, pages 1781–1788, 2015.

[64] P. Milanfar and J. H. Lang. Monitoring the thermal condition of permanent-magnet synchronous motors. *IEEE Transactions on Aerospace and Electronic Systems*, 32(4):1421–1429, 1996.

[65] M. Ganchev, B. Kubicek, and H. Kappeler. Rotor temperature monitoring system. In *The XIX International Conference on Electrical Machines - ICEM 2010*, pages 1–5, 2010.

[66] M. Ganchev, H. Umschaden, and H. Kappeler. Rotor temperature distribution measuring system. In *IECON 2011 - 37th Annual Conference of the IEEE Industrial Electronics Society*, pages 2006–2011, 2011.

[67] C. Kral, A. Haumer, and S. B. Lee. Innovative thermal model for the estimation of permanent magnet and stator winding temperatures. In *2012 IEEE Energy Conversion Congress and Exposition (ECCE)*, pages 2704–2711, 2012.

[68] A. M. EL-Refaie, N. C. Harris, T. M. Jahns, and K. M. Rahman. Thermal analysis of multibarrier interior pm synchronous machine using lumped parameter model. *IEEE Transactions on Energy Conversion*, 19(2):303–309, 2004.

[69] C. Kral, A. Haumer, and S. B. Lee. A practical thermal model for the estimation of permanent magnet and stator winding temperatures. *IEEE Transactions on Power Electronics*, 29(1):455–464, 2014.

[70] B. Lee, K. Kim, J. Jung, J. Hong, and Y. Kim. Temperature estimation of ipmsm using thermal equivalent circuit. *IEEE Transactions on Magnetics*, 48(11):2949–2952, 2012.

[71] K. Liu and Z. Q. Zhu. Online estimation of the rotor flux linkage and voltage-source inverter nonlinearity in permanent magnet synchronous machine drives. *IEEE Transactions on Power Electronics*, 29(1):418–427, 2014.

[72] K. Liu and Z. Q. Zhu. Mechanical parameter estimation of permanent-magnet synchronous machines with aiding from estimation of rotor pm flux linkage. *IEEE Transactions on Industry Applications*, 51(4):3115–3125, 2015.

[73] S. J. Underwood and I. Husain. Online parameter estimation and adaptive control of permanent-magnet synchronous machines. *IEEE Transactions on Industrial Electronics*, 57(7):2435–2443, 2010.

[74] S. Ichikawa, M. Tomita, S. Doki, and S. Okuma. Sensorless control of permanent-magnet synchronous motors using online parameter identification based on system identification theory. *IEEE Transactions on Industrial Electronics*, 53(2):363–372, 2006.

[75] T. Huber, W. Peters, and J. Böcker. Monitoring critical temperatures in permanent magnet synchronous motors using low-order thermal models. In *2014 International Power Electronics Conference (IPEC-Hiroshima 2014 - ECCE ASIA)*, pages 1508–1515, 2014.

[76] J. Faiz and H. Nejadi-Koti. Demagnetization fault indexes in permanent magnet synchronous motors—an overview. *IEEE Transactions on Magnetics*, 52(4):1–11, 2016.

[77] Daniel Fernandez Alonso. *Control And Supervision of Permanent Magnet Synchronous Machines using High Frequency Signal Injection*. PhD thesis, Universidad de Oviedo, February 2017.

[78] Shengnan Wang, Yun-Ze Li, Yang Liu, Hang Zhou, Yunhua Li, Wei Guo, and Xi Xiao. Temperature control of permanent-magnet synchronous motor using phase change material. 07 2015.

[79] B. Hannon, P. Sergeant, and L. Dupré. Evaluation of the rotor eddy-currents in high-speed pmsms with a shielding cylinder. In *2018 XIII International Conference on Electrical Machines (ICEM)*, pages 1182–1187, 2018.

[80] S. Zhu, M. Cheng, and Y. Zhu. Fast calculation of pm eddy current loss in ipmsm under pwm vsi supply based on the spectra of line-line voltage. *IEEE Transactions on Magnetics*, 54(11):1–5, 2018.

[81] Hispavila. *Filtros activos*, 2005.

[82] Marek Štulrajter, Valéria Hrabovcová, and Marek Franko. Permanent magnets synchronous motor control theory. *Journal of Electrical Engineering*, 58:79–84, 03 2007.

[83] Nitiksha Pancholi Chand Thakor Unnati Mali Yashvi Parmar, Priyanka Patel. Scalar control of permanent magnet synchronous motor. *International Research Journal of Engineering and Technology (IRJET)*, 3, 12 2016.